Remodelled Ribosomes Synthesise a Specific Proteome in Proliferating Plant Tissue during Cold

Federico Martinez-Seidel[1*,2¶], Pipob Suwanchaikasem[2], Dione Gentry-Torfer[1,2], Yogeswari Rajarathinam[1], Alina Ebert[1, 2], Alexander Erban[1], Alexandre Augusto Pereira Firmino[1], Shuai Nie[3], Michael G. Leeming[3,4], Nicholas A. Williamson[3,5], Ute Roessner[2], Joachim Kopka[1], Berin A. Boughton[2,6]

***For correspondence:** mseidel@mpimp-golm.mpg.de (FM-S)

Present address: ¶Willmitzer Department, Max-Planck-Institute of Molecular Plant Physiology, Potsdam-Golm, Germany

[1]Molecular Physiology Department, Max-Planck-Institute of Molecular Plant Physiology, Potsdam-Golm, Germany; [2]School of BioSciences, The University of Melbourne, Parkville, VIC, Australia; [3]Bio21 Institute of Molecular Science and Biotechnology, The University of Melbourne, Parkville, VIC, Australia; [4]School of Chemistry, The University of Melbourne, Parkville, VIC, Australia; [5]Department of Biochemistry and Molecular Biology, The University of Melbourne, Parkville, VIC, Australia; [6]Australian National Phenome Centre, Murdoch University, Murdoch, WA, Australia

Abstract

Plant acclimation to low temperatures occurs through system-wide mechanisms that include proteome shifts, some of which occur at the level of protein synthesis. All proteins are synthesised by ribosomes. Rather than being monolithic, transcript-to-protein translation machines, ribosomes can be selective and cause effective proteome shifts required for successful temperature acclimation. Here, we use apical root meristems of germinating seedlings of the monocotyledonous plant barley as a model to study changes in protein abundance and synthesis rates during cold acclimation. We measure metabolic and physiological parameters that allow us to compare protein synthesis rates in different physiological states, e.g., in cold acclimation compared to the optimal temperature state. We show that ribosomal proteins are independently synthesised and assembled into ribosomal complexes in root proliferative tissue, and assess how the ribo-proteome shifts during cold may be associated with changes in synthesis and accumulation of macromolecular complexes. We demonstrate that translation initiation is the limiting step during cold acclimation and based on our data propose a model of a ribosomal code that depends on a reconfigured ribosome population, where as a mode of cold acclimation, specific ribosomal protein compositions may confer selective association capabilities between 60S subunits and 48S initiation complexes.

Introduction

Cold acclimation is a physiological challenge for sessile plant organisms (***Hincha and Zuther, 2020***; ***Middleton et al., 2014***; ***Thomashow, 1999***). Next to extensively studied transcriptional responses (***Seki et al., 2002***; ***Jaglo-Ottosen et al., 1998***; ***Thomashow, 1999***; ***Fowler and Thomashow, 2002***; ***Hincha et al., 2012***), cold-triggered translational reprogramming moves into the focus as a hub for temperature acclimation (***Garcia-Molina et al., 2020***; ***Beine Golovchuk et al., 2018***; ***Schmidt et al., 2013***). Translation provides a second regulatory layer that integrates signals from cellular

processes and generates a cold acclimated proteome based on the primary layer of a remodeled transcriptome (***Yu et al., 2020***; ***Martinez-Seidel et al., 2021a***,c; ***Cheong et al., 2021***).

The functional importance of translation is evident in germinating barley seedlings when they stop growing during the first days of acclimation to a cold shift (***Martinez-Seidel et al., 2021c***) and yet continue to accumulate translation-related complexes in the root tip well above the level of plants grown at optimized temperature (***Martinez-Seidel et al., 2021c***). In the absence of growth, synthesis of new ribosomes appears activated or alternatively, the existing ones are less degraded. Regardless of the mechanism, the accumulation of translation-related complexes correlates with evidence of a cold-induced total proteome shift in root proliferative tissue. This shift comprises not only evidence of the accumulation of structural ribosomal proteins (rProteins) but also of elements of ribosome assembly and translation initiation (***Martinez-Seidel et al., 2021c***).

In Arabidopsis, the ribosome population that accumulates after a cold-shift in roots has altered ribosomal protein (rProtein) composition compared to temperature-optimised control conditions (***Cheong et al., 2021***; ***Martinez-Seidel et al., 2021a***), suggesting that temperature-shifts trigger ribosome heterogeneity. Ribosome heterogeneity can contribute to proteome shifts by selective translation of the transcriptome. Targeted translation of mRNAs based on altered ribosomal structures is referred to as ribosome specialization (***Genuth and Barna, 2018***; ***Martinez-Seidel et al., 2020***; ***Slavov et al., 2015***). Functional specialization of ribosomes entails translational events that drive a response to an external (***Lambers, 2022***; ***Berková et al., 2020***; ***Moin et al., 2021***; ***Appels et al., 2021***) or a developmental (***Norris et al., 2021***; ***Shrestha et al., 2022***; ***Xiong et al., 2021***) cue, for example, the preferred translation of specific groups of proteins that facilitate acclimation to low temperatures. These concepts suggest that the previously observed abundance changes of the translational machinery in cold-acclimating root tips of barley seedlings (***Martinez-Seidel et al., 2021c***) may indicate the production of ribosomes tuned to cold-specialized translation. Protein biosynthesis, including ribosome biogenesis, is the largest energy expenditure in the cell (***Ingolia et al., 2019***; ***Russell and Cook, 1995***; ***Verduyn et al., 1991***) and consequently building a specialized ribosome population *de novo* would consume much time and resources. In plants, cytosolic ribosomes have an rProtein-based half-life of 3-4 days (***Salih et al., 2020***), and thus ribosome biogenesis alone may fail to satisfy the demand for customized ribosomal complexes during cold. Thus, there may be a ribosome remodeling mechanism that relies on increased biogenesis and/or *in-situ* ribosome remodelling to alter steady proteome dynamics by causing a cold-induced proteome shift.

The cellular proteome is highly dynamic in sessile plants. The transition between different proteome states is a constant feature in the plant life cycle and varies between organs and tissues (***Nelson and Millar, 2015***). Plant roots contain cells at multiple different developmental and ontological stages that coexist along longitudinal and radial axes (***Dinneny and Benfey, 2008***). The proteome of the root tip is highly dynamic and demonstrably differed from the longitudinal adjacent older tissue, specifically considering the cold triggered abundance changes of translation- and ribosome-associated proteins (***Martinez-Seidel et al., 2021c***). Root apical meristems are "hotspots" of growth and require a high amount of newly synthesised ribosomes to support cell proliferation compared to the adjacent elongation and differentiation zones (***Clowes, 1958***; ***Verbelen et al., 2006***). The relatively large size of barley roots makes them an ideal system to compare proteome dynamics in response to environmental cues. Barley roots allow for feasible sampling of a sufficiently large tip enriched for meristematic cells. Such sampling circumvents one of the major limitations in analysing complex root landscapes as it avoids pooling of highly diverse root zones and the masking of phenomena linked to rapidly proliferating cells by the more abundant static root zones.

The proteome dynamics are related to protein turnover, which is the balance between protein synthesis and degradation. These two processes lead in different contexts to shifts in the relative abundances of active protein pools. Translation is related mainly to protein biosynthesis and approaches to study translational dynamics typically involve the use of stable isotope mass spectrometry as an empirical measure of protein synthesis (K_s) and degradation (K_d) (***Nelson et al., 2014b***,a). The calculation of plant protein K_s using a stable isotope pulse depends on several parameters that must be considered (***Ishihara et al., 2015***, ***2021***; ***Li et al., 2017***). The amount of protein fraction that has taken up the externally supplied stable isotope tracer can be determined by isotopolog analysis of proteinogenic amino acids from isolated and hydrolyzed protein fractions or individual purified proteins. Alternatively, proteomics technology allows multiparallel isotopolog distribution analysis of peptides obtained by digestion of complex protein preparations. The time of stable isotope pulse to sample collection allows conversion of observed isotope enrichment and protein concentration values into rates. To prevent physiological differences in plant tissue and environmental factors from confounding these calculations, several variables are required to correct and normalize protein K_s rates. The first two variables are protein content and relative growth rate (RGR), which are required to adjust K_s rates between plant systems that differ in these characteristics. A third set of variables describes the dynamics of tracer incorporation into soluble amino acid pools, and label incorporation into these pools may differ between the physiological conditions being compared and between individual proteinogenic amino acids (***Ishihara et al., 2021***). All of these variables are necessary to correct the isotopic envelopes of proteins or digested peptides based on knowledge of their individual amino acid sequences. These corrections are particularly important when the compared plant systems are transitioning between physiological quasi-stable states, as is the case in most studies of development, physiology, and environment x genome interactions, and especially during the well-described sequences of cold acclimation. The non-acclimated and acclimated states of plants drastically alter protein accumulation (***Martinez-Seidel et al., 2021c***), growth dynamics (***Beine Golovchuk et al., 2018***; ***Martinez-Seidel et al., 2021a***,c), and pools of soluble amino acids (***Kaplan et al., 2004***; ***Guy et al., 2008***). Such changes could strongly bias the observed protein K_s rates without correction.

In this study, we explore the proteome dynamics in barley root tips by stable isotope tracing and proteomic mass spectrometry of a protein fraction enriched for assembled translation-related complexes. We aim to provide new insight into non-steady-state translation dynamics of this rapidly developing plant tissue. We calculate K_s rates of individual peptides from samples of barley seedlings germinated in the dark prior to emergence of photosynthetic activity and compare acclimation to sub-optimal temperature (4°C) with optimal temperature (20°C). Our experiments correct for differential growth and protein accumulation and validate the calculation of K_s rates by morphometric and metabolic phenotype analyses. We monitor protein abundances, RGR, and label incorporation into soluble amino acid pools and thereby correct for expected differential isotope tracer dilution of the peptide building blocks. Using the corrected K_s rates, we investigate whether the ribosome population that accumulates during cold acclimation consists of *de novo* synthesised rProteins or alternatively, whether rProteins remain non-labelled and are re-used. We report changes of rProteins in cold-acclimated ribosomal populations and compare these findings to various other co-purified cellular protein complexes that are preferentially synthesised during cold and are either functionally related to the protein biosynthesis machinery or have different cellular functions.

Results

Experimental design

To ensure legitimate, physiological rearing conditions for barley seedlings, we followed previously published procedures (***Martinez-Seidel et al., 2021c***) with few modifications (Figure 1). Seeds were

imbibed for 14 hours under sterile conditions, then transferred to liquid medium and germinated on plates for another 48 hours. At this time, we applied different temperature regimes to mimic an agronomically relevant temperature drop after sowing barley in the field. Germination occurred in the dark for an additional 60 hours, which corresponds to an optimal seeding depth equivalent to the typical period of about 5 days before barley seedlings emerge from the soil in the field (***Kirby, 1993***).

Figure 1

Control seedlings continued to germinate at an optimal temperature of 25°C/ 18°C in a 16-hour day/8-hour night regime (Figure 1 - Figure S1) with an average temperature of 22°C over 24 hours. Barley seedlings treated with low temperatures were cultured at a suboptimal, but not lethal, temperature of a constant 4°C. Differential growth, one of the necessary variables for calculating individual protein synthesis rates, was monitored by high-resolution imaging of independently germinated seedlings at 12-hour intervals (Figure S1). Throughout the approximately 5-day period, etiolation, premature greening, seed nutrient starvation, and other processes resulting from unnaturally long darkness were avoided (***Kirby, 1993***). Seedlings at 4°C developed more slowly but showed no other macroscopic phenotypic changes (Figure S1). We began labeling seedlings with ^{15}N coincident with the temperature shift 48 hours after germination (t_0) and throughout the differential temperature treatment to ensure that the dynamics of tracer incorporation reflected the physiological change associated with cold acclimation and delayed growth. After 108 hours of germination, i.e. at the last experimental time point (t_f) of the labeling experiments, the root tips of the seedlings were harvested to analyze the isotope incorporation and pool sizes of soluble amino acids and to measure the relative abundances and ^{15}N enrichment of individual proteins (Figure 1 - Figure S2).

Root growth dynamics

Root systems of germinating barley seedlings were carefully phenotyped using non-destructive and paired destructive measurements to characterize differential growth and biomass dynamics induced by different temperature regimes. We expected a strong effect on growth based on previous observations of cold-acclimated *Arabidopsis thaliana* rosette plants delaying growth for a period of 7 days after switching to suboptimal temperatures (***Beine Golovchuk et al., 2018***; ***Martinez-Seidel et al., 2021a***). Such a growth difference can be a confounding variable when comparing protein synthesis rates of acclimated and non-acclimated plants. For example, a non-acclimated plant may produce more protein X (Px) in absolute terms than a cold-acclimated plant, but growth will also differ and is likely to be lower in a cold-acclimated plant. Whether a non-acclimated or a cold-acclimated plant preferentially synthesises Px can only be determined by normalizing biomass accumulation.

We selected an optimized growth measure from several variables that described morphological phenotypes of roots from germinating barley seedlings (Figure 2, Figure 2 - Figure S1 to S2 & Table S1). To this end, we monitored root growth at 12h intervals between t_0 and t_f across the germination period.

Figure 2

The roots of the control seedlings accumulated significantly more fresh weight (FW) compared to the roots of the cold-acclimated seedlings within the monitored period between 48h (t_0) and 108h (t_f) after germination (Figure 2A above). FW accumulation ceased after 60 hours and subsequently remained significantly reduced in the cold-shifted group compared to the control group. In contrast, dry weight (DW) increased equally in the cold-shifted group and the control

group, increasing significantly at 72 hours compared with 48 hours (Figure 2B above). After 72 hours, DW was constant. The cold-shifted group appeared to reduce DW, but this observation did not remain significant during the observation period. Analysis of the FW/DW ratio (Figure 2C) showed a significant difference between the cold-acclimated and control roots after 72 hours and an overall reduced ratio in the cold-acclimated roots.

Based on these observations of complex dynamic changes, we determined the RGRs by FW (Figure 2A below) and DW (Figure 2B below) at five intervals (N_t) relative to the average final root mass at t_f of the cold-shifted and control groups. We used equation 1.

$$RGR = \frac{1}{W} \cdot \frac{dW}{dt} \quad (1)$$

where W is the weight or weight proxy at time (t_f), *dW* is the weight change at time *dt*, which is the time after germination in hours. Consequently, RGR_{FW} and RGR_{DW} have units mg * mg(t_f)$^{-1}$ * h^{-1}, or in short h^{-1}. For the RGR calculation at 48h (t_0), i.e., the start of germination before the temperature shift, we set the root mass at 0h to zero. RGR_{FW} and RGR_{DW} of the control group were constant during the observation period of 48-108h with small, non-significant fluctuations. While the control group grew steadily, RGR_{FW} and RGR_{DW} of the cold-transferred group peaked at 60 and 72h, respectively. In this case, we expected transient growth, particularly a decrease in RGRs, due to the transition between optimized and suboptimal temperature regimes. Instead, we found a transient increase in the roots of the cold-acclimated seedlings, which can be explained by the initial DW accumulation after the temperature shift and the partial compensation by the fluctuating water content (Figure 2).

In previous studies on Arabidopsis seedlings, RGR was derived as the slope from log-linear regressions of growth-related variables over time (***Ishihara et al., 2015***). These systems satisfied the assumption of linearity with correlation coefficients (r^2) approaching 1. For roots of germinating barley seedlings, we had to reject the linearity assumption with r^2 less than 0.5 for all observed variables, including root length, diameter, volume, length * volume^{-1}, number of tips, or branching, as well as FW and DW (Figure 2 - Figure S3). To account for the obviously different RGRs of control and cold-acclimated roots, we chose the average of RGR_{DW} over the experimental ^{15}N labeling period, 48h (t_0) - 108h (t_f), for the required normalization (Table 1). Since protein synthesis directly contributes to DW accumulation, RGR_{DW} is the most relevant option for correcting protein synthesis rates of two experimental systems that differ in their growth rates. However, DW determination (as well as FW determination) is destructive and requires a significant sample mass. For these reasons, ^{15}N-label incorporation analyses cannot be directly paired and require additional replicated experiments. We investigated the potential of non-destructive methods for RGR determination but were unable to find a suitable replacement for RGR_{DW} (Table 1). Averaged RGRs by root length and length * volume^{-1} reflected accelerated RGR_{DW} in the cold acclimation condition, however, they did not accurately represent the excessive transient increase in RGR_{DW}, but rather corresponded to what is observed in RGR_{FW} (Table 1).

Table 1

Reprogramming of the Primary Metabolome

Primary metabolism is fundamentally reprogrammed during temperature acclimation (***Kaplan et al., 2004***; ***Guy et al., 2008***). The cold-induced reprogramming involves central metabolism,

the source of amino acid building blocks for translation. Therefore, we characterized the primary metabolome of root tips of germinating barley seedlings in the cold-acclimated and non-acclimated condition at t_f (Figure 3). Cold acclimation contributed most to the overall variance of the resulting multidimensional metabolic data set (Table S2). Principal component analysis (PCA) assigned 65% and 75% of the explained variance to PC1 of the autoscaled or non-scaled data, respectively (Figure 3C-D). The combined technical and biological variance between replicates evident in PC2 was minimal (Figure 3A). In addition to fructans and organic acids, amino acids contributed most to the variance caused by cold acclimation, as inferred from the measure of variable importance in PCA (Figure 3B). Additionally, the externally supplied ^{15}N tracer dilutes and distributes differentially among the proteinogenic amino acids, which accumulate in the cold with $\log_2$-fold changes of approximately 2-50 (Table S2). These observations highlight the need to monitor and correct for ^{15}N enrichment in each of the soluble proteinogenic amino acid pools, ideally in split and paired samples of the protein or peptide ^{15}N enrichment assays. The amino acids that contributed most to the PCA separation of the primary metabolome from cold and control samples were pyroglutamic acid (derived from glutamine converted via our extraction/derivatization procedures), cysteine, serine, homocysteine, glutamine, glycine, and glutamic acid, all of which were among the top 20 $\log_2$-fold changed metabolites between conditions.

Figure 3

Tracer Dynamics in Soluble Amino Acid Pools

In this study, we used free proteinogenic amino acids as a proxy for estimating the labelling of aminoacyl-tRNAs and monitored the ^{15}N-tracer dynamics of the soluble amino acid pools in root tips at t_f (Figure 4). We supplied a mixture of 99% ^{15}N-labelled glycine and serine to obtain a rectangular stable isotope pulse. We chose not to use inorganic ^{15}N tracers, which slowly label soluble amino acid pools (***Nelson et al., 2014b***). Inorganic ^{15}N labelling arguably leads to low ^{15}N incorporation, especially under reserve mobilization conditions of a germinating barley seedling (cf. Discussion). Consistent with our labelling strategy, soluble serine and glycine retained most of the ^{15}N tracer within root tips at 15% ^{15}N enrichment of the two amino acids in the cold-shifted group and at 2.5 - 5.0% in the control group (Figure 4, Table S3, File S1). The ^{15}N enrichment values represent the experimental ^{15}N incorporation after correction for the natural isotopic abundances of the elements (NIA). The large difference between conditions clearly indicates that additional correction between experimental conditions is required to allow comparison.

Figure 4

Further correction is required because the ^{15}N tracer was incorporated to different extents among the different proteinogenic amino acid pools under the experimental conditions. We monitored 18 proteinogenic amino acids (Figure 4). Histidine and arginine were below the detection limit in our current study. Under control conditions, glutamine, estimated by GC-MS profiling proxy, pyroglutamic acid, glutamate, and asparagine were significantly labelled at 2.5 to 5.0% ^{15}N enrichment. The cold-shifted root tips picked up to 2.5-15.0% ^{15}N labelling in glutamine, glutamate, asparagine, and additionally in proline, valine, aspartate, phenylalanine, and isoleucine (Figure 4, Table S3). The remaining monitored proteinogenic amino acids and beta-alanine, a non-proteinogenic amino acid control, did not absorb ^{15}N. Our analysis provided accurate ^{15}N enrichment of most proteinogenic amino acids that could be paired with protein and peptide enrichment measurements. Because even minor contributions from multiply labelled amino acids add up to substantial ^{15}N incorporation into peptides, failure to account for these contributions may introduce bias into estimated protein synthesis rates. This confirms the need to study the dynamics of the internalized tracer.

Protein Synthesis during Transition from a Physiological Steady State

Throughout their lifespan, plants constantly transition through physiological and proteomic states that adapt to developmental and environmental factors (***Nelson and Millar, 2015***). Finding conditions that approach a steady state and allow assessment of protein turnover using stable isotope mass spectrometry to track both synthesis rates (K_s) and degradation rates (K_d) of specific proteins is no easy task. Like many other plant systems that respond to stressors, the root of the barley seedling acclimated to cold is constantly changing (Figure 2) and did not reach an equilibrium state within our observation period. Therefore, we determined K_s over the observed time interval rather than turnover.

We based our calculations on two published strategies used to determine K_s from turnover calculations of plant proteins (***Ishihara et al., 2015***; ***Li et al., 2017***). Both of these studies normalize K_s of individual proteins using growth and protein accumulation rates, as described in the Methods section by equations 3a & 3b (***Ishihara et al., 2015***) and 4a, 4b, 4c & 4d (***Li et al., 2017***). Specifically, we determine the ^{15}N enrichment of peptides, consider ^{15}N enrichment in soluble proteinogenic amino acid pools, and correct K_s by relative growth transformed into relative protein accumulation rates. Equation 2a calculates K_s as the product of labelled peptide fraction (LPF) times a modified version of RGR ($\bar{RGR}_{pf}$ in equation 2b) times a factor of 100, which ensures that K_s units are expressed as a percentage (%) of the normalized labelled peptide fraction accumulated per unit of protein weight per hour. (equation 5a).

$$K_s = LPF \cdot \bar{RGR}_{pf} \cdot 100 \tag{2a}$$

Since our study is not at a biological steady state, we introduced the modified $\bar{RGR}_{pf}$ calculation. First, we calculate the average RGR_{DW} over the labelling period ($\bar{RGR}_{DW}$), i.e., the observed sum of the measured RGR_{DW} of the analyzed time intervals between t_0 and t_f divided by the number of time intervals (N_t), replacing *dW* (weight accumulation at time t) with P_f (equation 2b).

$$\bar{RGR}_{pf} = \frac{\sum_{t=0}^{f} \left(\frac{1}{W_{tf}} \cdot \frac{P_f}{dt} \right)}{N_t} \tag{2b}$$

The factor P_f is used to convert the RGR_{DW} into a relative accumulation rate of total protein with respect to DW (RGR_{pf}). To this end, we determined P_f, which is the ratio of the final total protein mass (mg [P_{pf}]) to the dry mass at time t (mg [*dW*]), equation 2c. For both empirical measurements in milligrams, this process cancels the units and converts them to a fraction of the total final protein relative to the cumulative weight.

$$P_f = \frac{mg_{prot}[P_{pf}]}{mg_{DW}[dW_t]} \tag{2c}$$

To calculate the labelled peptide fraction (LPF, equation 2d), we extracted the distributions of the mass isotopologs from the parent ion masses of LC-MS/MS data sets. We calculated the expected parent ion monoisotopic masses of the peptides based on their molecular formula derived from the known amino acid composition. We determined the isotopolog abundances at mass intervals corresponding to the mass-to-charge ratio of the peptide. These initial isotopolog distributions were corrected for the natural isotopic abundances (NIA) of the elements according to their molecular formula. The resulting NIA-corrected isotopolog distributions exclusively reflected the experimental ^{15}N labelling and allowed the calculation of the fractional ^{15}N enrichment of peptides, i.e., the ratio of ^{15}N atoms in a peptide to the sum of all N atoms. Finally, the fractional enrichment or non-corrected LPF is corrected by a constant that differs for each peptide as a

quotient, equation 2d.

$$LPF = \frac{\frac{NIA_{corr}(^{15}N_{pep})}{NIA_{corr}(^{14}N_{pep}) + NIA_{corr}(^{15}N_{pep})}}{^{15}N_{Aver.AA}} \quad (2d)$$

The $^{15}N_{Aver.AA}$ needs to be the quotient dividing non-corrected LPF in order to increase the fractional enrichment in individual peptides, which assumes a fully labelled source, by what is actually the achieved labelling, which is always only fractional given the partial labelling in soluble amino acid pools. Thus, the varying condition-dependent ^{15}N incorporation into soluble proteinogenic amino acids and the amino acid composition of peptides determine the maximum fractional enrichment that peptides can achieve. To account for these factors, we correct the fractional ^{15}N enrichment of peptides by dividing by a peptide- and condition-specific correction factor ($^{15}N_{Aver.AA}$ in equation 2e) to obtain a corrected version of the LPF. $^{15}N_{Aver.AA}$ is the average NIA-corrected fractional ^{15}N enrichment over all amino acids in a peptide assuming that the fractional ^{15}N enrichment of each amino acid incorporated into protein is equal to its observed fractional ^{15}N enrichment in the soluble amino acid pools, Equation 2e. In other words, $^{15}N_{Aver.AA}$ corresponds to the maximum fractional ^{15}N enrichment that each peptide can achieve under specific labelling conditions. $^{15}N_{Aver.AA}$ only considers the labelled amino acid residues because these are entered as potentially labelled N atoms to define the combinatorial matrix used to correct for NIA. Thus, unlabelled soluble amino acids have no effect on our calculations.

$$^{15}N_{Aver.AA} = \frac{\sum_{i=0}^{n} AA_s}{N_{aa}} \quad (2e)$$

Consistent with an expected immediate rectangular ^{15}N label incorporation into soluble amino acid pools, we used the NIA-corrected ^{15}N incorporation into amino acids as determined at t_f (***Ishihara et al., 2015***). We tested an alternative scenario for delayed incorporation by modelling incorporation as a linear function between t_0 and t_f (Table S4F and File S2.1 & S2.2). This leads to a more conservative trend of enrichment incorporation. Otherwise, the assumption of rectangular incorporation would mean that the average labelling in soluble amino acid pools over the experimental period is overestimated. Nevertheless, because of the large increase in peptides exceeding the maximum possible LPF (> 1.0), we rejected the alternative assumption of substantially delayed incorporation of label into soluble amino acid pools. Instead, we used the maximum possible LPF as a reference to accept or reject low-enriched soluble amino acids as part of the correction factor and thus be able to decide on the correct amino acid combination.The complete workflow for data mining and computation of our results (Figure 5) is provided by the ProtSynthesis R package, which contains detailed code annotations and descriptions of the computational procedures used in this and previous studies (***Ishihara et al., 2015***; ***Li et al., 2017***). The complete workflow (Figure 5) and its usage details are deposited in two GitHub repositories. Namely, the repository ProtSynthesis, from which the R package can be installed directly in any R environment, and the repository isotopeEnrichment, which contains the usage instructions and the Python function that allows direct mining of peptide isotopolog abundances.

Figure 5

Synthesis and Accumulation of Macromolecular Complexes during Cold

To validate our method, we obtained a ribosome-enriched fraction of the barley root tip proteome by filtering a cell lysate through a 60% sucrose cushion, recovering the pelleted fraction. This ensured that only assembled macromolecular complexes were monitored. The comparative fractions obtained were from treated and control seedlings. Using the same extraction procedure,

the total protein content of cell complexes was significantly higher in the roots of treated plants than in the roots of control plants (Figure 5 - Figure S1 and Table S5). Using the LFQ-normalized protein abundances (***Zhang et al., 2012***) of peptides extracted from the recovered fraction, we then report what fraction of the monitored complexes accumulate in barley root tips at sub-optimal low compared with optimized rearing temperatures (Table 2). At the same time, we monitored the incorporation of ^{15}N into the individual protein components of these complexes and found 1379 good quality peptides after applying our method (Figure 5 - Figure S2 and Table S4G), from which we can confidently report fractional synthesis rates. From this information, we can estimate what part of the complexome proteome accumulation is due to protein synthesis and what part is due to the lack of protein degradation (Table 2).

Table 2

There are four groups of responses for protein-complexes and their components in Table 2. Group one contains proteins that accumulate and are preferentially synthesised at a specific temperature. Group two contains proteins that accumulate due to lack of protein degradation because they do not incorporate the nitrogen isotope. Group three contains proteins that do not accumulate and nevertheless are preferentially synthesised at a specific temperature, implying high turnover. Group four contains proteins that are detected but do not accumulate nor are preferentially synthesised. The three significant groups (1-3) can be found at sub-optimal low temperature whereas only group one and two are found at optimal temperature.

Altered Ribozyme-Mediated Proteome Remodelling

The global ontology term of cytosolic translation in Table 2, which includes ribosome biogenesis, has proteins that belong to the three significant groups of responses (1-3) at both temperature regimes.

The accumulation dynamics of ribosome biogenesis complexes, which give rise to mature and translationally competent ribosomes, provides insight into the origin of assembled ribosomes. For example, the 90S pre-ribosome in the nucleolus leads to pre-60S and pre-40S complexes. Following their maturation, pre-40S complexes are shaped by the small-subunit processome. Protein components from all these four types of biogenesis complexes significantly accumulate at sub-optimal low temperature. Interestingly, the small-subunit processome features proteins from group one, i.e., accumulating due to *de novo* synthesis. Whereas the other three complexes accumulate due to lack of degradation (group two). This implies that the only remodelled complex from the biogenesis subset is the small-subunit processome, while the others keep functioning in the same state as that from plants growing at optimised temperature.

In terms of assembled cytosolic ribosomes, their structural protein components, as well as those from mitochondrial ribosomes, are accumulated preferentially at optimised temperature. The cytosolic ribosome components are preferentially synthesised, which categorises them in group one. In contrast, the mitochondrial ribosome components are not preferentially synthesised and thus accumulate due to lack of degradation (group two). On the other hand, the protein structural components of the cytosolic large ribosomal subunit are preferentially synthesised but not accumulated during cold, which categorises them in group three and indicates a remodelling aspect that is coupled to high turnover of these complexes at sub-optimal temperature.

Translation initiation complexes preferentially accumulate only at sub-optimal low temperature and, all of them belong to group one, where their proteins accumulate due to *de novo* synthesis.

Beyond the translation ontology term, many of the detected protein complexes that preferentially accumulated at low sub-optimal temperature belonged to group one, where their protein components are also newly synthesised. Two major ontological groups stand out as being newly synthesised by ribosomes and accumulated during cold. In brief, cellular machinery to cope with protein misfolding and aggregation is newly synthesised and accumulated (CCT complex protein components and heat shock proteins) as well as cellular complexes that mediate remodelling of the cell walls and cellular membranes. Thus, this prompted us to analyse in more depth the extent of triggered ribosome heterogeneity and its potential structural link to the observed proteome shift that happens due to protein synthesis by ribosomes.

Recycled and Remodelled Ribosomes Accumulate during Cold Acclimation

To characterise cold-induced rProtein heterogeneity and decipher its origin, we adjusted the protease digestion to the requirements of a highly basic ribosomal proteome (Figure 6 - Figure S1 and Table S6), and used the optimized method to profile ribosome-enriched barley proteome extracts. To validate that our method enabled recovery of native ribosomes, we subjected *Escherichia coli* 70S ribosomes to the same purification method and assessed the completeness of the recovered ribo-proteome. We found 21/21 30S small subunit rProteins and 33/33 50S large subunit rProteins, which featured reproducible abundances in triplicated measurements (Figure 6 - Figure S2 and Table S7). We then calculated protein abundances, relative stoichiometry, and fractional synthesis rates for ribosome structural protein components of the barley extracts at the onset of the physiological transition from optimized germination conditions to sub-optimal low temperatures (Figure 6 and Table S4H).

Figure 6

Previously, we observed that rProteins, when averaging ribosome-bound and ribosome-free forms, increase in abundance in barley root tips of germinating seedlings subjected to cold acclimation (***Martinez-Seidel et al., 2021c***). Here, we found reliable LFQ intensities for 17 rProtein families from the small 40S subunit (SSU) and 38 rProtein families from the large 60S subunit (Table S4C), all of which were bound to ribosomal complexes. Among these 55/80 high confidence rProtein families, a total of 95 paralog genes were identified.

Ribosomal Protein Substoichiometry

The sum of SSU-rProtein abundances correlated linearly over an r^2 of 0.98 with the sum of LSU-rProtein abundances across all samples, maintaining a constant ratio of 3x LSU to 1X SSU (Figure 6 - Figure S3 and Table S4C). Nevertheless, the LFQ abundances of all identified paralogs decreased in their ribosome-bound form during cold acclimation, either significantly (Table S4B) or not. Thus, the control seedlings had in average more 40S and 60S assembled subunits in their root tips. Consequently, we used the sum of 40S proteins to normalize the individual rProtein abundances of SSU and the sum of 60S proteins to normalize the individual rProtein abundances of LSU in order to correct for the relative amount of complexes across samples, as was previously reported (***Martinez-Seidel et al., 2021a***). The normalization allowed us to determine whether these complexes exhibit induced substoichiometry in their rProtein compositions (Figure 6A).

The population of 40S subunits was enriched in four rProtein paralogs during cold, namely eS10 (HORVU3Hr1G111760), eS1 (HORVU1Hr1G032060 and HORVU4Hr1G070370), and eS6 (HORVU2Hr1G010870). Thus, the population of 40S subunits in barley root tips is not canonically complete and sometimes these paralogs are absent compared with the cold population. The population of 60S subunits contains paralogs that are relatively depleted or accumulated in cold conditions. The rProtein families P2 (HORVU1Hr1G073640), uL16 (HORVU1Hr1G024710),

eL13 (HORVU7Hr1G067060), eL18 (HORVU2Hr1G018820), eL31 (HORVU7Hr1G050170), eL36 (HORVU5Hr1G009600), uL4 (HORVU4Hr1G075710), eL34 (HORVU7Hr1G071240), uL29 (HORVU2Hr1G068120), eL21 (HORVU1Hr1G038890), uL13 (HORVU5Hr1G096060 and HORVU2Hr1G063900), eL24 (HORVU3Hr1G080130 and HORVU5Hr1G111510) are depleted during cold. The rProtein families P1/P2/P3 (HORVU7Hr1G075360), eL30 (HORVU0Hr1G023290), eL43 (HORVU1Hr1G085170), uL18 (HORVU2Hr1G073320) are accumulated during cold.

Altered Ribosomal Protein Synthesis and Ribosome Remodelling

We next examined rProtein synthesis rates to understand what constituted the newly synthesised rProtein substoichiometry (Figure B-C). In general, the cold-induced changes in rProtein synthesis did not coincide with substoichiometry, suggesting independence between rProtein synthesis and ribosome assembly/remodeling. The population of 40S subunits was assembled or remodeled using four rProtein paralogs that were significantly more synthesised at optimized temperature, namely eS8 (HORVU6Hr1G056610), uS17 (HORVU2Hr1G067370), eS4 (HORVU1Hr1G021720), eS1 (HORVU1Hr1G032060). Similarly, two rProtein paralogs were significantly more synthesised during cold: eS10 (HORVU3Hr1G111760), eS17 (HORVU6Hr1G056610). The population of 60S subunits was assembled or remodeled using several rProtein paralogs, which were significantly more synthesised at optimized temperature or during cold. Paralogs uL10 (HORVU7Hr1G073720), eL18 (HORVU2Hr1G018820), uL23 (HORVU2Hr1G086360), uL18 (HORVU2Hr1G073320), eL6 (HORVU7Hr1G00206), eL21 (HORVU1Hr1G038890), eL22 (HORVU2Hr1G019160), uL29 (HORVU2Hr1G068120), eL43 (HORVU1Hr1G085170), uL22 (HORVU5Hr1G052280), uL1 (HORVU7Hr1G059090) were preferentially synthesised and assembled at optimized temperature. Paralogs uL16 (HORVU1Hr1G024710), uL3 (HORVU4Hr1G019980), eL19 (HORVU2Hr1G018700), uL1 (HORVU3Hr1G084310 and HORVU1Hr1G085730), uL18 (HORVU5Hr1G092630 and HORVU2Hr1G073320), eL6 (HORVU7Hr1G00206), eL28 (HORVU1Hr1G079370), uL4 (HORVU4Hr1G075710), eL8 (HORVU7Hr1G054670) were preferentially synthesised and assembled in the cold.

From our results, five types of paralog-specific and rProtein family ribosome association and synthesis dynamics can be deduced:

1. **Paralog switches:**
   - based on protein synthesis, the uL1 paralogs HORVU3Hr1G084310 and HORVU1Hr1G085730 (cold) and HORVU7Hr1G059090 (control).
   - based on substoichiometry, P1/P2/P3 paralogs HORVU7Hr1G075360 (cold) and HORVU1Hr1G073640 (control).
2. **Families with paralogs sharing ribosome-bound accumulation or synthesis dynamics:**
   - based on protein synthesis, uL18 HORVU5Hr1G092630 and HORVU2Hr1G073320 (cold-specific); uL1 HORVU3Hr1G084310 and HORVU1Hr1G085730 (cold-specific).
   - based on substoichiometry, eL24 HORVU3Hr1G080130 and HORVU5Hr1G111510 (control-specific); uL13 HORVU5Hr1G096060 and HORVU2Hr1G063900 (control-specific); eS1 HORVU1Hr1G032060 and HORVU4Hr1G070370 (cold-specific).
3. **Paralog splice variants (peptides from the same protein with different synthesis dynamics under cold and control conditions):**
   - uL10 HORVU7Hr1G073720 (one peptide from exon 5 is cold synthesized and one from exon 4 cold synthesized).
4. **Paralogs that share ribosome-bound accumulation and synthesis dynamics:**
   - eS10 HORVU3Hr1G111760; eL18 HORVU2Hr1G018820; eL21 HORVU1Hr1G038890; uL29 HORVU2Hr1G068120; uL18 HORVU2Hr1G073320

5. **Paralogs with inverse ribosome-bound accumulation and synthesis dynamics:**
   - accumulated in control ribosomes but preferentially synthesised in cold; uL16 HORVU1Hr1G024710; uL4 HORVU4Hr1G075710
   - accumulated in cold ribosomes but preferentially synthesised during control; eS1 HORVU1Hr1G032060; eL43 HORVU1Hr1G085170

Discussion

Morphological Phenotype of Barley Roots during Low Temperature Germination

At the physiological level, plants exhibit a growth arrest during the first week of cold acclimation (***Beine Golovchuk et al., 2018***; ***Martinez-Seidel et al., 2021a***,c). *Arabidopsis thaliana* roots reduce mitotic division but not cell elongation at a sub-optimal temperature of 4°C, which significantly reduces meristem size (***Ashraf and Rahman, 2019***). Similarly, barley roots from acclimated seedlings reduce their protein content (***Martinez-Seidel et al., 2021c***), which is mainly related to dry weight accumulation and thus by proxy to mitotic division, suggesting that the cold phenotype of barley and Arabidopsis may share this aspect. In our system, the root length and volume of non-acclimated seedlings increased significantly and steadily compared to the acclimated counterparts, which was enhanced by water accumulation as shown by differences in fresh weight. Conversely, root dry weight did not differ between acclimated and non-acclimated seedlings. The ratio of fresh weight to dry weight remained constant at the end of the acclimation period, and yet there was a transient relative increase in dry weight accumulation from the second to the third day causing a significant imbalance in the dry to fresh weight ratio of acclimated seedlings. In consequence, the dynamics of dry weight accumulation during germination of acclimated barley seedlings are not comparable to their non-acclimated pairs and, therefore, global analyses of protein turnover need to account for this difference.

Cold Metabolic Phenotype and Testable Links to Translational Responses

In spite of not growing, roots from acclimated barley seedlings show a transition to cold-induced metabolic states. After two days of cold treatment (4 °C) in the dark, glucose increases in barley seedlings, while proline, sucrose, and total lipids decrease (***Zúñiga et al., 1990***). Thus, there is a transient decrease in the abundance of these compounds during the early stages of acclimation, coinciding with the peak of dry weight accumulation reported in our study. The transient decrease in metabolites could subsequently attenuate and then increase again at later stages of acclimation. Transcriptional studies in barley leaves on the third day of cold acclimation (3°C during the day, 2°C at night) predict the accumulation of sugars and polyols such as maltose, glucose, trehalose, and galactinol (***Janská et al., 2011***), and we show that glucose and sucrose were accumulated on the fifth day of acclimation (maltose was not accumulated, and galactinol and trehalose were not detectable). In contrast, the amino acid biosynthetic pathway is not predicted to be upregulated at the transcriptional level, and yet we observed that 25 of the 29 amino acids we detected (including the well-known osmoprotectant proline) were accumulated under cold conditions compared with the optimal temperature. Thus, a cold-metabolic state in our system is consistent with evidence for potential translational control that influences the acclimation response by differentially impacting the amino acid biosynthesis pathway. Amino acid pools can increase from mobilised nitrogen resources or from enzymatic synthesis, the latter of which requires the accumulation of specific proteins through direct or indirect translational control, because amino acid biosynthesis is not predicted to be upregulated based on barley cold-transcriptional dynamics (***Janská et al., 2011***). Our report demonstrates that some of the accumulated amino acids also incorporated ^{15}N during cold, suggesting that they may be in part newly synthesized and not just degradation products of storage proteins, as will be discussed in the following paragraph. The role of all accumulated soluble sugars, amino acids, and polyols in the context of cold acclimation is thought to be that of an osmoprotector, i.e., compounds that stabilise proteins and membranes and thus contribute to

freezing tolerance (***Rontein et al., 2002***).

Amino Acid Metabolism and ^{15}N Isotopic Flux

How nitrogen uptake and supply occurs in germinating barley seedlings determines the best strategy for isotope flux studies in this system. Most of the nitrogen resources used by germinating barley embryos come from degraded storage proteins located in the endosperm during germination (***Ma et al., 2017***; ***Rosental et al., 2014***; ***Nonogaki, 2008***; ***Lea and Joy, 1983***). Thus, nitrogen transport into the embryo in the form of amino acids and peptides is critical for controlling and setting efficient germination. For example, nitrogen transport and reassimilation is fundamental for the development of gene expression programs in barley caryopses (***Mangelsen et al., 2010***). Consequently, germinating barley embryos activate genes involved in biosynthesis, metabolism, and transport of amino acids at an early stage of 2 to 3 days after germination (***Sreenivasulu et al., 2008***), with peptide transporters considered particularly critical for normal germination processes (***Waterworth et al., 2000***). At the proteome level, nitrogen mobilization systems that supply nutrients to the growing embryo are induced and activated (***Osama et al., 2021***). For example, proteases, including carboxypeptidases and aminopeptidases, provide peptide or amino acid substrates that are released, transported, and used during germination (***Sreenivasulu et al., 2008***; ***Shutov and Vaintraub, 1987***; ***Hammerton and Ho, 1986***; ***Dal Degan et al., 1994***). Similarly, just prior to radicle sprouting, genes encoding proteins involved in amino acid biosynthesis and transport are upregulated, whereas genes involved in amino acid degradation are largely unresponsive (***Ma et al., 2017***). This suggests that nitrate reductase activity is not required to reassimilate nitrogen from amino acid catabolism. Our results suggest that after feeding enriched amino acids, the spread of the tracer across all proteinogenic soluble amino acid pools is rather limited and only increases at low sub-optimal temperature. Thus, it appears that amino acid degradation and reassimilation are suppressed processes during barley germination at optimized temperature. Instead, barley seeds may be genetically tuned to rely on amino acid mobilization during the early stages of embryo development. Therefore, using labelled amino acids to introduce the tracer into germinating barley seedlings may be the best and only strategy to follow *in vivo* isotopic fluxes into protein.

Germinating barley seedlings have at least four systems for successful amino acid uptake (***Salmenkallio and Sopanen, 1989***), all of which depend on storage proteins or their hydrolysis products being taken up into the scutellum for further hydrolysis and utilization (***Higgins and Payne, 1981***). Thus, the supply of ^{15}N-labeled amino acid compounds in the germination media ensures that these nitrogen atoms are introduced into and utilized by the plants. However, because of the generous availability of endogenous amino acid resources, the incorporated ^{15}N-labeled amino acids are diluted in the roots of germinating seedlings. Moreover, at low temperatures, all enzymatic activities and cellular dynamics slow down. Therefore, mobilization of amino acids and peptides for nitrogen supply during germination is also likely to be affected by lower temperatures. Our results suggest that barley seedlings subjected to acclimation take up more labelled amino acids through their roots and use / spread their nitrogen supply across soluble amino acid pools. Thus, it is possible that nitrogen deficiency resulting from slowed nutrient mobilization is compensated for by increased uptake of nutrients through the roots, and since amino acid and peptide transporters are already available from the germination process, these compounds would be adsorbed. The bottom line is that the physiological transition triggered by acclimation to low temperatures causes differential incorporation of amino acids carrying the tracer, differential spread of the tracer across amino acid pools and different accumulation of soluble amino acids, and all of these differences must be accounted for if biological insights are to be derived from tracking the tracer incorporation into polypeptides.

Ribozyme-mediated ^{15}N Incorporation Into Protein

In all living organisms, the proteome is synthesised by ribosomes, whose ribozyme activities catalyse the formation of peptide bonds between the existing peptidyl-tRNA and the subsequent aminoacyl-tRNA (***Rodnina, 2013***). Thus, the natural pathway of ^{15}N-labeled amino acids is to conjugate with tRNAs and be transported to ribosomes, where they enter the elongation cycle and end up as a monomer in a synthesised polypeptide. Amino acids exist as soluble pools in the cytoplasm and are loaded onto aminoacyl-tRNAs, which are present in much lower proportions as compared to amino acid pools and are much more labile, i.e., their turnover is extremely rapid (***Gomez and Ibba, 2020***), suggesting that the enrichment in soluble amino acid pools is a valid proxy for isotope enrichment in aminoacyl-tRNA conjugates.

The main activity of ribosomes is autocatalysis (***Reuveni et al., 2017***), and as such the tracer is expected to be incorporated first into the machinery within one degree of ribosomes (***Bowman et al., 2020***), which include rProteins, aminoacyl-tRNA synthetases, tRNAs, initiation, elongation and release factors. The cellular proteome within one degree of ribosomes is part of macromolecular complexes. Thus, by purifying a complexome proteome, one can recover translation-related multiprotein complexes in a near-native state while co-purifying other complexes. In this way, it is possible to test the link between ribosome structural divergence and altered rates of protein synthesis at sub-optimal low temperature. Altered protein synthesis can be caused by direct or indirect translational control determining which transcripts are translated under the limited growth of cold acclimation. Direct translational control implies an altered and selective ribozyme-functionality shaping the proteome. In our system, translation during cold is carried out by a ribosomal population that is heterogeneous and substoichiometric in its rProtein composition. Altered rProteome compositions confer metazoan ribosomes the ability to selectively recruit transcripts for translation, i.e., to specialize (***Shi et al., 2017***; ***Genuth and Barna, 2018***). Additionally, Plants have an increased number of rProtein paralogs compared to all higher metazoans (***Barakat et al., 2001***), and the fate of duplicated genes usually leads to novel and divergent functions (***Kosová et al., 2021***). Thus, it is probable that specialized rProtein proteoforms may equip heterogenous ribosomes to perform direct translational control, efficiently adapting them to cold temperatures.

Translational Dynamics of Heterogeneous Ribosomes

In Arabidopsis, cold heterogeneous translating ribosomes exhibit rProtein substoichiometry around the polypeptide exit tunnel (PET), with many of the rProteins being relatively removed during cold (***Martinez-Seidel et al., 2021a***). Here, we report that barley ribosomes also exhibit, on average, subtractive heterogeneity (***Briggs and Dinman, 2017***) in the cold-ribosomal population around protein uL4 and uL29, the former being essential for PET assembly during ribosome biogenesis (***Lawrence et al., 2016***; ***Gamalinda and Woolford, 2014***; ***Stelter et al., 2015***; ***Pillet et al., 2015***), as its internal loops form the constriction sites of the nascent PET (***Micic et al., 2022***) along uL29. The PET and its assembly are likely to be particularly critical during cold acclimation because both yeast (***Hung and Johnson, 2006***) and plants (***Schmidt et al., 2013***) have a 60S maturation factor that when knocked out, leads to cold sensitivity, namely Rei-1 in yeast and its homolog REIL in plants. The functional role of Rei-1 in yeast is to insert its C-terminus into the PET to check the integrity of the tunnel as a quality control step before making 60S subunits translationally competent (***Greber et al., 2016***). Thus, subtractive rProtein heterogeneity near the tunnel could indicate higher rRNA disorder, defective tunnel assembly, and/or defective structure, causing the observed need for PET quality control during cold.

On the other hand, the 60S rProteins accumulated in the cold population of ribosomes, uL18 and eL30, are located near important intersubunit bridges (***Martinez-Seidel et al., 2021b***; ***Tamm et al., 2019***). Similarly, the population of 40S subunits, which shows accumulation of specific rProteins only during cold, has two rProteins, eS6 and eS1, that also form important intersub-

unit bridges in the form of connections between the 40S and 60S and their constituent rProteins (***Martinez-Seidel et al., 2021b***; ***Tamm et al., 2019***). The third rProtein more abundant in 40S subunits, eS10, links the large uS3 hub (containing the ribosomal region adjacent to the tRNA-mRNA entry sites) to the uS13-uL11 subunit bridge (***Martinez-Seidel et al., 2021b***). Bridges between subunits in bacteria have been shown to directly affect initiation factor-dependent translation (***Kipper et al., 2009***). Thus, these observations suggest that the rProteins accumulated during cold in ribosomal populations are related to subunit connectivity and may influence their association during initiation, elongation or termination.

Translation Initiation: Newly Synthesised Complexes

Complexes related to translation initiation were accumulated during cold acclimation in our system due to synthesis of their protein components, implying tight control over what type of translation initiation complexes form and participate in 40S transcript association. Translation initiation is a sequential and complex process that is highly conserved (***Jackson et al., 2010***; ***Hashem and Frank, 2018***) and nonetheless exhibits peculiarities in its regulation in plants (***Castellano and Merchante, 2021***). Translation initiation begins with the binding of multiple factors to the 40S subunit to form a 43S pre-initiation complex (PIC) (***Aylett et al., 2015***; ***Hashem et al., 2013***; ***Majumdar et al., 2003***), which then binds the mRNA to be translated, supported by multiple factors, to form the 48S initiation complex (IC) (***Brito Querido et al., 2020***; ***Pisareva and Pisarev, 2014***). Finally, the IC is supported by several factors to allow the 60S subunits to connect, making the elongation process competent in the newly formed 80S monosome (***Fringer et al., 2007***; ***Shin et al., 2002***). In our study, we found that several protein components of the initiation machinery are both significantly accumulated and synthesised during cold:

1. First, the eukaryotic translation initiation factor 3 subunits A, B, C, and E (eIF3A-C,E). The eIF3 complex consists of 13 subunits (A-M) and is the most complex initiation factor in eukaryotes and also the largest (***Des Georges et al., 2015***; ***Zhou et al., 2008***). Moreover, eIF3 has been associated with various pathological conditions in higher metazoans (***Gomes-Duarte et al., 2018***). Subunits A and C bind eIF3 to 40S subunits via the platform on the solvent side (***Aylett et al., 2015***) and can also interact with eIF1 and eIF4G via subunit E (***LeFebvre et al., 2006***). Thus, 3/4 of the preferentially accumulated and synthesised eIF3 subunits serve as anchors between ribosomes and mRNA recruitment factors. Subunit B is part of the eIF3b-i-g module and presumably interacts with the 40S subunit directly at the mRNA entry channel by occupying it (***Chiu et al., 2010***). Accumulation of these specific subunits of the eIF3 complex is associated with cancer in humans via increased (***Scoles et al., 2006***; ***Xu et al., 2012***; ***Wang et al., 2013***) and selective (***Dong et al., 2004***; ***Parasuraman et al., 2017***) translational output.

2. Second, eukaryotic translation initiation factor 2 subunit 1 (eIF2α). This eIF catalyses the first step of 40S - initiator-tRNA (Met-tRNA) association (***Hinnebusch, 2017***). This factor is the central element of the integrated stress response in eukaryotes (***Pakos-Zebrucka et al., 2016***), as it leads to a global decrease in protein synthesis through a phosphorylation event mediated by eIF2α kinases, while promoting the selective translation of specific transcripts whose protein products are required for survival (***Lu et al., 2004***). In this case plants may be using this robust and well-characterized stress response for successful acclimation to sub-optimal low temperatures.

Importantly, the significant accumulation of a protein fraction enriched in rProteins during cold, which we reported previously (***Martinez-Seidel et al., 2021c***) and demonstrated again in this study (Figure 5 - Figure S1), originated from complexes related to ribosome biogenesis and translation initiation, highlighting the functional importance of translation initiation during cold acclimation and

assigning a potential regulatory and functional role to the group of cold heterogeneous rProteins. The accumulation of machinery at both sides of competent ribosomes, i.e. pre-ribosomes and translation initiation complexes, along with the mantained ratio of 40S to 60S subunits suggests that the limiting step during cold acclimation is successful initiation. Thus, the set of competent 60S subunits assembled during cold might select which transcript to translate based on an excess of PICs and ICs.

Ribosome Biogenesis: Assembled and Remodelled Ribosomes

The increasing complexity uncovered in the process of ribosome biogenesis suggests that the highly energy demanding process of assembling ribosomes is connected to major environmental and developmental cellular responses (***Lindahl, 2022***). In our study, ribosome biogenesis complexes accumulated during cold acclimation due to the lack of degradation, as their protein components did not take up the ^{15}N tracer and yet were significantly more abundant during cold compared with control conditions. The only pre-ribosomal complex that accumulated newly synthesised protein components was the small subunit processome. The small subunit processome is the earliest pre-40S complex found to date in eukaryotes, and it uses many accessory factors to process and mature 40S subunits (***Barandun et al., 2017***). Therefore, the protein components that are newly synthesised during cold might indicate alternative processing of pre-40S subunits, which could be related to the reported cold-specific accumulation of 40S rProteins in assembled SSU complexes. At the structural rProtein level, there were fewer competent ribosomes during cold, and only 60S subunit components were generally and preferentially synthesised during cold, to such an extent that GO enrichment of the 60S structural component category was detected when the cold-synthesised proteome was examined. Thus, our results suggest that there is restructuring due to altered LSU rProtein synthesis in cold-acclimated 60S large subunits and variability in processing of pre-40S small subunits of cytosolic ribosomes due to differential protein synthesis of components from the small subunit processome. Both aspects are complemented by increased abundances of ribosome biogenesis complexes, suggesting that ribosome heterogeneity arises in part from the ribosome assembly line at low sub-optimal temperatures.

At the individual protein level, it is clear that ribosomes are assembled or remodelled using new and old rProteins. Only a subset of rProteins significantly incorporated the tracer ^{15}N, confirming the previously observed fact that in plants cytosolic rProteins exhibit the greatest variability in degradation rates among protein components of large cellular complexes (***Li et al., 2017***). This variability makes economic sense, as ribosome assembly and protein biosynthesis impose the greatest cellular costs (***Shore and Albert, 2022***) and continued synthesis of each component within the translational apparatus would be detrimental. In addition, rProteins in plants have a half-life of about 4 days (***Salih et al., 2020***), and given the slower cell dynamics at cold temperatures, relying solely on ribosome biogenesis to control translational dynamics would be too slow. Therefore, remodelling old ribosomes to adapt them for the work at hand could be an efficient way to alter their function. For example, in higher metazoans, ribosomes in neuropil (far from the nucleolus) are remodelled *in situ* rather than undergoing a new cycle of ribosome biogenesis and subsequent transport to dendrites and axons, and this is a means of regulating local protein synthesis depending on the cellular context (***Fusco et al., 2021***). Whether this is the case in plants remains to be tested, because we do not report rRNA synthesis rates required to determine whether a complete biogenesis cycle generated the heterogeneous ribosomes using new and old rProteins or whether, on the contrary, these ribosomes were remodelled in the cytoplasm.

Translational Outcome of Heterogenous Ribosomes: A Proteome Shift

The assembled and remodelled heterogeneous ribosomes are able to cause a significant part of the proteome shift observed during cold (the rest of the shift is due to the lack of degradation of specific proteins). In addition to complexes related to translation, cold-remodelled ribosomes

significantly affect the synthesis and accumulation of protein folding machinery, complexes from the endoplasmic reticulum (ER) and Golgi, nuclear complexes and complexes related to the cell cycle, cell wall and microtubule complexes, and protein complexes from the outer mitochondrial membrane. All of these complexes and their individual proteins could be of great importance for acclimation, as the plant accumulates them beyond the level reached in plants grown at optimal temperature, despite its limited resources and slow growth dynamics.

We found that 6/8 subunits of the cytosolic chaperonin T-complex-protein 1 ring complex or chaperonin-containing TCP-1 (CCT) are preferentially synthesised during cold, leading to accumulation of the complex, which may be directly related to the altered functionality of cold heterogeneous ribosomes. The CCT binds and promotes protein folding of newly synthesised polypeptides (***Lopez et al., 2015***; ***Yébenes et al., 2011***) or promotes their aggregation and thus protein degradation to maintain proteostasis (***Lopez et al., 2015***; ***Hartl et al., 2011***; ***Spiess et al., 2004***). We have shown that during cold in plants, ribosome remodeling, i.e., subtractive heterogeneity, occurs in the proteome surrounding the PET, and the signature of a defective tunnel is protein misfolding (***Micic et al., 2022***; ***Peterson et al., 2010***; ***Wruck et al., 2021***). Thus, it is conceivable that an altered tunnel structure leads to increased protein misfolding and this forces the plant cell to produce more CCT complexes to properly fold or aggregate misfolded proteins in order to fix or degrade them, respectively. Moreover, we found that several heat shock proteins are preferentially synthesised and accumulated at cold temperatures, underscoring that protein misfolding is an urgent problem that plants need to address during acclimation to sub-optimal low temperatures.

We also found that nuclear and cell cycle complexes were preferentially synthesised and accumulated. Among them was condensin, which in addition to its role in the cell cycle promoting chromosome assembly, is also known to directly regulate gene expression (***Iwasaki et al., 2019***; ***Li et al., 2015***). Plants stop their mitotic activity in response to cold (***Ashraf and Rahman, 2019***), and thus condensin is less likely to accumulate to promote further cell cycle progression, but rather may accumulate to promote mechanisms of transcriptional control in response to cold.

All other preferentially synthesised and accumulated complexes can be classified into the machinery that transports and targets the cell membrane and wall. Among this type of complexes we found ER and Golgi components as well as cell wall and microtubule proteins. They were all directly related to protein transporters, glycosyltransferases, membrane transport components, and cell wall structure. The integrity of cell membranes and walls is threatened in plants during cold as membrane fluidity decreases and dehydration increases (***Takahashi et al., 2020***). Therefore, physical changes such as remodelling of the lipidome of membranes (***Barrero-Sicilia et al., 2017***) are essential to survive cold (***Johnson, 2018***). For example, abundance changes of specific lipid species in other cereal models confer cold resistance (***Cheong et al., 2022***). Such membrane remodelling mechanisms in plants can rely on enzymatic activity to deliver new components needed to enhance cold acclimation (***Fourrier et al., 2008***). Many of the proteins that are transported to the cell periphery are initially synthesised near the ER - Golgi organelles, where the shuttles that transport them are ready to deliver them to their site of function. We have provided evidence that the transport machinery is active during cold, accumulating and being newly synthesised. This may be part of the plant's attempt to mitigate the loss of membrane integrity by transporting necessary membrane and wall components or the enzymes to produce them. Most importantly, translation of this sub-proteome demonstrates that cold-heterogeneous ribosomes are able to directly or indirectly control their translational output to efficiently acclimate.

Cold-heterogenous ribosomes also synthesise components of other macromolecular complexes without accumulating them. This type of synthesis implies potential remodelling of com-

plexes that continue to be present in equal amounts due to ongoing protein turnover. Complexes that fall into this category include the 60S ribosmal subunit, translation initiation, ER-Golgi, proteasome, vacuolar proton-transporting ATPase, and the oxoglutarate metabolon.

Conclusions

With careful consideration of the ^{15}N isotope flux and plant phenotype, we were able to monitor tracer incorporation into digested peptides of proteins at the complexome proteome level and compare between experimental conditions. Our strategy can be applied to any system that transitions between different biological steady states to study the dynamics of protein synthesis, as long as the right variables can be measured. We have made available our equations and complete bioinformatics method as a public R package, i.e., the ProtSynthesis R package. We applied this strategy to understand the transition of proliferative root tissue from germinating barley seedlings to a cold acclimated state. The proliferating root tissue of germinating barley seedlings undergoing cold acclimation, like Arabidopsis, requires ribosome biogenesis to overcome the initial stimulus. In addition, plants build remodelled and heterogeneous ribosomes that cause a shift in the proteome. To characterize the heterogeneity, we mapped the relative stoichiometry of ribosome-assembled rProteins and their synthesis rates using proteome-wide ^{15}N labelling to determine which part of the rProteome shift is due to synthesis and which part is due to reuse of pre-existing rProteins. We can currently conclude that plants significantly modulate the relative synthesis rates of ribosome-bound rProteins differentially when confronted with environmental factors, such as a shift to sub-optimal temperature, and that such modulation appears to be independent of *de novo* ribosome assembly. Moreover, ribosomes remodelled in the cold exhibit subtractive heterogeneity around the polypeptide exit tunnel (PET) and an accumulation of specific rProteins, in both 40S and 60S subunits, that are structurally linked to key intersubunit bridges. In addition, we examined general proteome shifts and found that 43S and 48S translation initiation complexes are preferentially synthesised and accumulate during cold, leading to a higher requirement for 60S subunits, which are at a constant ratio with 40S subunits but appear to be insufficient to form elongation-competent 80S monosomes and solve the over-accumulation of initiation complexes. We therefore hypothesize that 60S subunits are not able to bind all of the translation initiation complexes, and consequently they selectively associate with specific transcript-associated 48S complexes. This hypothesis is supported by the cold-induced heterogeneity, which mainly relates to the association of 40S and 60S subunits and as such could be a way to identify translational needs inherent to the cold context. The other major shift in the newly synthesised proteome is a response to protein aggregation and misfolding, which we propose is linked to missing rProteins around the PET in cold-remodelled ribosomes. This mechanism may be a second layer of translational control that allows ribosomes to misfold and target for degradation the part of the proteome that is currently not needed. From this study, we can currently conclude that there are major responses in the plant translational apparatus during cold that cause ribosomes to build a proteome to respond to the consequences of their own structural adaptations. Concomitantly the cold-heterogeneous ribosomes are able to directly or indirectly cause proteome shifts to remodel the cellular membrane and cell wall as part of the agenda to transition to an acclimated state and eventually resume growth.

Methods and Materials

Plant rearing

Surface Seed Sterilisation and Imbibition

Hordeum vulgare cultivar Keel seeds were obtained from The University of Melbourne from previous studies (***Gupta et al., 2019***). Seeds were placed inside sterile 50 mL falcon tubes (max 2 g per falcon tube approx. 40 seeds) amounting to a total of approx. 600 seeds (i.e., 15 falcon tubes). The non-biological materials were surface sterilised with 70 % ethanol and placed inside a clean bench, followed by UV-sterilisation. The seeds were soaked in 70 % ethanol and shaken gently for 1 min,

ethanol was then discarded. A 1 % bleach solution (0.042 % sodium hypochlorite) was then added to the falcon tube and gently shaken for 10 min, after which the bleach solution was discarded. The seeds were rinsed five times with sterile MilliQ H_2O and gently shaken for 5 min each time to completely remove the hypochlorite. The water was discarded. After straining the water, the seeds were soaked in sterile MilliQ H_2O and the falcon tubes were wrapped in aluminium foil to prevent any light exposure for 14 to 18 hours, half of which was at 25 °C and the other half at 18 °C, to mimic the daily temperature fluctuations and initiate imbibition of the seeds.

Seedling Germination and Treatment

Seeds were germinated and treated in complete perceived darkness by using a green light filter to cover the light entering the clean bench when the seeds were transferred to plates. For germination, seeds were transferred to 72 Petri dishes that were filled with 10 ml non-labelled, non-supplemented Scheible medium (***Scheible et al., 2004***) for 48 hours, 8 to 16 seeds were transferred into each petri dish. The dishes were sealed with micropore tape, wrapped in aluminium foil and placed in a phytotron growth chamber (Weiss Technik, Germany) with temperature settings of 25 °C for 16 h and 18 °C for 8 h until the completion of 48 h to allow germination. When 48 hours had passed, six germinated plants from a petri dish were harvested and processed to calculate RGR at time point zero (to be explained below). Then, working on the clean bench and under a green light filter, the medium in the dishes was disposed and exchanged for labelled and non-labelled supplemented media. 42 dishes with 10 mL non-labelled Scheible medium supplemented with 0.5 mM ^{14}N Serine and Glycine and 30 dishes with 10 mL labelled Scheible medium supplemented with 0.5 mM ^{15}N Serine (609005, Lot: MBBB0411V, Sigma Aldrich) and Glycine (299294, Lot: MBBC7772, CAS: 7299-33-4, Sigma Aldrich). Half of the labelled and non-labelled dishes were shifted to 4 °C to induce cold acclimation for 5 days. The other half remained in the control growth chamber with temperature fluctuation of 25 °C for 16 h and 18 °C for 8 h.

Plant Harvest and Phenotyping

For phenotyping, each individual plant was considered a biological replicate. In total 12 dishes were used, one per treatment, per time-point. Six cold-germinated and six control-germinated plants were harvested each day from day 0 until day 5. Immediately, the seedlings were scanned in order to determine the length, width, volume and area of the roots. Then, the roots of each plant were harvested separately and the excess media was completely removed with a paper towel. Samples were wrapped in a folded piece of Pergamin paper and immediately weighed for the fresh weight (FW), and then dried for 70 h at approx. 70 °C and weighed again for dry weight (DW). For all subsequent analysis, root tips were collected in 1.5 cm segments on the fifth day of acclimation. Labelled and non-labelled plants reared at cold and control temperatures were collected for primary metabolome and complexome / ribo-proteomic assays. Root segments of plants from the remaining 60 dishes were harvested by pooling root segments from 5 dishes per biological replicate (for a total of 3 biological replicates per labelling - temperature treatment combination). Briefly, 1.5 cm segments of the root tip were collected using a sharp blade and flash frozen with liquid nitrogen. Handling the plant material in frozen conditions, root pools were grinded in a pre-frozen mortar and pestle, followed by preparation of 200 mg and 60 mg aliquots for complexome / ribo-proteomic and primary metabolome analyses respectively. Ground plant material was stored at -80°C until further use.

Morphometric Image Processing

Images of the complete roots were acquired with an image analysis system and scanner (Perfection V800 Photo, Epson). Subsequently the software winRHIZO (Regent Instruments Inc., version released as 2019a) was used to delineate the root tissue and quantify the relevant morphological variables, root length, root average diameter, root volume, number of forks or bifurcations, number of tips, root length per volume. The software parameters were: ImgType - Grey, CalibMeth

- Intr, TPU Units - cm, PxSizeH - 0.006353, PxSizeV - 0.006347 [CalFile] - Scanner.Cal, PxClassif - GreyThdAutom-57, Filters - Smooth Off Area Off LWRatio Off, Fractal PxMin PxMax - Off.

Primary Metabolome Analysis

To extract metabolites, 360 µL of pre-cooled extraction mix containing Methanol:Chloroform:Water (2.5:1:1(v/v)) and 30 µL of U-^{13}C sorbitol (0.2 mg/mL), as internal standard, was added to 60 mg flash-frozen, grounded root tip tissue, vortexed vigorously and incubated at 70 °C for 15 min. Once the samples were cooled down to room temperature, 200 µL of $CHCl_3$ was added and incubated at 37 °C for 5 min with shaking. Phase separation was induced by adding 400 µL H_2O, vortexed and centrifuged at 20,800 rcf for 10 min. 160 µL aliquot from the upper polar phase was transferred to fresh 2 mL microvials and dried by vacuum centrifugation for 18 hours at room temperature. The dried samples were stored at -20°C until further use.

Primary metabolites were analysed by gas chromatography-mass spectrometry (GC-MS) of methoxyaminated and trimethylsilylated metabolite preparations (***Erban et al., 2020***). Metabolite extraction, chemical derivatization were as previously described. C_{10}, C_{12}, C_{15}, C_{18}, C_{19}, C_{22}, C_{28}, C_{32}, C_{36} n-alkane mixture was added to each sample for retention index calculation. Samples were processed using a Factor Four Capillary Column VF-5ms of dimensions 30 m length, 0.25 mm internal diameter and 0.25 mm film thickness (Variant Agilent) mounted to an Agilent 6890N gas chromatograph with split/splitless injector and electronic pressure control up to 150 psi (Agilent, Böblingen, Germany). Mass spectrometric data were acquired through a Pegasus III time-of-flight mass spectrometer (LECO Instrumente GmbH, Mönchengladbach, Germany), and in parallel using the same samples at high mass resolution using a micrOTOF-Q II hybrid quadrupole time-of-flight mass spectrometer (Bruker Daltonics, Bremen, Germany) with a multipurpose APCI source. Detailed GC-electron spray ionization TOF-MS settings were as reported previously (***Erban et al., 2020***).

Metabolites were annotated and identified by mass spectral and retention index matching to data of authenticated reference compounds from the Golm Metabolome Database (***Kopka et al., 2005***).

Ribosome Enriched Proteomics

Protease Considerations

Lys-C over Trypsin: Amino acids enriched in RNA protein-binding domains are histidine, arginine and lysine, which are all basic amino acids and. The rProteome is enriched in basic amino acids in order to be able to bind rRNA. Trypsin cleaves peptide sequences at the C-terminal of lysine and arginine residues, thus it would digest rProteins into smaller pieces as compare to Lys-C, which cleaves peptide sequences only at the C-terminal side of lysine residues. Thus Lys-C cuts sets of basic proteins such as the rProteins into significantly longer pieces as compared to trypsin (Figure 6 - Figure S1).

Ribosomal Protein Purification and Processing

Cell lysis was induced in grounded plant tissue using reported methods (***Firmino et al., 2020***; ***Martinez-Seidel et al., 2021c***) with minor modifications. Briefly, aliquots were placed in liquid nitrogen-cooled mortars and mass spectrometry friendly ribosome extraction buffer (MS_f-REB) was added at a buffer (V) to tissue (FW) ratio of two. The extract was then homogenised for 20 minutes while the mortars stayed on ice to prevent temperature from rising. Big particles were filtered through a pre-made, autoclaved and tip-amputated 5 mL pipette tip containing a ©Miracloth clog inside, and the filtrate was aliquoted in 2 mL microcentrifuge tubes. Samples were centrifuged at 14,000 x g for 20 min (4°C) to pellet insoluble cell debris and supernatants were transferred to violet QIAshredder mini spin columns (Qiagen, Australia) and centrifuged

again for one minute. Sample volume was adjusted to 4.5 ml in order to fill the ultracentrifuge tubes until 50 %. Subsequently, extracts were loaded carefully into thick-walled polycarbonate tubes with three-piece caps (10.4 mL, Polycarbonate Bottle with Cap Assembly, 16 x 76 mm - 6Pk, 355603, Beckman Coulter, USA) pre-filled with 2.5 mL sucrose cushion (SC) solution.

MS_f-REB: 0.2 M of Tris, pH 9.0, 0.2 M of KCl, 0.025 M of EGTA, pH 8.0, 0.035 M of $MgCl_2$, 1 % (W/V) octyl beta-D-glucopyranoside (98 %, O8001, Sigma Aldrich, Australia), 0.18 mM cycloheximide (Sigma Aldrich, Australia), 5 mM Dithiothreitol (R0861, Thermo Fisher, Australia), 1 mM Phenylmethylsulfonyl fluoride (36978, Thermo Fisher, Australia), 1X protease inhibitor cocktail (cat. No. P9599, Sigma Adrich, Australia).

SC: 0.4 M of Tris, pH 9.0, 0.2 M of KCl, 0.005 M of EGTA, pH 8.0, 0.035 M of $MgCl_2 \times 6H_2O$, and 60 % sucrose (Molecular Biology Grade, 573113, Sigma Aldrich, Australia), 0.18 mM cycloheximide (Sigma Aldrich, Australia), 5 mM Dithiothreitol (R0861, Thermo Fisher, Australia), 1 mM Phenylmethylsulfonyl fluoride (36978, Thermo Fisher, Australia), 1X protease inhibitor cocktail (cat. No. P9599, Sigma Adrich, Australia).

Loaded samples were centrifuged at 4°C, 330,000 x g / 60,000 RPM for 4.5 hours using a TY 70.1Ti rotor (Type 70.1 Ti Rotor, Beckman Coulter, USA) loaded into an Optima XE-100 Ultracentrifuge (Beckman Coulter, USA). After centrifugation, the supernatant was removed including the sucrose cushion taking care that the only solution in contact with the pellet was the SC. Tubes were completely dried by placing them upside down for a couple of minutes and dried pellets stored at -80°C until further usage. Ribosomal pellets were resuspended in 60 µL, freshly prepared, GuHCl to dissociate rProteins and TFA was added to 1 % final volume to induce precipitation of nucleic acids. The solution was then centrifuged in a microcentrifuge at 20,800 x g for 20 minutes and the supernatant recovered. Protein content was determined in samples using the bicinchoninic acid (BCA) kit (Thermo Scientific, United States) assay. As a control *Escherichia coli* ribosomes (P0763S, NEB, Australia) were used in 4 µL aliquots (approx. 2000 A260 units that are equivalent to 102 µg of ribosomes and 23 µg of rProtein) to undergo the full protocol (Figure 6 - Figure S2), confirming the integrity of ribosomal complexes when passing through the SCs solution and subsequent rProtein dissociation.

Protein amounts were standardised to the minimum concentration, i.e., 13.7 µg in 50 µL 6M GuHCl, 1 % TFA. Proteins were reduced and alkylated by adding tris(2-carboxyethyl)phosphine (TCEP) (77720, Thermo Scientific, United States) and iodoacetamide (IAA) (A3221, Sigma Aldrich, Australia) to 10 mM and 55 mM respectively, and shaking for 45 minutes at 37°C. The alkylation step was shaken in the dark. Acetonenitrile was then added to 70 % and a 10:1 ratio of magnetic beads (Hydrophilic- Part no: 45152105050250, GE Healthcare plus Hydrophobic- Part no: 65152105050250, GE Healthcare, Australia) were added and mixed with the solution. Beads were prepared according to the manufacturers instructions to a concentration of 20 μg/μL stock. Solution sat for 20 minutes with two pipette mixes, one every 10 minutes. Tubes were placed on a magnetic rack (DynaMag-2, 12321D, Life Technologies) and allowed to separate for 30 seconds. Washes were performed while the tubes remained in the rack. 1 ml of neat acetonitrile was added for 10 seconds and removed followed by 1 ml of 70 % ethanol for 10 seconds and removed. Tubes were removed from the rack and 1:10 protein (µg) to digestion buffer (µL) was immediately added. The digestion buffer (25mM triethylammonium bicarbonate (TEAB)) contained the Lys-C protease (P8109S, NEB, Australia) at a 1:20 protease to protein ratio. Samples were incubated for 18 hours at 37°C at 1000 RPM in a thermomixer (Eppendorf, Australia). TFA was added to 1 % to quench the reaction and then the tubes were put on the magnetic rack and the supernatant transferred to new tubes, twice. Finally a centrifugation step at 14,000 x g was performed to get rid of any residual beads and only 90 % of the supernatant was recovered. The recovered fraction was frozen for an

hour at -80°C and then freeze-dried. Peptides were resuspended in MS-loading buffer (2 % Acn + 0.05 % TFA) and loaded into a LC-MS/MS platform.

LC-MS/MS Analysis

All samples were analysed in the Nano-ESI-LC-MS/MS. The Nano-LC system, Ultimate 3000 RSLC (Thermofisher Scientific, San Jose, CA, USA) was set up with an Acclaim Pepmap RSLC analytical column (C18, 100 Å, 75 µm × 50 cm, Thermo Fisher Scientific, San Jose, CA, USA) and Acclaim Pepmap nano-trap column (75 µm × 2 cm, C18, 100 Å) and controlled at 50 °C. Solvent A was 0.1 % v/v formic acid and 5 % v/v dimethyl sulfoxide (DMSO) in water and solvent B was 0.1 % v/v formic acid and 5 % DMSO in ACN. The trap column was loaded with digested peptides at an isocratic flow 3 % ACN containing 0.05 % trifluoroacetic acid (TFA) at 6 µl/min for 6 min, followed by the switch of the trap column as parallel to the analytical column.

To measure peptides from barley experimental rProteome samples, the gradient settings for the LC runs, at a flow rate 300 nl/min, were as follows: solvent B 3 % to 23 % in 89 min, 23 % to 40 % in 10 min, 40 % to 80 % in 5 min, maintained at 80 % for 5 min before dropping to 3 % in 0.1 min and equilibration at 3 % solvent B for 9.9 min. An Exploris 480 Orbitrap mass spectrometer (Thermo Fisher Scientific, San Jose, CA, USA) with nano electrospray ionization (ESI) source at positive mode was employed to execute the MS experiments using settings of spray voltages, ion funnel RF, and capillary temperature level at 1.9 kV, 40 %, 275 °C, respectively. The mass spectrometry data was acquired with a 3-s cycle time for one full scan MS spectrum and as many data dependent higher-energy C-trap dissociation (HCD)-MS/MS spectra as possible. Full scan MS spectra feature ions at m/z of 300-1600, a maximum ion trapping time of 25 msec, an auto gain control target value of $3e^6$, and a resolution of 120,000 at m/z 200. An m/z isolation window of 1.2, an auto gain control target value of $7.5e^4$, a 30 % normalized collision energy, a first mass at m/z of 120, an automatic maximum ion trapping time, and a resolution of 15,000 at m/z 200 were used to perform data dependent HCD-MS/MS of precursor ions (charge states from 2 to 6).

To measure peptides from commercially available *Escherichia coli* ribosomes processed into rProteome samples gradient settings for the LC runs, at a flow rate 300 nl/min, were as follows: solvent B 3 % to 23 % in 59 min, 23 % to 40 % in 10 min, 40 % to 80 % in 5 min, maintained at 80 % for 5 min before dropping to 3 % in 0.1 min and equilibration at 3 % solvent B for 9.9 min. An Eclipse Orbitrap mass spectrometer (Thermo Fisher Scientific, San Jose, CA, USA) with nano electrospray ionization (ESI) source at positive mode was employed to execute the MS experiments using settings of spray voltages, ion funnel RF, and capillary temperature level at 1.9 kV, 30 %, 275 °C, respectively. The mass spectrometry data was acquired with a 3-s cycle time for one full scan MS spectra and as many data dependent higher-energy C-trap dissociation (HCD)-MS/MS spectra as possible. Full scan MS spectra features ions at m/z of 375-1500, a maximum ion trapping time of 50 msec, an auto gain control target value of $4e^5$, and a resolution of 120,000 at m/z 200. An m/z isolation window of 1.6, an auto gain control target value of $5e^4$, a 30 % normalized collision energy, a maximum ion trapping time of 22 msec, and a resolution of 15,000 at m/z 200 were used to perform data dependent HCD-MS/MS of precursor ions (charge states from 2 to 6).

Complete dataset proteomics submissions have been deposited to the ProteomeXchange Consortium (***Deutsch et al., 2020***) via the PRIDE (***Perez-Riverol et al., 2019***) partner repository with the dataset identifiers PXD032923 for *H. vulgare* experimental samples (**DOI**: 10.6019/PXD032923) and PXD032938 for *E.coli* control samples (**DOI**: 10.6019/PXD032938).

Data Analyses

Phenotyping

Relative growth rates using fresh, dry weight and varied phenotype measurements were calculated using R programming language with equation 1. The output units were mg * (mg^{-1} * h^{-1}). W is total weight accumulation at t_f and it is used in equation 1 to transform the growth rates into fractional of the final weight. Delta W or *dW* is the change in fresh or dry weight accumulation in milligrams from time 0 or non-germinated until delta t or *dt*, which represents hours after germination. Thus assuming an initial root weight of 0 leads to dW_t being represented by the weight measurement at time-point t. The Tukey-HSD test was performed after an ANOVA with a confidence level of 95 %.

Primary Metabolome

Amino acid abundances were analytically derived from GC-EI-ToF-MS acquired data using the software TagFinder (***Luedemann et al., 2008***) and the Golm Metabolome Database (***Kopka et al., 2005***). Extraction, standardisation, derivatization and GC-MS analytics were performed according to Erban et al., 2020 (***Erban et al., 2020***). Three biological replicates were measured in technical triplicates. For high abundant metabolites reaching the detection limit measurements of all samples were repeated with a 1:30 dilution (split) of extracts. Compounds were manually annotated in TagFinder and representative Tags for each metabolite chosen. Metabolome data were normalized to the levels of an internal $^{13}C_6$ sorbitol standard (CAS 121067-66-1), the background levels of the blanks were subtracted and data were normalized to the fresh weight of plant material in each sample. For Table S2, primary metabolome data were analysed with the "OmicsUnivariateStats.R" function of the RandoDiStats R package. Here, missing values were replaced by a small normally distributed numeric vector. Additionally, the fold change of metabolite abundances under cold conditions as well as the logical induction of metabolites (absence-presence-scenarios) were calculated.

^{15}N enrichment percentages of labelled metabolite pools was analytically derived from a multiplexed GC-EI-ToF-MS and GC-APCI-qToF-MS platform. In the first case, the workflow entailed baseline correction of the raw chromatogram files using the vendor software and transformation into CDF files. Pre-processing of the chromatograms for increasing data matrices quality (internal standard normalization and chromatogram alignment, mass scan width synchronisation) using TagFinder. Similarly, in the latter case, the vendor software was used to find the amino acid peaks in the chromatograms. peaks were manually mined and integrated in order to derive relative abundances. Every step of the targeted manual annotation of N containing mass tags is deposited in Table S3. Since ^{15}N feeding can cause differential abundances in monoisotopic fragments from the same amino acid analyte depending on the lack or presence of a N atom, multiple fragments per analyte and multiple isotopologs per fragment were considered. Thus, in order to account for the stable isotope variation, the correlation between fragment abundances was modified from a classical correlation among monoisotopic abundances to a correlation of the sum from all measured isotopologs for each fragment pair. Finally, for each amino acid analyte, three or more fragments were considered to provide a well-rounded annotation. From the final list of fragments, the most abundant ones (i.e., in the linear range of MS detection) were selected in order to calculate the percentage of ^{15}N enrichment. Only fragments with null enrichment in the control were let to pass to the next stage. When all fragments presented residual "enrichment" in non-labelled samples this way considered a technical bias, and as such the mean "enrichment" in non-labelled samples was subtracted from the labelled samples and those fragments in which the final variance in control "enrichment" was minimal were further used. Finally, when multiple fragments satisfied the criteria to be useful as a proxy for amino acid synthesis, the most accurate were defined to be those fragments with the lowest relative standard deviation across technical triplicates and biological replicates (File S1). Subsequently, using the molecular formula information per fragment, NIA corrections and % of enrichment calculations (***Heinrich et al., 2018***) were performed, followed by

a statistical comparison using the RandoDiStats R package (Tukey-HSD test was performed after an ANOVA with a confidence level of 95 %).

Plant Protein Synthesis Rates (K_s)

Two main approaches were used to derive our own calculations of protein synthesis rates, which are both detailed below. In Ishihara et al., protein synthesis rates are calculated using the amino acid alanine and its enrichment percentage in proteinogenic (ALA_p) and soluble (ALA_s) pools as a proxy for label incorporation into protein (K_s, equation 3a). The experimental time from the beginning of the experiment (t_0) until the end (t_f) is used to transform the nominal values into rates, which are expressed in percentage (%) per hour after a multiplication by 100.

$$K_s = \frac{(ALA_p[t_f]) - (ALA_p[t_0])}{ALA_s(t_f - t_0)} * \frac{100}{(t_f - t_0)} \tag{3a}$$

Protein degradation rates are then derived from K_s minus the product between plant relative growth rates (RGR) times the fractional change in protein content (P_p), accounting for differential growth (K_d, equation 3b).

$$K_d = (K_s - RGR * P_p) * 100 \tag{3b}$$

In Li et al., protein degradation rates are defined as the product of fold change in protein (FCP, equation 4c), natural logarithm normalized, by the non-labelled peptide fraction (1 - LPF) (K_d, equation 4a). LPF corresponds to the integer of the area under the curve observed in isotopolog envelope shifts caused by tracer incorporation for specific peptides. The calculations are performed using an in-house script written in Mathematica and the percentages differ from the peptide enrichment values.

$$K_d = \frac{LnFCP * (1 - LPF)}{T} \tag{4a}$$

Protein synthesis rates are then derived as a product of FCP, weighed by the K_d and experimental time (T, 4d), times the K_d rate (K_s, equation 4b).

$$\frac{K_s}{A} = \frac{FCP - e^{-K_d * T}}{1 - e^{-K_d * T}} * K_d \tag{4b}$$

FCP is calculated as the ratio between the products of fresh weight (FW) times total final (P_{pf}), in the numerator, and total initial (P_{p0}) protein content in the denominator (FCP, equation 4c).

$$FCP = \frac{FW * P_{pf}}{FW * P_{p0}} \tag{4c}$$

Time (T, equation 4d) equals to the difference between the intial experimental time (t_0) and the final experimental time (t_f).

$$T = t_f - t_0 \tag{4d}$$

Measurement Units of Protein Synthesis Rates (K_s)

Our K_s units imply percentage (%) of normalised labelled peptide fraction accumulated per unit of weight per hour (equation 5a).

$$K_s(units) = \frac{\%NormLPF_{pf}}{mg_{DW} * h} \tag{5a}$$

The product of the protein fraction (P_f) times the labelled peptide fraction equals a normalised version of the labelled peptide fraction ($NormLPF_{pf}$, equation 5b) that is turned into percentage fraction when multiplied by 100.

$$\%NormLPF_{pf} = P_f * LPF * \% \tag{5b}$$

This operation intends to normalise the enrichment in single peptides by the fraction of accumulated total protein, preventing biases derived from differential protein accumulation. Ultimately, the $NormLPF_{pf}$ units conserve the rate terms from the RGR formula, i.e., $NormLPF_{pf}$ accumulated per unit of weight per hour (equations 5a & 5c).

$$K_s(units) = LPF * \frac{P_f}{mg_{DW} * h} * \% \tag{5c}$$

Ribosome Enriched Proteome

RAW chromatograms, including labelled and non-labelled samples, were processed with MaxQuant, version 1.6.10.43 (***Cox and Mann, 2008***). Search parameters included fixed—carbamidomethyl (C) and variable—oxidation (M), acetyl (protein N-term) modifications. Everything else was set as default. Subsequently all .RAW files were converted into .mzML using the MSConverterGUI from the ProteoWizard toolbox. The threshold peak filter was set to "absolute intensity", ensuring the retention of all the peaks with an intensity greater than 100. This step allowed retaining in the files all the low abundant isotopes to conserve the isotopic envelopes of single peptides. Subsequently, using a python script, "isotopeEnrichment.py", developed in-house (isotopeEnrichment), the abundances of individual isotopolog peaks for peptide signals were mined out of the .mzML files (Table S4 - D tab). Briefly, the sequence, mass, charge and retention times for peptides derived from proteins were taken from MaxQuant search results (i.e., the "evidence" MaxQuant output file). For each peptide localised at a single point in the chromatograms, theoretical exact masses were then used to create an extracted ion chromatogram (EIC) that is a summation of the intensities of each of the target isotopolog peaks. A Gaussian curve was then fitted to the EIC and the target isotopolog intensities were taken as the average of the observed intensities in a given number of mass spectra at either side of the Gaussian peak maxima. The procedure avoids skewing subsequent calculations to single scan isotopic ratios and thus ensures that the measured isotopolog abundances and relative ratios across the peptide peak are conserved with high fidelity. The script is written for python 3.7 and uses PymzML (***Bald et al., 2012***) and Pyteomics (***Levitsky et al., 2019***) to read mass spectrometry data files and calculate peptide masses respectively. The exemplary code used to produce our results was:

```
//Python-3.6.5

##  loading the correct module and specification of the correct python version (when working
     with a modular server system):

module add devel/Python-3.6.5

## Returning peptides with potentially labelled amino acid resiudes during cold:

python3 isotopeEnrichment.py --evidenceFile evidence.txt --mzmlFileDir . --specialResidue S
     --specialResidue G --addSpecialResidues --outDir results_cold

## Returning peptides with potentially labelled amino acid resiudes at optimized temperature:

python3 isotopeEnrichment.py --evidenceFile evidence.txt --mzmlFileDir . --specialResidue S
     --specialResidue G --addSpecialResidues --outDir results_control
```

The mined isotopolog peaks for individual peptide species were then used to construct the necessary files for enrichment calculation (Table S4 - E tabs). Natural isotopic abundance (NIA) was calculated and abundances corrected using the R package IsoCorrectoR (***Heinrich et al., 2018***). The package requires first a “molecule” file that features the molecular formulas of the masses to be corrected. Secondly, an “intensities” file, containing the measured mass features and their isotopologs. Finally, an “elemental” file, containing the chemical elements with their NIA. Input files have been compiled in Table S4 - E tabs. An R function, "isotopeEnrichment.R", was built to take up the abundances mined by "isotopeEnrichment.py" and turn them into the necessary format of IsoCorrectoR. Subsequently, the .csv files containing the enrichment percentages were used as input for the R function "EnrichmentSet.R", which generates subsets of significantly labelled peptides using dependencies to the RandoDiStats R package. Additionally the function outputs the subset of unlabelled peptides as a control to monitor in the annotated proteins. The next function is named "AnnotateProteins.R", which takes the outputs from "EnrichmentSet.R" in order to build protein enrichment percentages that are calculated based on the average enrichment of their monitored peptides. The function outputs protein sequences with the highlighted monitored peptides, the mean non-corrected protein enrichment percentage (non-corrected LPF, Table S4 - E4 tab) and standard deviations as a measure of reliability from the obtained averages. Finally, "LPFcorrect.R" corrects the outputs using the enrichment percentage in soluble amino acids and protein enrichments are transformed into fractional synthesis rates using equation 2a, all these calculations have been implemented into R functions and can be used from the ProtSynthesis R package. The workflow can be used averaging peptides from the same protein into a single entry or conserving peptides individually.

Acknowledgments

We thank the Mass Spectrometry and Proteomics Facility of The Bio21 Molecular Science and Biotechnology Institute at The University of Melbourne for the support of mass spectrometry analysis. We thank Dr. Sneha Gupta for providing the seed material used in this work.

Figures and Tables

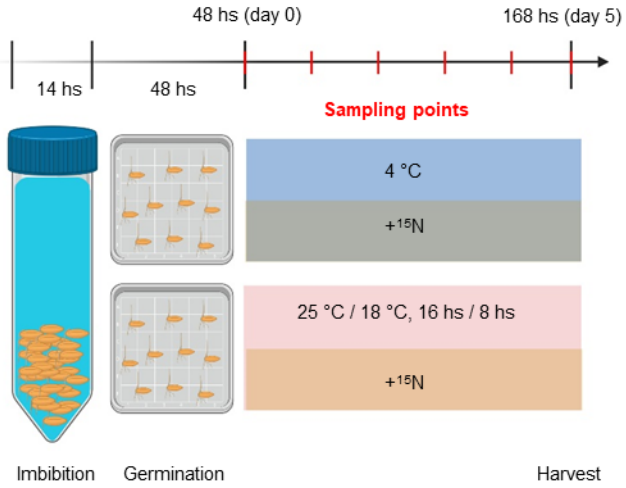

Figure 1–Figure supplement 1. Root phenotype during germination assay in optimal control and suboptimal cold temperatures.

Figure 1–Figure supplement 2. Summary of the methodological workflow to achieve measurements of protein synthesis and abundance in barley root tips.

Figure 1. Experimental setup. *Hordeum vulgare* seeds were soaked in sterile H_2O for 14 h imbibition. Seeds were transferred to plates for germination for 48 h. At 48 h treatments were applied and it was considered as experimental day 0. Half of remaining seedlings were treated with media supplemented with ^{15}N compounds and the other half continued on media supplemented with ^{14}N compounds as a control. Half of the seeds in treatment and in control plates were shifted to 4 °C to induce cold acclimation. The other half remained in the control growth chamber with a temperature fluctuation of 25 °C for 16 h and 18 °C for 8 h. Six seedlings were harvested daily per treatment after day 0 for phenotypic analyses. After harvest, each seedling was scanned for phenotyping, roots were weighed for fresh weight and dried for 70 h at 70 °C and weighed again for dry weight. For primary metabolome analysis, root tips were collected in 1.5-cm segments on the fifth day of acclimation. Created with BioRender.com

Table 1. Relative growth rates calculated from multiple root growth proxies from germinating barley seedlings

Relative Growth Rates (RGR)	Control	Cold
Fresh Weight (*mg/mg.FW*hs*)	0.008	0.011
Dry Weight (*mg/mg.DW*hs*)	0.008	0.017
Length Per Volume ($cm*m^3/cm*m^3*hs$)	0.008	0.01
Length (*cm/cm*hs*)	0.008	0.01
Volume (cm^3/cm^3*hs)	0.008	0.008
Average Diameter (*mm/mm*hs*)	0.014	0.014
Number of Forks (*#/#*hr*)	0.012	0.007
Number of Tips (*#/#*hr*)	0.007	0.007

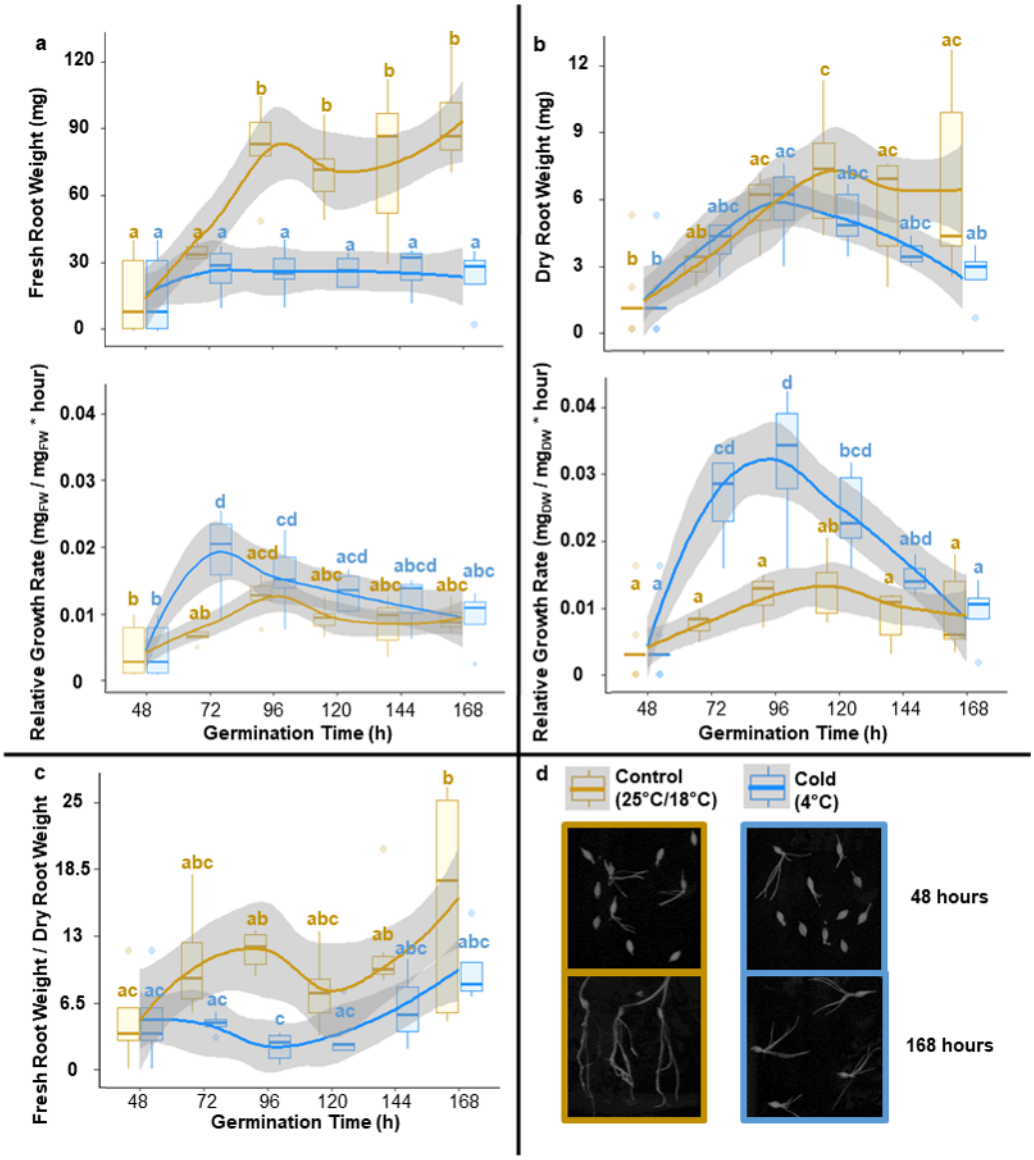

Figure 2–Figure supplement 1. Summary of 95% confidence level Tukey-HSD statistical differences in mean levels of growth related variables across treated and control barley seedlings.

Figure 2–Figure supplement 2. Statistical differences in mean levels (95% confidence level Tukey-HSD) of growth related variables derived from scanning treated (blue) and control (gold) barley seedlings at each time-point.

Figure 2–Figure supplement 3. Linear regression after natural logarithm transformation of growth related variables.

Figure 2. Root growth dynamics of barley seedlings reared at optimal and cold suboptimal temperatures. Barley seeds were imbibed and germinated for 48 hours at optimal rearing conditions and then were transferred to different temperature regimes for five days. Panels A, B, & C contain measurements of specific growth related variables measured in roots, outlined as plots where means are solid coloured lines (blue for cold and gold for control) and standard deviations are shades around the mean. All mean values were compared using an ANOVA followed by the posthoc Tukey HSD test. The boxplots are labelled according to significant differences in the Tukey HSD test, where shared letters indicate lack of significance. Starting at 48 hours after imbibition, seedlings were scanned every 24 hours to measure root growth with a subsequent destructive harvesting to measure root fresh weight (A - upper panel). Subsequently root systems were dried for 3 days at 70°C and weighed again to measure root dry weight (B - upper panel). The recorded weights were used to asses the statistical changes in the fresh to dry weight ratio during the experimental period (C). Finally, both weights were used to calculate RGRs (A & B - lower panels) based on root weight at the imbibition stage (i.e., 0 hours) being zero grams. RGR would subsequently serve the purpose of normalizing protein synthesis rates to basal root growth, preventing biomass accumulation biases.

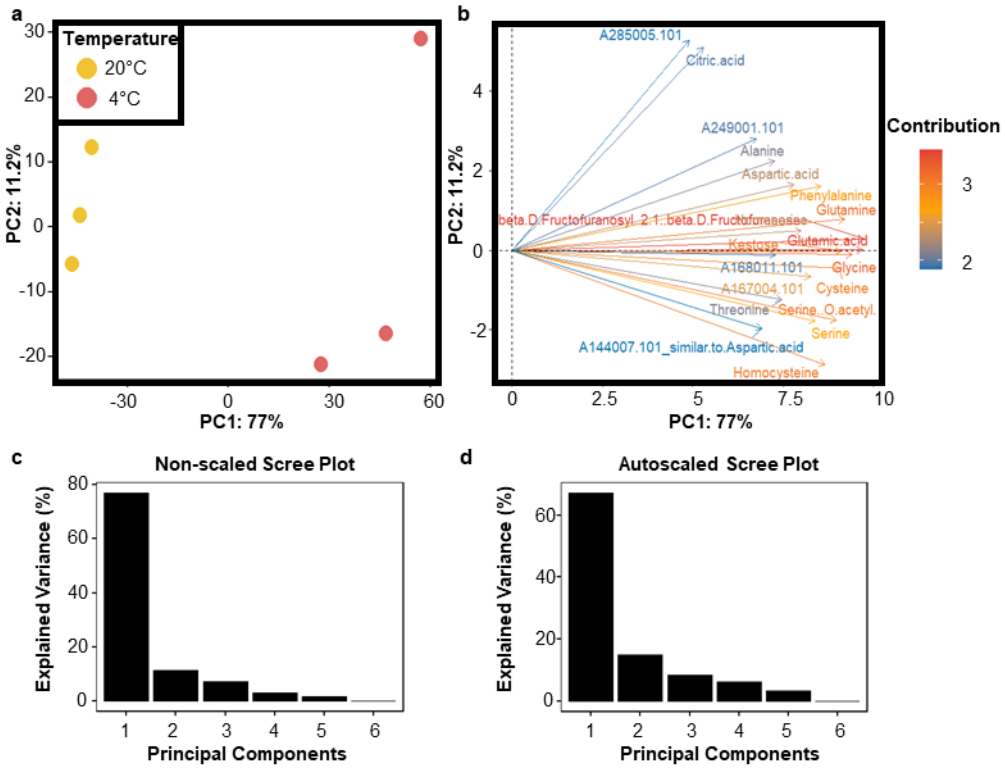

Figure 3. Primary metabolome dynamics of barley seedlings reared at optimal and cold suboptimal temperatures. Also relates to Table S2. The soluble primary metabolome was obtained from frozen and ground plant tissue by methanol / chlorophorm extraction, and the metabolite extracts were chemically derivatized using trimethylsilyl groups to enhance volatility across the gas chromatographic column. Subsequently, the metabolome was measured in a multiplexed array by GC-EI-ToF-MS and GC-APCI-qToF-MS (***Erban et al., 2020***) in technical triplicates. Metabolites were manually annotated in TagFinder and representative tags for each metabolite chosen. Primary metabolome data were analyzed with functions of the RandoDiStats R package. Panel A contains the principal component analyses (PCA) plot where experimental samples are variables and metabolites eigenvectors determining the separation of the samples. Panel B highlights the best 20 metabolite features contributing to the separation outlined in the samples by a contribution PCA plot. Panel C & D contain the scree plot of variance explained in each principal component (PC) in the non-scaled and autoscaled dataset respectively.

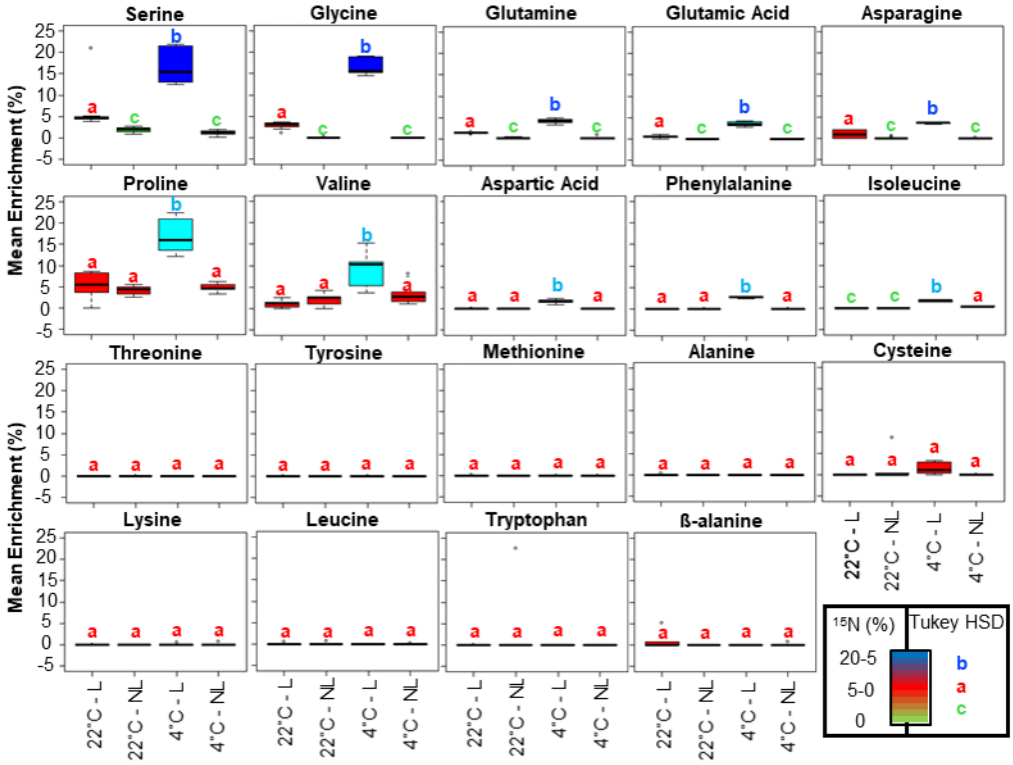

Figure 4. Mean isotopic enrichment of amino acid soluble pools in barley root tips from seedlings germinated at suboptimal (4°C) and optimal (20°C) temperatures. Also relates to Table S3 and File S1. The soluble primary metabolome was obtained exactly as described in Figure 3. Subsequently, at least three independent mass fragments per amino acid analyte along with their isotopolog peak intensities were extracted from total ion chromatograms. The selected fragments for ^{15}N enrichment percentage calculations were those that appeared in spectra containing less co-eluting ions as well as those with evidently increased mass accuracy (e.g., from the APCI platform) summing up to less noisy spectra. The fragments were corrected for natural isotopic abundance, enabling calculation of enrichment percentages using the R package IsoCorrectoR (***Heinrich et al., 2018***). Finally, mean enrichments were statistically compared across treatments using an ANOVA, followed by a posthoc Tukey HSD test. Boxplots are coloured according to mean significant differences, further emphasised by the letters above each box.

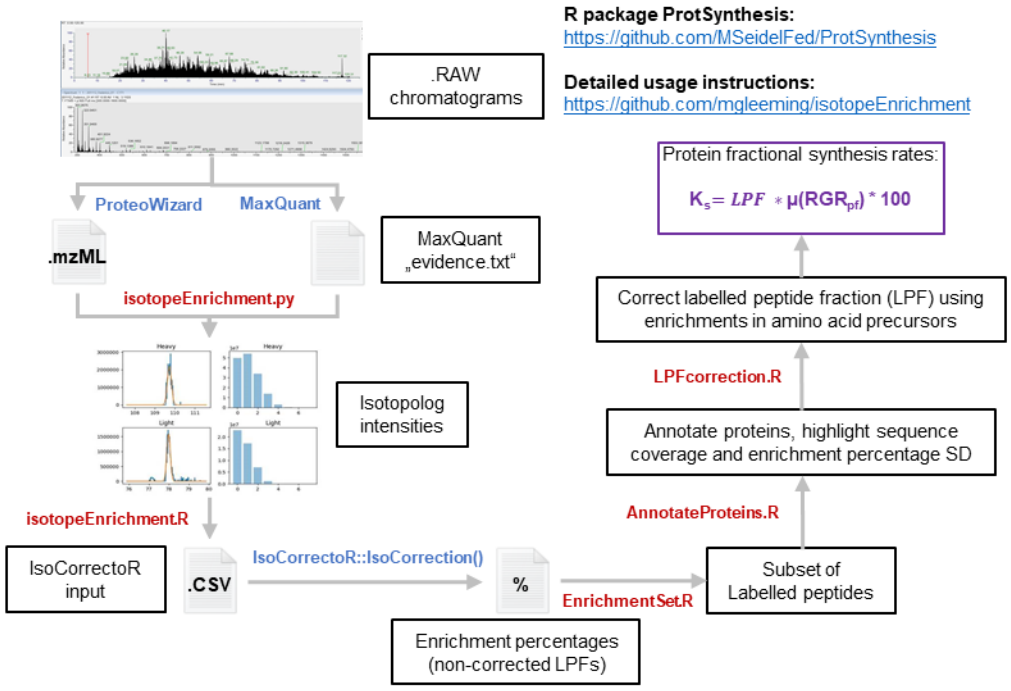

Figure 5–Figure supplement 1. Summary of 95% confidence level Tukey-HSD statistical differences in mean levels of protein content from proteome fractions enriched in ribosomes across treated and control barley seedlings.

Figure 5–Figure supplement 2. Subset of peptides considered as having optimal quality for interpretation of their relative fractional synthesis rates during the physiological transition of roots from germinating barley seedlings from optimal to suboptimal temperature.

Figure 5. Bioinformatics pipeline written as a python function and an R package that jointly enable to calculate stable isotope tracer incorporation into peptides from LC-MS/MS data and derive fractional protein synthesis rates in the organismal physiological context. Also relates to Table S4. The whole pipeline has been made publicly available in two repositories. The isotopeEnrichment GitHub repository, which contains detailed usage instruction of both python and R functions and the ProtSynthesis R package, which can be installed into any R environment via devtools. All the self-written steps in the pipeline are signalled by red font, while existing algorithms that are external dependencies are depicted in blue font. The pipeline entails using the MaxQuant software to locate proteins and peptides in the chromatograms and then trace back their position and recover their full isotopolog intensities from .mzML files using "isotopeEnrichment.py". Subsequently, an optimal number of isotopolog peaks are derived for individual peptides based on the molecular formula and the enrichment percentages in soluble amino acids using "isotopeEnrichment.R". The data delivered is organised as is required by the IsoCorrectoR R package, which is then used to correct for the natural isotopic abundance and calculate the enrichment percentage of individual peptides (LPF). Subsequently, statistical filters are used to identify and annotate significantly labelled proteins as well as to derive relevant statistics that detail the quality of the protein hit using "EnrichmentSet.R" and "AnnotateProteins.R" respectively. Finally, "LPFcorrection.R" is used to correct the calculated LPFs using the enrichment in soluble amino acid pools, with these corrected values fractional protein synthesis rates are calculated by multiplying them by relative growth rates times 100.

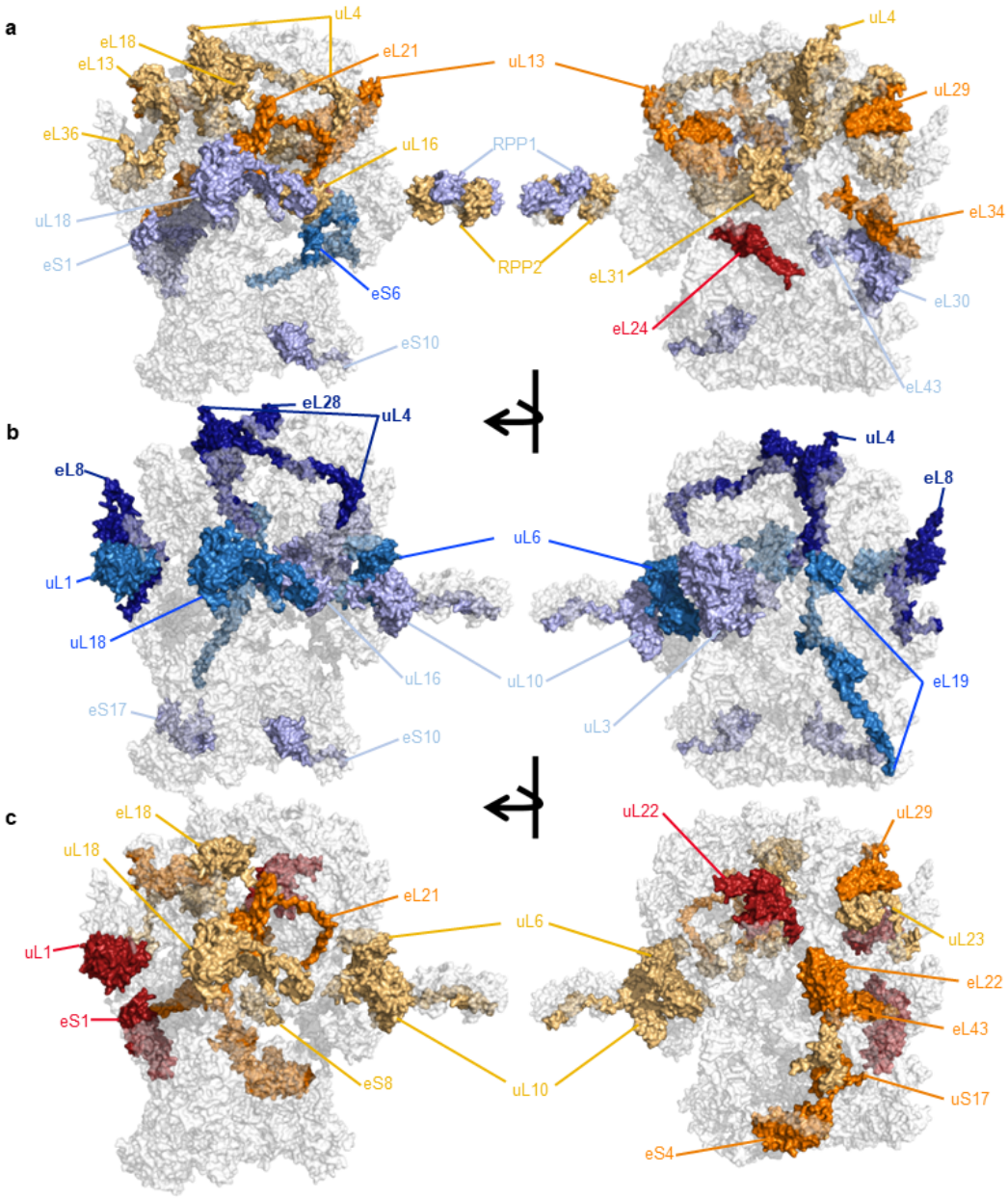

Figure 6–Figure supplement 1. Volcano plot outlining the differences in mean peptide length produced with Lys-C or Trypsin, during an *in silico* protease digestion test, as proteases to digest the Arabidopsis signature plant ribosomal proteome.

Figure 6–Figure supplement 2. Positive control and complete coverage of *escherichia coli* 70S ribosomal proteome from a commercially available preparation used to verify the ribosomal proteomics pipeline.

Figure 6–Figure supplement 3. Ratio between 40S SSU and 60S LSU abundances across experimental samples

Figure 6. Characterization of cold heterogeneous barley ribosomes, their ribosomal protein (rProtein) composition, fractional synthesis rates and induced substoichiometry. Barley ribosomes from plant ^{15}N labelled proliferative tissue were purified and used to profile the rProteome. Abundances and isotopolog envelopes were recovered from the Mass Spectrometry data and used to calculate average ribosome relative stoichiometry of rProteins and their fractional synthesis rates. (a) rProtein substoichiometry; orange and reds are rProteins accumulated at optimal temperature and blues rProteins accumulated during cold in the ribosomal population. (b) Preferential synthesis of assembled rProteins during cold acclimation. (c) Preferential synthesis of assembled rProteins during control temperature. Preferential synthesis refers to peptides with significant changes (P_{adj} values < 0.05, n = 3, tested using a customized generalized linear model) in their fractional synthesis rates.

Table 2. Accumulation and origin of protein components from detected multi-protein complexes in barley root tips classified in four groups of responses during the experimental period: (Group 1) accumulated and newly synthesised, (Group 2) accumulated and not degraded, (Group 3) not accumulated but newly synthesised, (Group 4) and not accumulated and not synthesised.

Parent Categories	Detected Complexes	Cold (4°C)	Control (22°C)
Cytosolic ribosome	cytosolic large ribosomal subunit (GO:0022625)	Group 3	Group 1
	cytosolic small ribosomal subunit (GO:0022627)	Group 4	Group 1
Mitochondrial ribosome	mitochondrial large ribosomal subunit (GO:0005762)	Group 4	Group 2
	mitochondrial small ribosomal subunit (GO:0005763)	Group 4	Group 2
Ribosome biogenesis complex	preribosome, small subunit precursor (GO:0030688)	Group 2 (GO:0030692)	Group 4
	preribosome, large subunit precursor (GO:0030687)	Group 2	Group 4
	small-subunit processome (GO:0032040)	Group 1	Group 4
	Pwp2p-containing subcomplex of 90S preribosome (GO:0034388)	Group 2	Group 4
Translation initiation complex	eukaryotic 48S preinitiation complex (GO:0033290)	Group 1	Group 4
	eukaryotic 43S preinitiation complex (GO:0016282)	Group 1	Group 4
	eukaryotic translation initiation factor 3 complex (GO:0005852)	Group 1	Group 4
	eukaryotic translation initiation factor 2B complex (GO:0005851)	Group 3	Group 4
	eukaryotic translation initiation factor 2 complex (GO:0005850)	Group 3	Group 4
Protein folding	chaperonin-containing T-complex (GO:0005832)	Group 1	Group 4
ER-Golgi complex	clathrin adaptor complex (GO:0030131)	Group 3	Group 4
	clathrin vesicle coat (GO:0030125)	Group 3	Group 4
	EMC complex (GO:0072546)	Group 1 (GO:0005789)	Group 4
	endoplasmic reticulum exit site (GO:0070971)	Group 1	Group 4
	COPII vesicle coat (GO:0030127)	Group 2	Group 4
	trans-Golgi network (GO:0005802)	Group 3	Group 4
	Golgi membrane (GO:0000139)	Group 1	Group 4
	Golgi transport complex (GO:0017119)	Group 3	Group 4
	COPI vesicle coat (GO:0030126)	Group 3	Group 4
	exocyst (GO:0000145)	Group 4	Group 4
	endoplasmic reticulum-Golgi intermediate compartment (GO:0005793)	Group 2 (GO:0098791)	Group 4
Stress related complexes	cytoplasmic stress granule (GO:0010494)	Group 4	Group 4
	P-body (GO:0000932)	Group 4	Group 4
Proteasome	proteasome core complex, alpha-subunit complex (GO:0019773)	Group 3	Group 4

	proteasome regulatory particle, lid subcomplex (GO:0008541)	Group 4	Group 4
	proteasome regulatory particle, base subcomplex (GO:0008540)	Group 3	Group 4
Oxidative complex	peroxisome (GO:0005777)	Group 4	Group 4
protein degradation complex	COP9 signalosome (GO:0008180)	Group 4	Group 4
Transcriptional regulation complex	THO complex part of transcription export complex (GO:0000445)	Group 2 (GO:0000347)	Group 4
	catalytic step 2 spliceosome (GO:0071013)	Group 2 (GO:0097525)	Group 4
Nuclear complex	DNA topoisomerase type II (double strand cut, ATP-hydrolyzing) complex (GO:0009330)	Group 2 (GO:0030870)	Group 4
	perinuclear region of cytoplasm (GO:0048471)	Group 1	Group 4
	nuclear periphery (GO:0034399)	Group 2 (GO:0070603)	Group 4
	nuclear pore (GO:0005643)	Group 2 (GO:0031080)	Group 4
Cell cycle related complexes	condensin complex (GO:0000796)	Group 1	Group 4
	MCM complex (GO:0042555)	Group 2	Group 4
	alpha DNA polymerase:primase complex (GO:0005658)	Group 2	Group 4
	DNA replication factor C complex (GO:0005663)	Group 2	Group 4
Cell wall and membrane complex	oligosaccharyltransferase complex (GO:0008250)	Group 4	Group 4
	endosome membrane (GO:0010008)	Group 3	Group 4
	cellulose synthase complex (GO:0010330)	Group 4	Group 4
	endocytic vesicle (GO:0030139)	Group 4	Group 4
	cell wall (GO:0005618)	Group 4	Group 4
	plasma membrane protein complex (GO:0098797)	Group 4	Group 4
Vacuolar complex	plant-type vacuole (GO:0000325)	Group 4	Group 4
	vacuolar proton-transporting V-type ATPase complex (GO:0016471)	Group 3	Group 4
	proton-transporting V-type ATPase, V1 domain (GO:0033180)	Group 3	Group 4
Metabolon	oxoglutarate dehydrogenase complex (GO:0045252)	Group 3	Group 2 (GO:0045254)
Motor related complex	myosin complex (GO:0016459)	Group 2	Group 4
Transmembrane complex	transmembrane transporter complex (GO:1902495)	Group 4	Group 4
Cytoskeleton complex	microtubule (GO:0005874)	Group 1	Group 4
Mitochondrial complex	mitochondrial outer membrane (GO:0005741)	Group 1	Group 4

	mitochondrial inner membrane (GO:0005743)	Group 4	Group 4
Chloroplast complex	chloroplast membrane (GO:0031969)	Group 4	Group 4

- **Note**: the table integrates the information from A1 and G1 tabs in Table S4. GO terms have been defined in parenthesis at first appearance. When cellular complex subsets and not the whole monitored complex belongs to one of the response groups, the GO terms are indicated in parenthesis.

References

Appels R, Wang P, Islam S. Integrating wheat nucleolus structure and function: variation in the wheat ribosomal RNA and protein genes. Frontiers in plant science. 2021; 12:686586. doi: 10.3389/fpls.2021.686586.

Ashraf MA, Rahman A. Cold stress response in Arabidopsis thaliana is mediated by GNOM ARF-GEF. Plant Journal. 2019; 97(3):500–516. doi: 10.1111/tpj.14137.

Aylett CH, Boehringer D, Erzberger JP, Schaefer T, Ban N. Structure of a Yeast 40S–eIF1–eIF1A–eIF3–eIF3j initiation complex. Nature structural & molecular biology. 2015; 22(3):269–271. doi: 10.1038/nsmb.2963.

Bald T, Barth J, Niehues A, Specht M, Hippler M, Fufezan C. PymzML-Python module for high-throughput bioinformatics on mass spectrometry data. Bioinformatics. 2012; 28(7). doi: 10.1093/bioinformatics/bts066.

Barakat A, Szick-Miranda K, Chang IF, Guyot R, Blanc G, Cooke R, Delseny M, Bailey-Serres J. The organization of cytoplasmic ribosomal protein genes in the Arabidopsis genome. Plant physiology. 2001; 127(2):398–415. doi: 10.1104/pp.010265.

Barandun J, Chaker-Margot M, Hunziker M, Molloy KR, Chait BT, Klinge S. The complete structure of the small-subunit processome. Nature structural & molecular biology. 2017; 24(11):944–953. doi: 10.1038/nsmb.3472.

Barrero-Sicilia C, Silvestre S, Haslam RP, Michaelson LV. Lipid remodelling: Unravelling the response to cold stress in Arabidopsis and its extremophile relative Eutrema salsugineum. Plant Science. 2017; 263:194–200. doi: 10.1016/j.plantsci.2017.07.017.

Beine Golovchuk O, Firmino AAP, Dąbrowska A, Schmidt S, Erban A, Walther D, Zuther E, Hincha DK, Kopka J. Plant temperature acclimation and growth rely on cytosolic ribosome biogenesis factor homologs. Plant Physiology. 2018; 176(3):2251–2276. doi: 10.1104/pp.17.01448.

Berková V, Kameniarová M, Ondrisková V, Berka M, Menšíková S, Kopecká R, Luklová M, Novák J, Spíchal L, Rashotte AM, et al. Arabidopsis response to inhibitor of cytokinin degradation INCYDE: Modulations of cytokinin signaling and plant proteome. Plants. 2020; 9(11):1563. doi: 10.3390/plants9111563.

Bowman JC, Petrov AS, Frenkel-Pinter M, Penev PI, Williams LD. Root of the tree: the significance, evolution, and origins of the ribosome. Chemical reviews. 2020; 120(11):4848–4878. doi: 10.1021/acs.chemrev.9b00742.

Briggs JW, Dinman JD. Subtractional heterogeneity: a crucial step toward defining specialized ribosomes. Molecular cell. 2017; 67(1):3–4. doi: 10.1016/j.molcel.2017.06.022.

Brito Querido J, Sokabe M, Kraatz S, Gordiyenko Y, Skehel JM, Fraser CS, Ramakrishnan V. Structure of a human 48 S translational initiation complex. Science. 2020; 369(6508):1220–1227. doi: 10.1126/science.aba4904.

Castellano MM, Merchante C. Peculiarities of the regulation of translation initiation in plants. Current Opinion in Plant Biology. 2021; 63:102073. doi: 10.1016/j.pbi.2021.102073.

Cheong BE, Beine-Golovchuk O, Gorka M, Ho WWH, Martinez-Seidel F, Firmino AAP, Skirycz A, Roessner U, Kopka J. Arabidopsis REI-LIKE proteins activate ribosome biogenesis during cold acclimation. Scientific Reports. 2021; 11(1):1–25. doi: 10.1038/s41598-021-81610-z.

Cheong BE, Yu D, Martinez-Seidel F, Ho WWH, Rupasinghe TW, Dolferus R, Roessner U. The Effect of Cold Stress on the Root-Specific Lipidome of Two Wheat Varieties with Contrasting Cold Tolerance. Plants. 2022; 11(10):1364. doi: 10.3390/plants11101364.

Chiu WL, Wagner S, Herrmannova A, Burela L, Zhang F, Saini AK, Valasek L, Hinnebusch AG. The C-terminal region of eukaryotic translation initiation factor 3a (eIF3a) promotes mRNA recruitment, scanning, and, together with eIF3j and the eIF3b RNA recognition motif, selection of AUG start codons. Molecular and cellular biology. 2010; 30(18):4415–4434. doi: 10.1128/MCB.00280-10.

Clowes FAL. Protein synthesis in root meristems. Journal of Experimental Botany. 1958; 9(2):229–238. doi: 10.1093/jxb/9.2.229.

Cox J, Mann M. MaxQuant enables high peptide identification rates, individualized p.p.b.-range mass accuracies and proteome-wide protein quantification. Nature Biotechnology. 2008; 26(12):1367–1372. doi: 10.1038/nbt.1511.

Dal Degan F, Rocher A, Cameron-Mills V, Von Wettstein D. The expression of serine carboxypeptidases during maturation and germination of the barley grain. Proceedings of the National Academy of Sciences of the United States of America. 1994; 91(17):8209–8213. doi: 10.1073/pnas.91.17.8209.

Des Georges A, Dhote V, Kuhn L, Hellen CU, Pestova TV, Frank J, Hashem Y. Structure of mammalian eIF3 in the context of the 43S preinitiation complex. Nature. 2015; 525(7570):491–495. doi: 10.1038/nature14891.

Deutsch EW, Bandeira N, Sharma V, Perez-Riverol Y, Carver JJ, Kundu DJ, García-Seisdedos D, Jarnuczak AF, Hewapathirana S, Pullman BS, Wertz J, Sun Z, Kawano S, Okuda S, Watanabe Y, Hermjakob H, Maclean B, Maccoss MJ, Zhu Y, Ishihama Y, et al. The ProteomeXchange consortium in 2020: Enabling 'big data' approaches in proteomics. Nucleic Acids Research. 2020; 48(D1):D1145–D1152. doi: 10.1093/nar/gkz984.

Dinneny JR, Benfey PN. Plant Stem Cell Niches: Standing the Test of Time. Cell. 2008; 132(4):553–557. doi: 10.1016/j.cell.2008.02.001.

Dong Z, Liu LH, Han B, Pincheira R, Zhang JT. Role of eIF3 p170 in controlling synthesis of ribonucleotide reductase M2 and cell growth. Oncogene. 2004; 23(21):3790–3801. doi: 10.1038/sj.onc.1207465.

Erban A, Martinez-Seidel F, Rajarathinam Y, Dethloff F, Orf I, Fehrle I, Alpers J, Beine-Golovchuk O, Kopka J. Multiplexed Profiling and Data Processing Methods to Identify Temperature-Regulated Primary Metabolites Using Gas Chromatography Coupled to Mass Spectrometry. In: Hincha DK, Zuther E, editors. *Methods in Molecular Biology*, vol. 2156 New York, NY: Springer US; 2020.p. 203–239. https://doi.org/10.1007/978-1-0716-0660-5_15, doi: 10.1007/978-1-0716-0660-5_15.

Firmino AAP, Gorka M, Graf A, Skirycz A, Martinez-Seidel F, Zander K, Kopka J, Beine-Golovchuk O. Separation and paired proteome profiling of plant chloroplast and cytoplasmic ribosomes. Plants. 2020; 9(7):1–29. doi: 10.3390/plants9070892.

Fourrier N, Bédard J, Lopez-Juez E, Barbrook A, Bowyer J, Jarvis P, Warren G, Thorlby G. A role for sensitive to freezing2 in protecting chloroplasts against freeze-induced damage in Arabidopsis. The Plant Journal. 2008; 55(5):734–745. doi: 10.1111/j.1365-313X.2008.03549.x.

Fowler S, Thomashow MF. Arabidopsis transcriptome profiling indicates that multiple regulatory pathways are activated during cold acclimation in addition to the CBF cold response pathway. The Plant Cell. 2002; 14(8):1675–1690. doi: 10.1105/tpc.003483.

Fringer JM, Acker MG, Fekete CA, Lorsch JR, Dever TE. Coupled release of eukaryotic translation initiation factors 5B and 1A from 80S ribosomes following subunit joining. Molecular and cellular biology. 2007; 27(6):2384–2397. doi: 10.1128/MCB.02254-06.

Fusco CM, Desch K, Dörrbaum AR, Wang M, Staab A, Chan IC, Vail E, Villeri V, Langer JD, Schuman EM. Neuronal ribosomes exhibit dynamic and context-dependent exchange of ribosomal proteins. Nature communications. 2021; 12(1):1–14. doi: 10.1038/s41467-021-26365-x.

Gamalinda M, Woolford JL. Deletion of L4 domains reveals insights into the importance of ribosomal protein extensions in eukaryotic ribosome assembly. Rna. 2014; 20(11):1725–1731. doi: 10.1261/rna.046649.114.

Garcia-Molina A, Kleine T, Schneider K, Mühlhaus T, Lehmann M, Leister D. Translational Components Contribute to Acclimation Responses to High Light, Heat, and Cold in Arabidopsis. iScience. 2020; 23(7):101331. doi: 10.1016/j.isci.2020.101331.

Genuth NR, Barna M. Heterogeneity and specialized functions of translation machinery: From genes to organisms. Nature Reviews Genetics. 2018; 19(7):431–452. doi: 10.1038/s41576-018-0008-z.

Gomes-Duarte A, Lacerda R, Menezes J, Romão L. eIF3: a factor for human health and disease. RNA biology. 2018; 15(1):26–34. doi: 10.1080/15476286.2017.1391437.

Gomez MAR, Ibba M. Aminoacyl-tRNA synthetases. Rna. 2020; 26(8):910–936. doi: 10.1261/rna.071720.119.

Greber BJ, Gerhardy S, Leitner A, Leibundgut M, Salem M, Boehringer D, Leulliot N, Aebersold R, Panse VG, Ban N. Insertion of the biogenesis factor Rei1 probes the ribosomal tunnel during 60S maturation. Cell. 2016; 164(1-2):91–102. doi: 10.1016/j.cell.2015.11.027.

Gupta S, Rupasinghe T, Callahan DL, Natera SHA, Smith PMC, Hill CB, Roessner U, Boughton BA. Spatio-Temporal Metabolite and Elemental Profiling of Salt Stressed Barley Seeds During Initial Stages of Germination by MALDI-MSI and μ-XRF Spectrometry. Frontiers in Plant Science. 2019; 10:1139. doi: 10.3389/fpls.2019.01139.

Guy C, Kaplan F, Kopka J, Selbig J, Hincha DK. Metabolomics of temperature stress. Physiologia plantarum. 2008; 132(2):220–235. doi: 10.1111/j.1399-3054.2007.00999.x.

Hammerton RW, Ho THD. Hormonal Regulation of the Development of Protease and Carboxypeptidase Activities in Barley Aleurone Layers. Plant Physiology. 1986; 80(3):692–697. doi: 10.1104/pp.80.3.692.

Hartl FU, Bracher A, Hayer-Hartl M. Molecular chaperones in protein folding and proteostasis. Nature. 2011; 475(7356):324–332. doi: 10.1038/nature10317.

Hashem Y, Frank J. The jigsaw puzzle of mRNA translation initiation in eukaryotes: a decade of structures unraveling the mechanics of the process. Annual review of biophysics. 2018; 47:125. doi: 10.1146/annurev-biophys-070816-034034.

Hashem Y, des Georges A, Dhote V, Langlois R, Liao HY, Grassucci RA, Hellen CU, Pestova TV, Frank J. Structure of the mammalian ribosomal 43S preinitiation complex bound to the scanning factor DHX29. Cell. 2013; 153(5):1108–1119. doi: 10.1016/j.cell.2013.04.036.

Heinrich P, Kohler C, Ellmann L, Kuerner P, Spang R, Oefner PJ, Dettmer K. Correcting for natural isotope abundance and tracer impurity in MS-, MS/MS- and high-resolution-multiple-tracer-data from stable isotope labeling experiments with IsoCorrectoR. Scientific Reports. 2018; 8(1):1–10. doi: 10.1038/s41598-018-36293-4.

Higgins CF, Payne JW. The Peptide Pools of Germinating Barley Grains: Relation to Hydrolysis and Transport of Storage Proteins. Plant Physiology. 1981; 67(4):785–792. doi: 10.1104/pp.67.4.785.

Hincha DK, Espinoza C, Zuther E. Transcriptomic and metabolomic approaches to the analysis of plant freezing tolerance and cold acclimation. In: *Improving crop resistance to abiotic stress* Wiley Online Library; 2012.p. 255–287.

Hincha DK, Zuther E. Plant Cold Acclimation Methods and Protocols Methods in Molecular Biology. In: *Methods in Molecular Biology*; 2020.

Hinnebusch AG. Structural insights into the mechanism of scanning and start codon recognition in eukaryotic translation initiation. Trends in biochemical sciences. 2017; 42(8):589–611. doi: 10.1016/j.tibs.2017.03.004.

Hung NJ, Johnson AW. Nuclear recycling of the pre-60S ribosomal subunit-associated factor Arx1 depends on Rei1 in Saccharomyces cerevisiae. Molecular and cellular biology. 2006; 26(10):3718–3727. doi: 10.1128/MCB.26.10.3718-3727.2006.

Ingolia NT, Hussmann JA, Weissman JS. Ribosome profiling: Global views of translation. Cold Spring Harbor Perspectives in Biology. 2019; 11(5):1–20. doi: 10.1101/cshperspect.a032698.

Ishihara H, Moraes TA, Arrivault S, Stitt M. Assessing Protein Synthesis and Degradation Rates in Arabidopsis thaliana Using Amino Acid Analysis. Current Protocols. 2021; 1(5):e114. doi: 10.1002/cpz1.114.

Ishihara H, Obata T, Sulpice R, Fernie AR, Stitt M. Quantifying protein synthesis and degradation in arabidopsis by dynamic 13 CO2 labeling and analysis of enrichment in individual amino acids in their free pools and in protein. Plant Physiology. 2015; 168(1):74–93. doi: 10.1104/pp.15.00209.

Iwasaki O, Tanizawa H, Kim KD, Kossenkov A, Nacarelli T, Tashiro S, Majumdar S, Showe LC, Zhang R, Noma Ki. Involvement of condensin in cellular senescence through gene regulation and compartmental reorganization. Nature communications. 2019; 10(1):1–20. doi: 10.1038/s41467-019-13604-5.

Jackson RJ, Hellen CU, Pestova TV. The mechanism of eukaryotic translation initiation and principles of its regulation. Nature reviews Molecular cell biology. 2010; 11(2):113–127. doi: 10.1038/nrm2838.

Jaglo-Ottosen KR, Gilmour SJ, Zarka DG, Schabenberger O, Thomashow MF. Arabidopsis CBF1 overexpression induces COR genes and enhances freezing tolerance. Science. 1998; 280(5360):104–106. doi: 10.1126/science.280.5360.104.

Janská A, Aprile A, Zámečník J, Cattivelli L, Ovesná J. Transcriptional responses of winter barley to cold indicate nucleosome remodelling as a specific feature of crown tissues. Functional and Integrative Genomics. 2011; 11(2):307–325. doi: 10.1007/s10142-011-0213-8.

Johnson KL. Baby, It's Cold Inside: Maintaining Membrane Integrity during Freezing. Plant Physiology. 2018; 177(4):1350–1351. doi: 10.1104/pp.18.00809.

Kaplan F, Kopka J, Haskell DW, Zhao W, Schiller KC, Gatzke N, Sung DY, Guy CL. Exploring the temperature-stress metabolome of Arabidopsis. Plant physiology. 2004; 136(4):4159–4168. doi: 10.1104/pp.104.052142.

1381 **Kipper K**, Hetényi C, Sild S, Remme J, Liiv A. Ribosomal intersubunit bridge B2a is involved in factor-dependent
1382 translation initiation and translational processivity. Journal of molecular biology. 2009; 385(2):405–422. doi:
1383 10.1016/j.jmb.2008.10.065.

1384 **Kirby EJM**. Effect of sowing depth on seedling emergence, growth and development in barley and wheat. Field
1385 Crops Research. 1993; 35(2):101–111. doi: 10.1016/0378-4290(93)90143-B.

1386 **Kopka J**, Schauer N, Krueger S, Birkemeyer C, Usadel B, Bergmüller E, Dörmann P, Weckwerth W, Gibon Y, Stitt
1387 M, et al. GMD@ CSB. DB: the Golm metabolome database. Bioinformatics. 2005; 21(8):1635–1638. doi:
1388 10.1093/bioinformatics/bti236.

1389 **Kosová K**, Vítámvás P, Prášil IT, Klíma M, Renaut J. Plant Proteoforms Under Environmental Stress: Func-
1390 tional Proteins Arising From a Single Gene. Frontiers in Plant Science. 2021; 12:793113. doi: 10.3389/f-
1391 pls.2021.793113.

1392 **Lambers H**. Phosphorus acquisition and utilization in plants. Annual Review of Plant Biology. 2022; 73:11–126.
1393 doi: 10.1146/annurev-arplant-102720-125738.

1394 **Lawrence MG**, Shamsuzzaman M, Kondopaka M, Pascual C, Zengel JM, Lindahl L. The extended loops of ribo-
1395 somal proteins uL4 and uL22 of Escherichia coli contribute to ribosome assembly and protein translation.
1396 Nucleic acids research. 2016; 44(12):5798–5810. doi: 10.1093/nar/gkw493.

1397 **Lea PJ**, Joy KW. Amino Acid Interconversion in Germinating Seeds. In: *Mobilization of Reserves in Germination*;
1398 1983.p. 77–109. doi: 10.1007/978-1-4684-1167-6_5.

1399 **LeFebvre AK**, Korneeva NL, Trutschl M, Cvek U, Duzan RD, Bradley CA, Hershey JW, Rhoads RE. Translation
1400 initiation factor eIF4G-1 binds to eIF3 through the eIF3e subunit. Journal of Biological Chemistry. 2006;
1401 281(32):22917–22932. doi: 10.1074/jbc.M605418200.

1402 **Levitsky LI**, Klein JA, Ivanov MV, Gorshkov MV. Pyteomics 4.0: Five Years of Development of
1403 a Python Proteomics Framework. Journal of Proteome Research. 2019; 18(2):709–714. doi:
1404 10.1021/acs.jproteome.8b00717.

1405 **Li L**, Nelson CJ, Trösch J, Castleden I, Huang S, Millar AH. Protein degradation rate in Arabidopsis thaliana leaf
1406 growth and development. Plant Cell. 2017; 29(2):207–228. doi: 10.1105/tpc.16.00768.

1407 **Li W**, Hu Y, Oh S, Ma Q, Merkurjev D, Song X, Zhou X, Liu Z, Tanasa B, He X, et al. Condensin I and II complexes
1408 license full estrogen receptor α-dependent enhancer activation. Molecular cell. 2015; 59(2):188–202. doi:
1409 10.1016/j.molcel.2015.06.002.

1410 **Lindahl L**. Increasing Complexity of Ribosomes and Their Biogenesis. International Journal of Molecular Sci-
1411 ences. 2022; 23(15):8264. doi: 10.3390/ijms23158264.

1412 **Lopez T**, Dalton K, Frydman J. The mechanism and function of group II chaperonins. Journal of molecular
1413 biology. 2015; 427(18):2919–2930. doi: 10.1016/j.jmb.2015.04.013.

1414 **Lu PD**, Harding HP, Ron D. Translation reinitiation at alternative open reading frames regulates gene expression
1415 in an integrated stress response. The Journal of cell biology. 2004; 167(1):27–33. doi: 10.1083/jcb.200408003.

1416 **Luedemann A**, Strassburg K, Erban A, Kopka J. TagFinder for the quantitative analysis of gas chromatogra-
1417 phy—mass spectrometry (GC-MS)-based metabolite profiling experiments. Bioinformatics. 2008; 24(5):732–
1418 737. doi: 10.1093/bioinformatics/btn023.

1419 **Ma Z**, Bykova NV, Igamberdiev AU. Cell signaling mechanisms and metabolic regulation of germination and
1420 dormancy in barley seeds. Crop Journal. 2017; 5(6):459–477. doi: 10.1016/j.cj.2017.08.007.

1421 **Majumdar R**, Bandyopadhyay A, Maitra U. Mammalian translation initiation factor eIF1 functions with eIF1A
1422 and eIF3 in the formation of a stable 40 S preinitiation complex. Journal of Biological Chemistry. 2003;
1423 278(8):6580–6587. doi: 10.1074/jbc.M210357200.

1424 **Mangelsen E**, Wanke D, Kilian J, Sundberg E, Harter K, Jansson C. Significance of light, sugar, and amino acid
1425 supply for diurnal gene regulation in developing barley caryopses. Plant Physiology. 2010; 153(1):14–33. doi:
1426 10.1104/pp.110.154856.

1427 **Martinez-Seidel F**, Beine-Golovchuk O, Hsieh YC, Kopka J. Systematic review of plant ribosome heterogeneity
1428 and specialization. Frontiers in Plant Science. 2020; 11:948. doi: 10.3389/fpls.2020.00948.

Martinez-Seidel F, Beine-golovchuk O, Hsieh YC, El Eshraky K, Gorka M, Cheong BE, Jimenez-posada EV, Walther D, Skirycz A, Roessner U, Kopka J, Firmino AAP. Spatially enriched paralog rearrangements argue functionally diverse ribosomes arise during cold acclimation in arabidopsis. International Journal of Molecular Sciences. 2021; 22(11):6160. doi: 10.3390/ijms22116160.

Martinez-Seidel F, Hsieh YC, Walther D, Kopka J, Pereira Firmino AA. COSNet$_i$: ComplexOme-Structural Network Interpreter used to study spatial enrichment in metazoan ribosomes. BMC bioinformatics. 2021; 22(1):1–29. doi: 10.1186/s12859-021-04510-z.

Martinez-Seidel F, Suwanchaikasem P, Nie S, Leeming MG, Pereira Firmino AA, Williamson NA, Kopka J, Roessner U, Boughton BA. Membrane-Enriched Proteomics Link Ribosome Accumulation and Proteome Reprogramming With Cold Acclimation in Barley Root Meristems. Frontiers in Plant Science. 2021; 12:656683. doi: 10.3389/fpls.2021.656683.

Micic J, Rodríguez-Galán O, Babiano R, Fitzgerald F, Fernández-Fernández J, Zhang Y, Gao N, Woolford JL, de la Cruz J. Ribosomal protein eL39 is important for maturation of the nascent polypeptide exit tunnel and proper protein folding during translation. Nucleic Acids Research. 2022; 50(11):6453–6473. doi: 10.1093/nar/gkac366.

Middleton AJ, Vanderbeld B, Bredow M, Tomalty H, Davies PL, Walker VK. Plant Cold Acclimation. . 2014; 1166:255–277. doi: 10.1007/978-1-4939-0844-8.

Moin M, Saha A, Bakshi A, Madhav M, Kirti P. Constitutive expression of ribosomal protein L6 modulates salt tolerance in rice transgenic plants. Gene. 2021; 789:145670. doi: 10.1016/j.gene.2021.145670.

Nelson CJ, Alexova R, Jacoby RP, Harvey Millar A. Proteins with high turnover rate in barley leaves estimated by proteome analysis combined with in planta isotope labeling. Plant Physiology. 2014; 166(1):91–108. doi: 10.1104/pp.114.243014.

Nelson CJ, Li L, Millar AH. Quantitative analysis of protein turnover in plants. Proteomics. 2014; 14(4-5):579–592. doi: 10.1002/pmic.201300240.

Nelson CJ, Millar AH. Protein turnover in plant biology. Nature Plants. 2015; 1:1–7. doi: 10.1038/nplants.2015.17.

Nonogaki H. Seed Germination and Reserve Mobilization. In: *eLS* Wiley Online Library; 2008.doi: 10.1002/9780470015902.a0002047.pub2.

Norris K, Hopes T, Aspden JL. Ribosome heterogeneity and specialization in development. Wiley interdisciplinary reviews: RNA. 2021; 12(4):e1644. doi: 10.1002/wrna.1644.

Osama SK, Kerr ED, Yousif AM, Phung TK, Kelly AM, Fox GP, Schulz BL. Proteomics reveals commitment to germination in barley seeds is marked by loss of stress response proteins and mobilisation of nutrient reservoirs. Journal of Proteomics. 2021; 242:104221. doi: 10.1016/j.jprot.2021.104221.

Pakos-Zebrucka K, Koryga I, Mnich K, Ljujic M, Samali A, Gorman AM. The integrated stress response. EMBO reports. 2016; 17(10):1374–1395. doi: 10.15252/embr.201642195.

Parasuraman P, Mulligan P, Walker JA, Li B, Boukhali M, Haas W, Bernards A. Interaction of p190A RhoGAP with eIF3A and other translation preinitiation factors suggests a role in protein biosynthesis. Journal of Biological Chemistry. 2017; 292(7):2679–2689. doi: 10.1074/jbc.M116.769216.

Perez-Riverol Y, Csordas A, Bai J, Bernal-Llinares M, Hewapathirana S, Kundu DJ, Inuganti A, Griss J, Mayer G, Eisenacher M, Perez E, Uszkoreit J, Pfeuffer J, Sachsenberg T, Yilmaz S, Tiwary S, Cox J, Audain E, Walzer M, Jarnuczak AF, et al. The PRIDE database and related tools and resources in 2019: Improving support for quantification data. Nucleic Acids Research. 2019; 47(D1):D442–D450. doi: 10.1093/nar/gky1106.

Peterson JH, Woolhead CA, Bernstein HD. The conformation of a nascent polypeptide inside the ribosome tunnel affects protein targeting and protein folding. Molecular microbiology. 2010; 78(1):203–217. doi: 10.1111/j.1365-2958.2010.07325.x.

Pillet B, Garcia-Gomez JJ, Pausch P, Falquet L, Bange G, de la Cruz J, Kressler D. The dedicated chaperone Acl4 escorts ribosomal protein Rpl4 to its nuclear pre-60S assembly site. PLoS genetics. 2015; 11(10):e1005565. doi: 10.1371/journal.pgen.1005565.

Pisareva VP, Pisarev AV. eIF5 and eIF5B together stimulate 48S initiation complex formation during ribosomal scanning. Nucleic acids research. 2014; 42(19):12052–12069. doi: 10.1093/nar/gkab068.

Reuveni S, Ehrenberg M, Paulsson J. Ribosomes are optimized for autocatalytic production. Nature. 2017; 547(7663):293–297. doi: 10.1038/nature22998.

Rodnina MV. The ribosome as a versatile catalyst: reactions at the peptidyl transferase center. Current Opinion in Structural Biology. 2013; 23(4):595–602. doi: 10.1016/j.sbi.2013.04.012.

Rontein D, Basset G, Hanson AD. Metabolic engineering of osmoprotectant accumulation in plants. Metabolic Engineering. 2002; 4(1):49–56. doi: 10.1006/mben.2001.0208.

Rosental L, Nonogaki H, Fait A. Activation and regulation of primary metabolism during seed germination. Seed Science Research. 2014; 24(1):1–15. doi: 10.1017/S0960258513000391.

Russell JB, Cook GM. Energetics of bacterial growth: Balance of anabolic and catabolic reactions. Microbiological Reviews. 1995; 59(1):48–62. doi: 10.1128/mmbr.59.1.48-62.1995.

Salih KJ, Duncan O, Li L, Trösch J, Millar AH. The composition and turnover of the Arabidopsis thaliana 80S cytosolic ribosome. Biochemical Journal. 2020; 477(16):3019–3032. doi: 10.1042/BCJ20200385.

Salmenkallio M, Sopanen T. Amino Acid and Peptide Uptake in the Scutella of Germinating Grains of Barley, Wheat, Rice, and Maize. Plant Physiology. 1989; 89(4):1285–1291. doi: 10.1104/pp.89.4.1285.

Scheible WR, Morcuende R, Czechowski T, Fritz C, Osuna D, Palacios-Rojas N, Schindelasch D, Thimm O, Udvardi MK, Stitt M. Genome-wide reprogramming of primary and secondary metabolism, protein synthesis, cellular growth processes, and the regulatory infrastructure of Arabidopsis in response to nitrogen. Plant Physiology. 2004; 136(1):2483–2499. doi: 10.1104/pp.104.047019.

Schmidt S, Dethloff F, Beine-Golovchuk O, Kopka J. The REIL1 and REIL2 proteins of Arabidopsis thaliana are required for leaf growth in the cold. Plant physiology. 2013; 163(4):1623–1639. doi: 10.1104/pp.113.223925.

Scoles DR, Yong WH, Qin Y, Wawrowsky K, Pulst SM. Schwannomin inhibits tumorigenesis through direct interaction with the eukaryotic initiation factor subunit c (eIF3c). Human molecular genetics. 2006; 15(7):1059–1070. doi: 10.1093/hmg/ddl021.

Seki M, Narusaka M, Ishida J, Nanjo T, Fujita M, Oono Y, Kamiya A, Nakajima M, Enju A, Sakurai T, et al. Monitoring the expression profiles of 7000 Arabidopsis genes under drought, cold and high-salinity stresses using a full-length cDNA microarray. The Plant Journal. 2002; 31(3):279–292. doi: 10.1046/j.1365-313X.2002.01359.x.

Shi Z, Fujii K, Kovary KM, Genuth NR, Röst HL, Teruel MN, Barna M. Heterogeneous ribosomes preferentially translate distinct subpools of mRNAs genome-wide. Molecular cell. 2017; 67(1):71–83. doi: 10.1016/j.molcel.2017.05.021.

Shin BS, Maag D, Roll-Mecak A, Arefin MS, Burley SK, Lorsch JR, Dever TE. Uncoupling of initiation factor eIF5B/IF2 GTPase and translational activities by mutations that lower ribosome affinity. Cell. 2002; 111(7):1015–1025. doi: 10.1016/S0092-8674(02)01171-6.

Shore D, Albert B. Ribosome biogenesis and the cellular energy economy. Current Biology. 2022; 32(12):R611–R617. doi: 10.1016/j.cub.2022.04.083.

Shrestha V, Yobi A, Slaten ML, Chan YO, Holden S, Gyawali A, Flint-Garcia S, Lipka AE, Angelovici R. Multiomics approach reveals a role of translational machinery in shaping maize kernel amino acid composition. Plant physiology. 2022; 188(1):111–133. doi: 10.1093/plphys/kiab390.

Shutov AD, Vaintraub IA. Degradation of storage proteins in germinating seeds. Phytochemistry. 1987; 26(6):1557–1566. doi: 10.1016/S0031-9422(00)82245-1.

Slavov N, Semrau S, Airoldi E, Budnik B, van Oudenaarden A. Differential Stoichiometry among Core Ribosomal Proteins. Cell Reports. 2015; 13(5):865–873. doi: 10.1016/j.celrep.2015.09.056.

Spiess C, Meyer AS, Reissmann S, Frydman J. Mechanism of the eukaryotic chaperonin: protein folding in the chamber of secrets. Trends in cell biology. 2004; 14(11):598–604. doi: 10.1016/j.tcb.2004.09.015.

Sreenivasulu N, Usadel B, Winter A, Radchuk V, Scholz U, Stein N, Weschke W, Strickert M, Close TJ, Stitt M, Graner A, Wobus U. Barley grain maturation and germination: Metabolic pathway and regulatory network commonalities and differences highlighted by new MapMan/PageMan profiling tools. Plant Physiology. 2008; 146(4):1738–1758. doi: 10.1104/pp.107.111781.

Stelter P, Huber FM, Kunze R, Flemming D, Hoelz A, Hurt E. Coordinated ribosomal L4 protein assembly into the pre-ribosome is regulated by its eukaryote-specific extension. Molecular cell. 2015; 58(5):854–862. doi: 10.1016/j.molcel.2015.03.029.

Takahashi D, Zuther E, Hincha DK. Analysis of Changes in Plant Cell Wall Composition and Structure During Cold Acclimation. In: *Plant cold acclimation* Springer; 2020.p. 255–268. doi: 10.1007/978-1-0716-0660-5_17.

Tamm T, Kisly I, Remme J. Functional interactions of ribosomal intersubunit bridges in Saccharomyces cerevisiae. Genetics. 2019; 213(4):1329–1339. doi: 10.1534/genetics.119.302777.

Thomashow MF. Plant cold acclimation: Freezing tolerance genes and regulatory mechanisms. Annual Review of Plant Biology. 1999; 50:571–599. doi: 10.1146/annurev.arplant.50.1.571.

Verbelen JP, De Cnodder T, Le J, Vissenberg K, Baluška F. The root apex of arabidopsis thaliana consists of four distinct zones of growth activities: Meristematic zone, transition zone, fast elongation zone and growth terminating zone. Plant Signaling and Behavior. 2006; 1(6):296–304. doi: 10.4161/psb.1.6.3511.

Verduyn C, Stouthamer AH, Scheffers WA, van Dijken JP. A theoretical evaluation of growth yields of yeasts. Antonie van Leeuwenhoek. 1991; 59(1):49–63. doi: 10.1007/BF00582119.

Wang H, Ru Y, Sanchez-Carbayo M, Wang X, Kieft JS, Theodorescu D. Translation Initiation Factor eIF3b Expression in Human Cancer and Its Role in Tumor Growth and Lung Colonization eIF3b in Patient Outcome and Experimental Tumor Growth and Metastasis. Clinical cancer research. 2013; 19(11):2850–2860. doi: 10.1158/1078-0432.CCR-12-3084.

Waterworth WM, West CE, Bray CM. The barley scutellar peptide transporter: Biochemical characterization and localization to the plasma membrane. Journal of Experimental Botany. 2000; 51(348):1201–1209. doi: 10.1093/jxb/51.348.1201.

Wruck F, Tian P, Kudva R, Best RB, von Heijne G, Tans SJ, Katranidis A. The ribosome modulates folding inside the ribosomal exit tunnel. Communications biology. 2021; 4(1):1–8. doi: 10.1038/s42003-021-02055-8.

Xiong W, Zhang J, Lan T, Kong W, Wang X, Liu L, Chen X, Mo B. High resolution RNA-seq profiling of genes encoding ribosomal proteins across different organs and developmental stages in Arabidopsis thaliana. Plant direct. 2021; 5(5):e00320. doi: 10.1002/pld3.320.

Xu TR, Lu RF, Romano D, Pitt A, Houslay MD, Milligan G, Kolch W. Eukaryotic translation initiation factor 3, subunit a, regulates the extracellular signal-regulated kinase pathway. Molecular and cellular biology. 2012; 32(1):88–95. doi: 10.1128/MCB.05770-11.

Yébenes H, Mesa P, Muñoz IG, Montoya G, Valpuesta JM. Chaperonins: two rings for folding. Trends in biochemical sciences. 2011; 36(8):424–432. doi: 10.1016/j.tibs.2011.05.003.

Yu H, Kong X, Huang H, Wu W, Park J, Yun DJ, Lee Bh, Shi H, Zhu JK. STCH4/REIL2 confers cold stress tolerance in Arabidopsis by promoting rRNA processing and CBF protein translation. Cell Reports. 2020; 30(1):229–242. doi: 10.1016/j.celrep.2019.12.012.

Zhang W, Zhang J, Xu C, Li N, Liu H, Ma J, Zhu Y, Xie H. LFQ uant: a label-free fast quantitative analysis tool for high-resolution LC-MS/MS proteomics data. Proteomics. 2012; 12(23-24):3475–3484. doi: 10.1002/pmic.201200017.

Zhou M, Sandercock AM, Fraser CS, Ridlova G, Stephens E, Schenauer MR, Yokoi-Fong T, Barsky D, Leary JA, Hershey JW, et al. Mass spectrometry reveals modularity and a complete subunit interaction map of the eukaryotic translation factor eIF3. Proceedings of the National Academy of Sciences. 2008; 105(47):18139–18144. doi: 10.1073/pnas.0801313105.

Zúñiga GE, Fernandez J, Cristi R, Alberdi M, Corcuera LJ. Lipid changes in barley seedlings subjected to water and cold stress. Phytochemistry. 1990; 29(10):3087–3090. doi: 10.1016/0031-9422(90)80162-A.

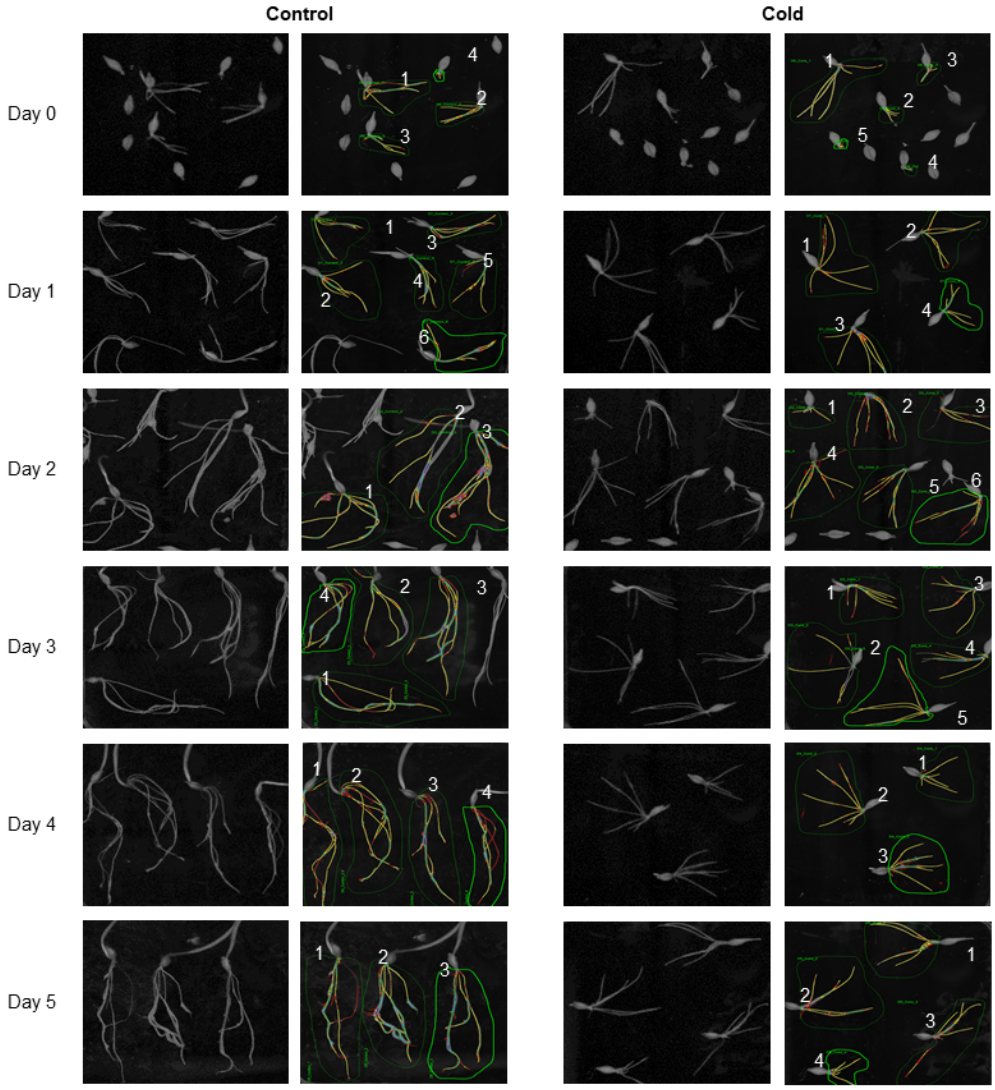

1569

Figure 1–Figure supplement 1. Root phenotype during germination assay in optimal control and suboptimal cold temperatures. Root systems were scanned at each time-point, beginning from day 0 until day 5. The columns on the left represent roots reared at optimal temperature and 3-6 selected representative root systems for phenotypic analyses The columns on the right represent the germination assay of roots acclimated to cold temperature during each time-point and 3-6 representative seedlings were phenotypically analyzed. winRHIZO software was used.

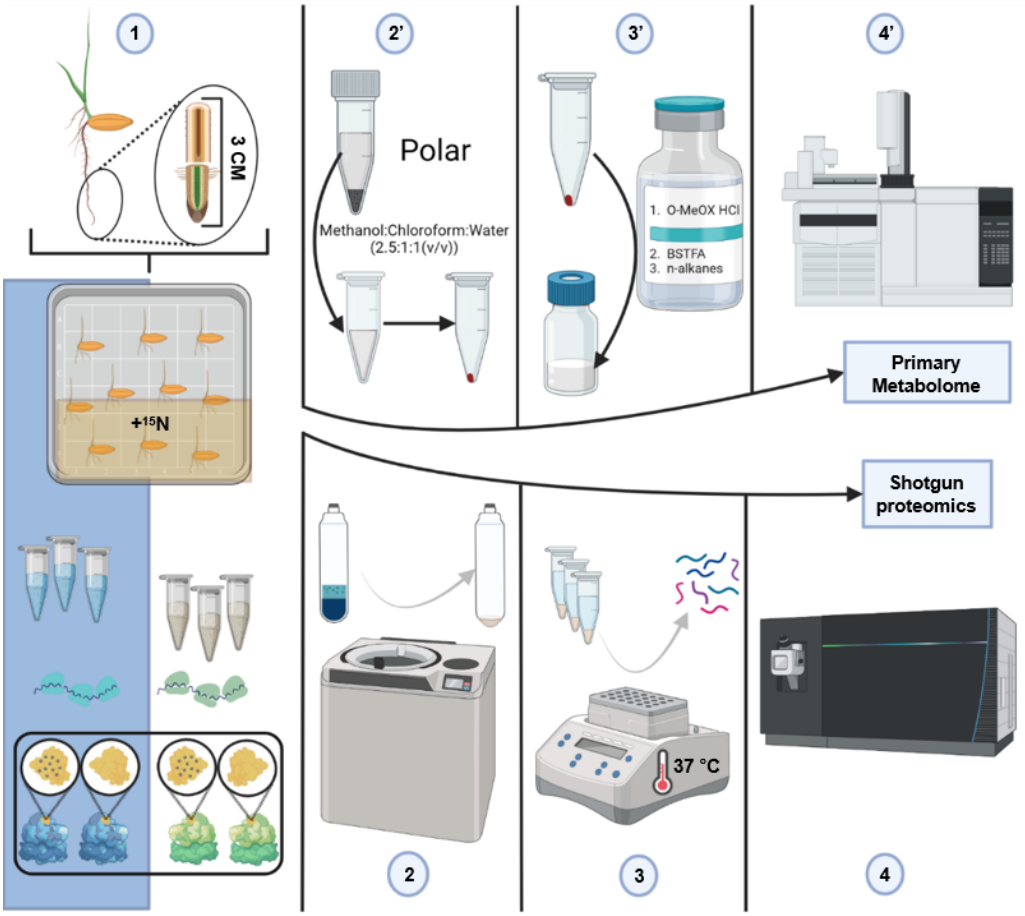

Figure 1–Figure supplement 2. Summary of the methodological workflow to achieve measurements of protein synthesis and abundance in barley root tips. (1) harvesting of root tips from barley seedlings and division into two 1.5cm segments. Barley seedlings were germinated in two temperature regimes with one quarter of the plants having additional labelled nitrogen source and another quarter the same non-labelled nitrogen sources. (2) grinding of pooled tissue using liquid nitrogen, mortar and pestle followed by ribosome enrichment by ultracentrifuge-mediated large cellular complex subproteome extraction and pelleting. (3) Reduction, alkylation, trypsin digestion and peptide cleaning. (4) LC-MS/MS. (2') Extraction of the polar primary metabolome using a methanol, chloroform, water ratio of 2.5:1:1 (V/V). (3') Methoximation and silylation of primary metabolites. (4') GC-ToF-MS multiplexed GC-APCI-MS.

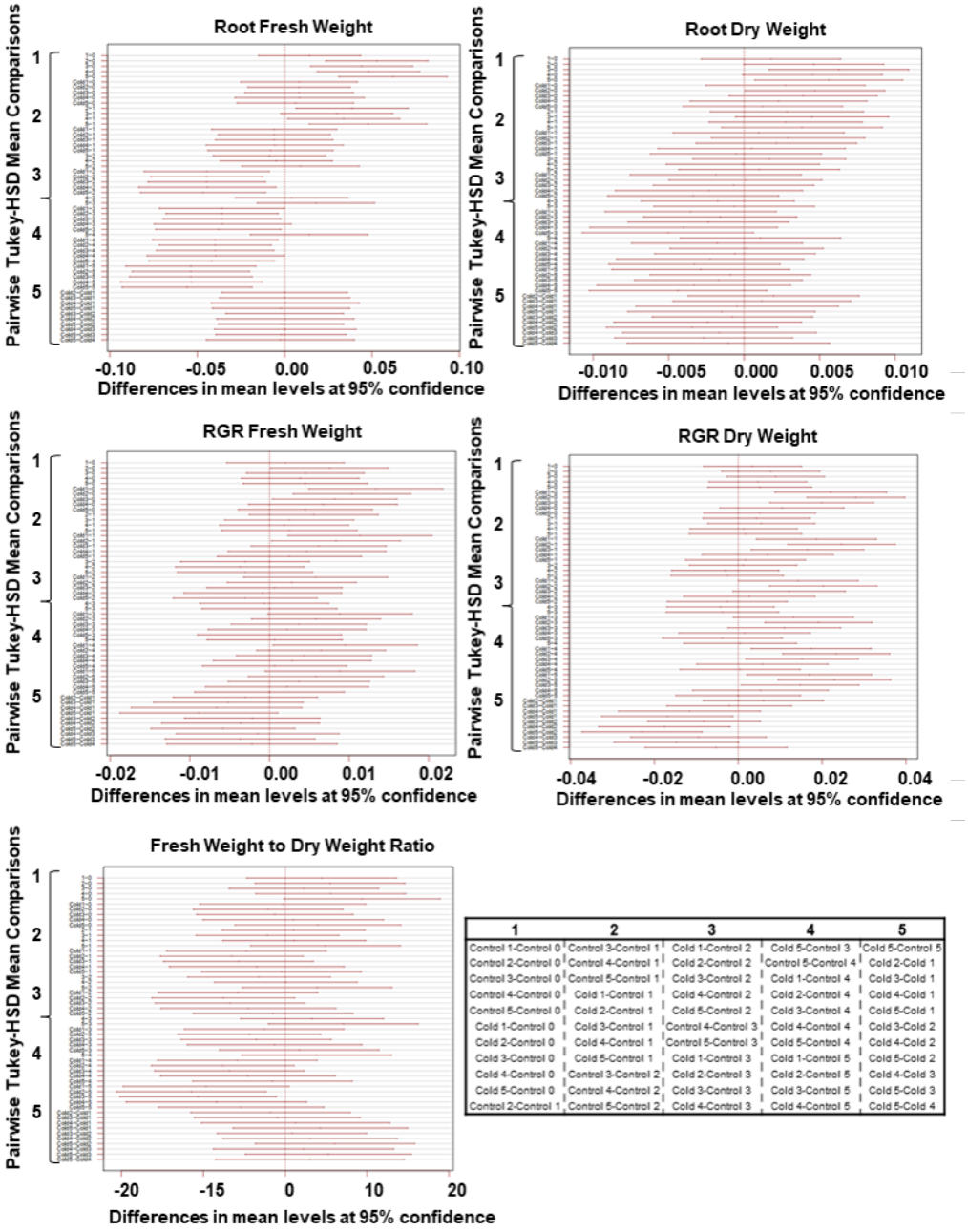

Figure 2–Figure supplement 1. Summary of 95% confidence level Tukey-HSD statistical differences in mean levels of growth related variables across treated and control barley seedlings. Each panel reflects the pairwise comparison across all treatments of specific variables reflecting plant growth. The table on the lower right panel contains the sequential order of the mean comparisons in the plots in five groups. The groupings are signalled in the y-axes of the plots for reference.

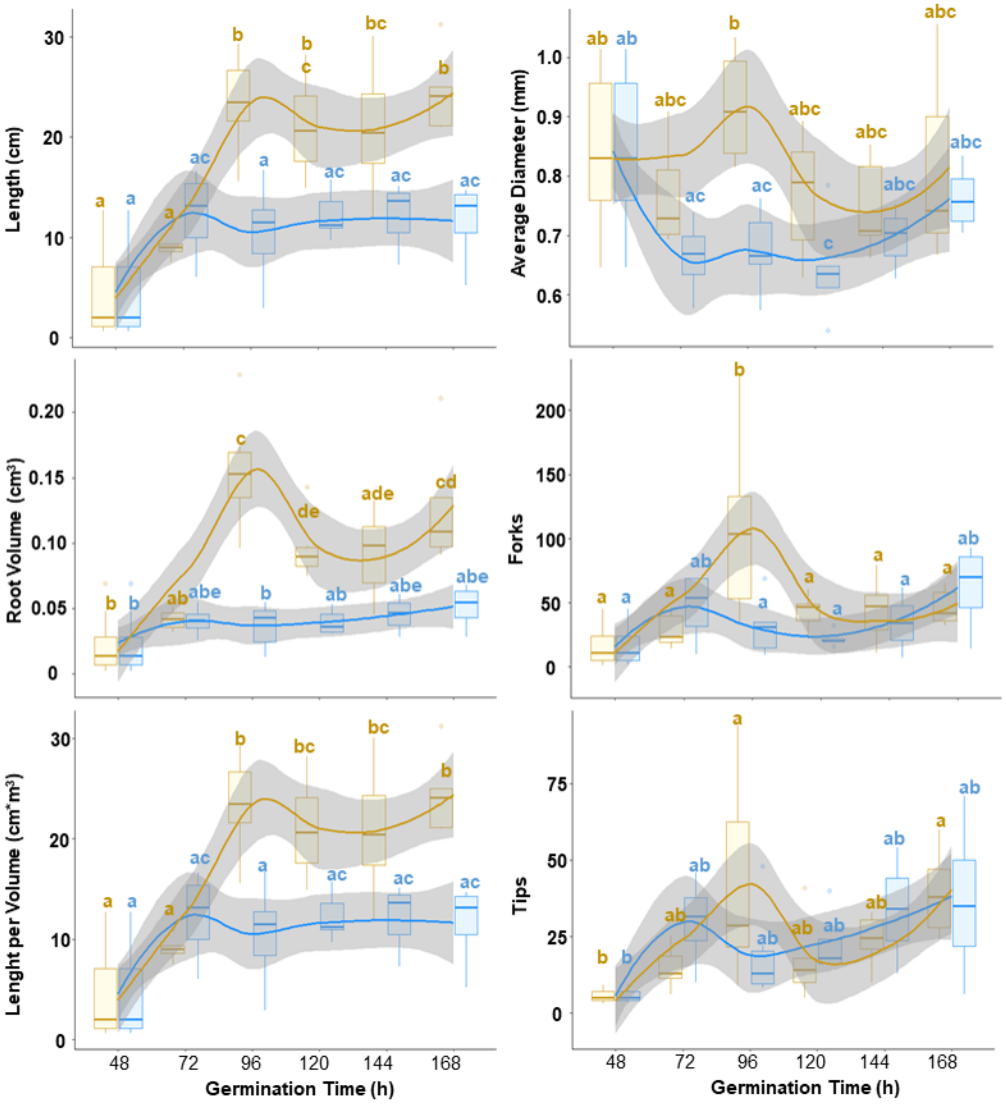

Figure 2–Figure supplement 2. Statistical differences in mean levels (95% confidence level Tukey-HSD) of growth related variables derived from scanning treated and control barley seedlings at each time-point. Each panel reflects plant growth dynamics at control and sub-optimal low temperature. All variables were measured using scanned images and the winRHIZO software.

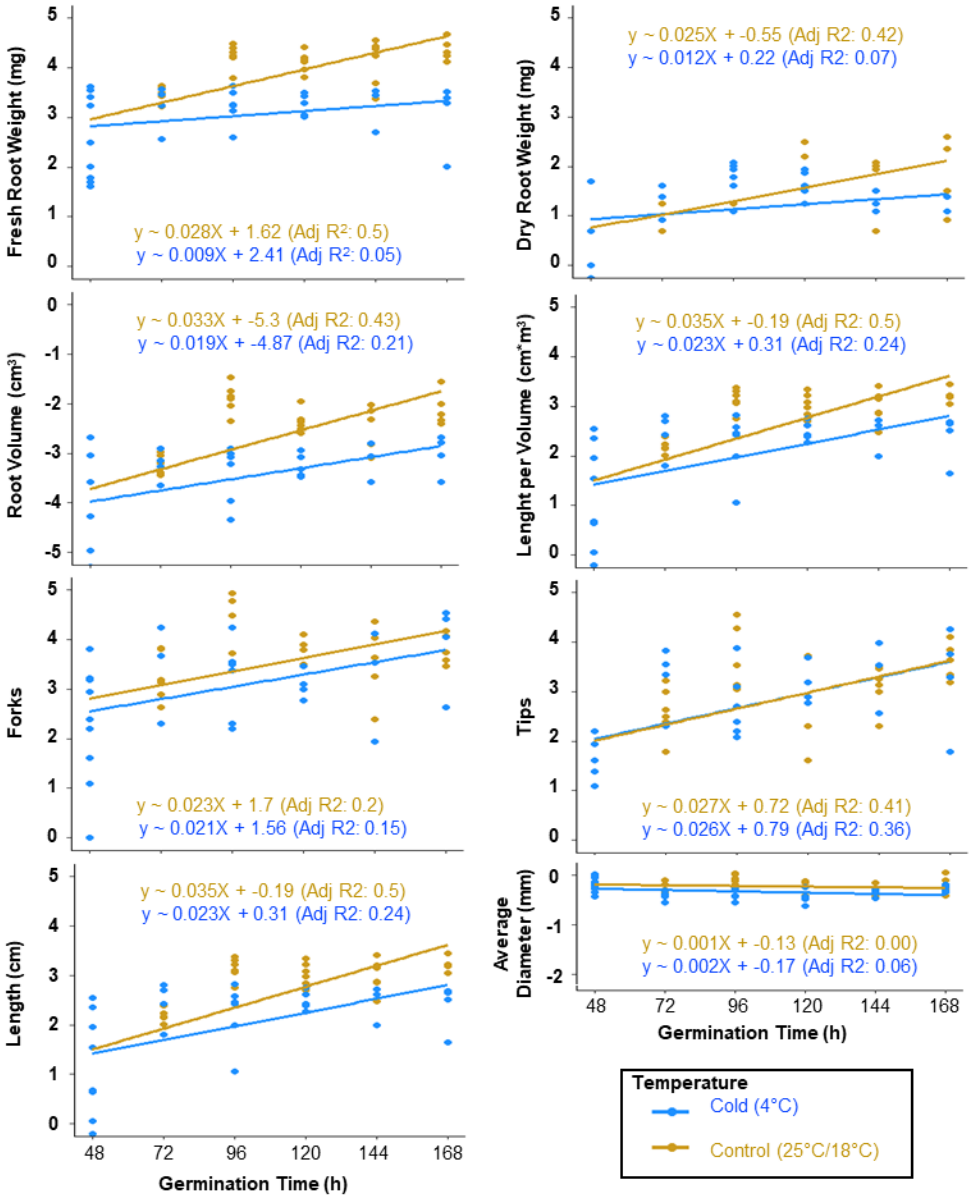

Figure 2–Figure supplement 3. Linear regression after natural logarithm transformation of growth related variables. Growth variables were transformed using the natural logarithm (Ln) and a subsequent linear regression was made on the transformed vector. The fitting was evaluated using the adjusted r^2, and the respective equation was derived from the linear fitting following the equation of a straight line (i.e., f(x) = mX + b, where m represents the slope and b the intercept). The slope represents mean growth rate for each variable and its biological accuracy depends on the adjusted r^2 being close to 1.

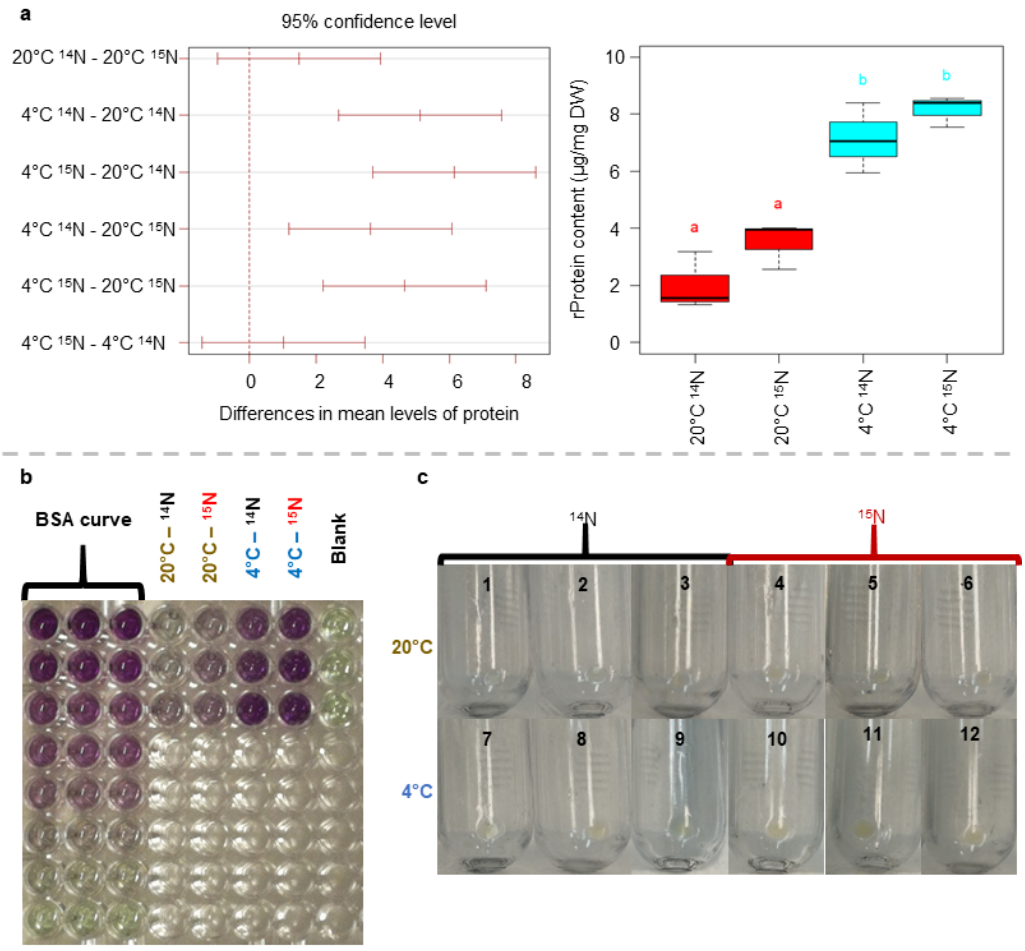

1574

Figure 5–Figure supplement 1. Summary of 95% confidence level Tukey-HSD statistical differences in mean levels of protein content from proteome fractions enriched in ribosomes across treated and control barley seedlings. Also relates to Table S5. (a left-panel) Pairwise comparisons across all treatments of a proteome fraction enriched in ribosomal protein content. The paired mean differences are signalled in the y-axis of the plot for reference. (a right-panel) Boxplot representation of the ribosomal protein content mean differences across temperature regimes, significance is signalled by colour transitions and different letters above the boxes. (b) Features the original photograph of the plate used for the bicinchoninic acid assay from which the results portrayed in panel "a" were derived. (c) Features the original photographs of the ribosome-enriched pellets from all experimental samples after passing through the 60 % sucrose cushion.

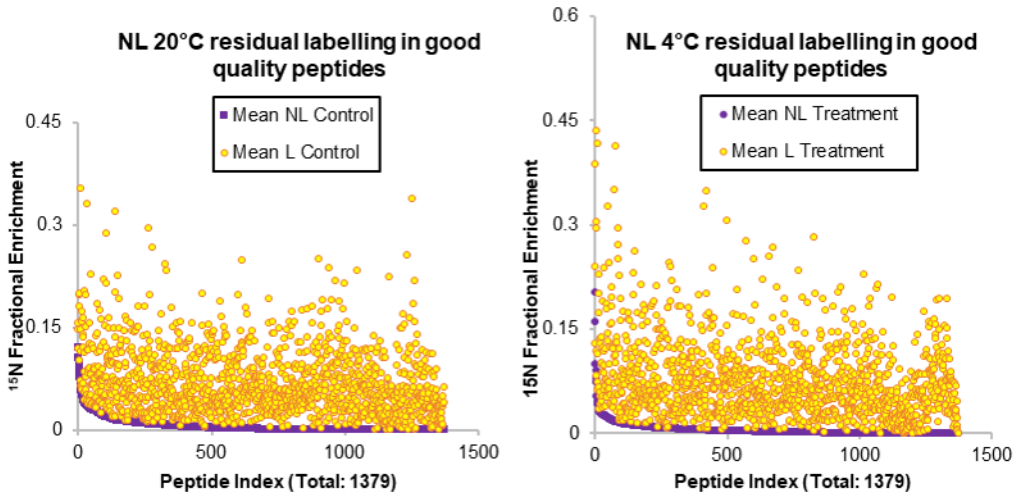

Figure 5–Figure supplement 2. Subset of peptides considered as having optimal quality for interpretation of their relative fractional synthesis rates during the physiological transition of roots from germinating barley seedlings from optimal to sub-optimal temperature. The peptides in the list have all the necessary isotopolog abundances to calculate enrichment percentages in both temperature treatments. Many of the peptides in the list still conserve "noise" in the sense of false enrichment in the non-labelled samples (purple dots in both graphs). Nevertheless this noise is mostly below 1 % enrichment and always below the labelled samples. In both graphs the enrichment fraction is portrayed in the y-axis while the x.axis contains the peptide indexes, which have been sorted from highest to lowest noise in the non-labelled samples. Thus both graphs present a different peptide order. The left graph contains the information of peptides as monitored in samples derived from roots of germinating seedlings growing at an average of 22°C. The right graph contains the information of peptides as monitored in samples derived from roots of germinating seedlings growing at an average of 4°C.

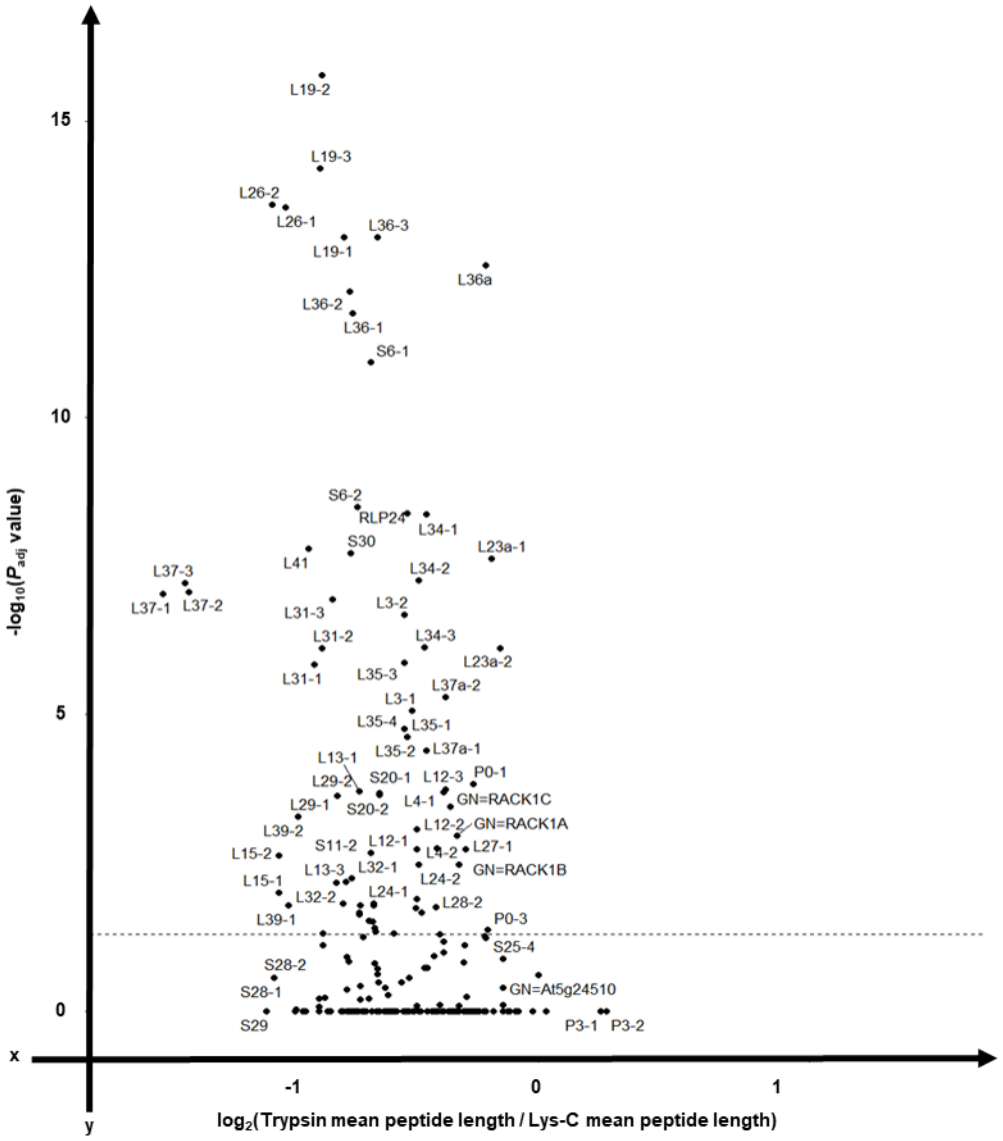

1576

Figure 6–Figure supplement 1. Volcano plot outlining the differences in mean peptide length produced with Lys-C or Trypsin, during an *in silico* protease digestion test, as proteases to digest the Arabidopsis signature plant ribosomal proteome. Also related to Table S6. Protease digestion *in silico* was performed with the free software Protein-Digestion-Simulator. The resulting plot from analysing the digestions contains in the x-axis the log_2 of the ratio between mean peptide lengths from Trypsin and Lys-C digestion. Similarly, the y-axis contains the -log_{10} of the P_{adj} value from the statistical comparison of mean peptide lengths per each specific barley ribosomal protein. Note that with the exception of RPS21 and RPP3 all the other ribosomal proteins have shorter mean peptide lengths when digested with Trypsin as compared to Lys-C. The horizontal dotted line signals the significance boundary and thus all the proteins above this line have significantly shorter mean peptide lengths when digested with Trypsin as compared to Lys-C.

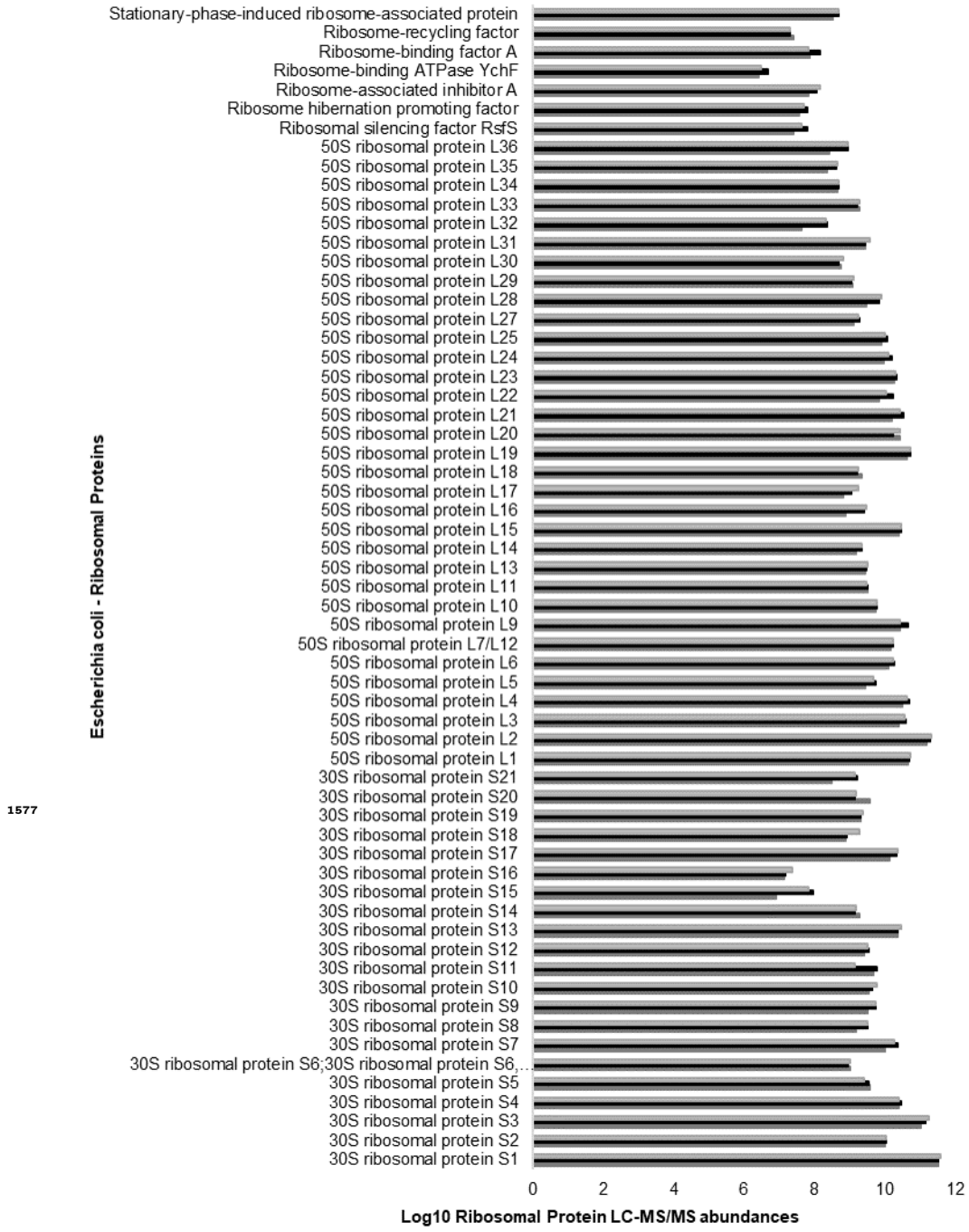

1577

Figure 6–Figure supplement 2. Positive control and complete coverage of *escherichia coli* 70S ribosomal proteome from a commercially available preparation used to verify the ribosomal proteomics pipeline. Also related to Table S7. The ribosomal proteomics pipeline was verified with three independent replicates from the same commercial preparation of *escherichia coli* 70S ribosomes (P0763S, NEB, Australia). The pipeline tested included ribosome extraction, subsequent purification through a sucrose cushion, resuspension of the pelleted complexes with a chaotrope to promote ribosomal protein dissociation and rRNA removal before SP3 beads binding of the ribosomal proteins for protease digestion. The coverage of the 70S ribosomes was full, with 21 proteins from the 30S small subunit and 33 from the 50S large subunit, plus a small set of ribosome associated factors. The height of the triplicate bars in the plot (i.e., x-axis unit) represents the log_{10} ribosomal protein abundances as measured by LC-MS/MS from the control ribosomal complexes. The y-axis contains the common name of the identified ribosomal proteins.

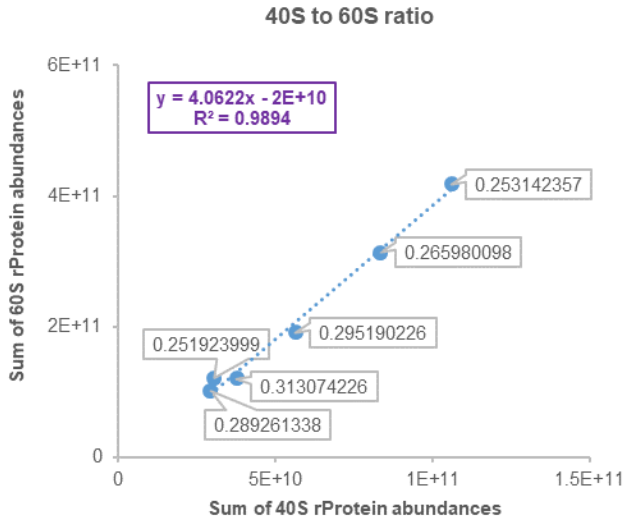

Figure 6–Figure supplement 3. Ratio between 40S SSU and 60S LSU abundances across experimental samples. Also related to Table S4 - Tab C3. The y-axis features the sum of all detected and reliable 60S rProtein abundances. Likewise the x-axis features the sum of all detected and reliable 40S rProtein abundances. The labels at each point are the 40S to 60S ratio as calculated for each sample, note that the ratios all lie between 0.25 and 0.31, which means that 60S proteins are always at a relationship of 3 to 1 with 40S proteins and this aligns with the number of protein paralogs per subunit. Finally, since the ratios are constant, note that the dispersion of the dots is well adjusted to a linear regression model with an r^2 above 0.98.

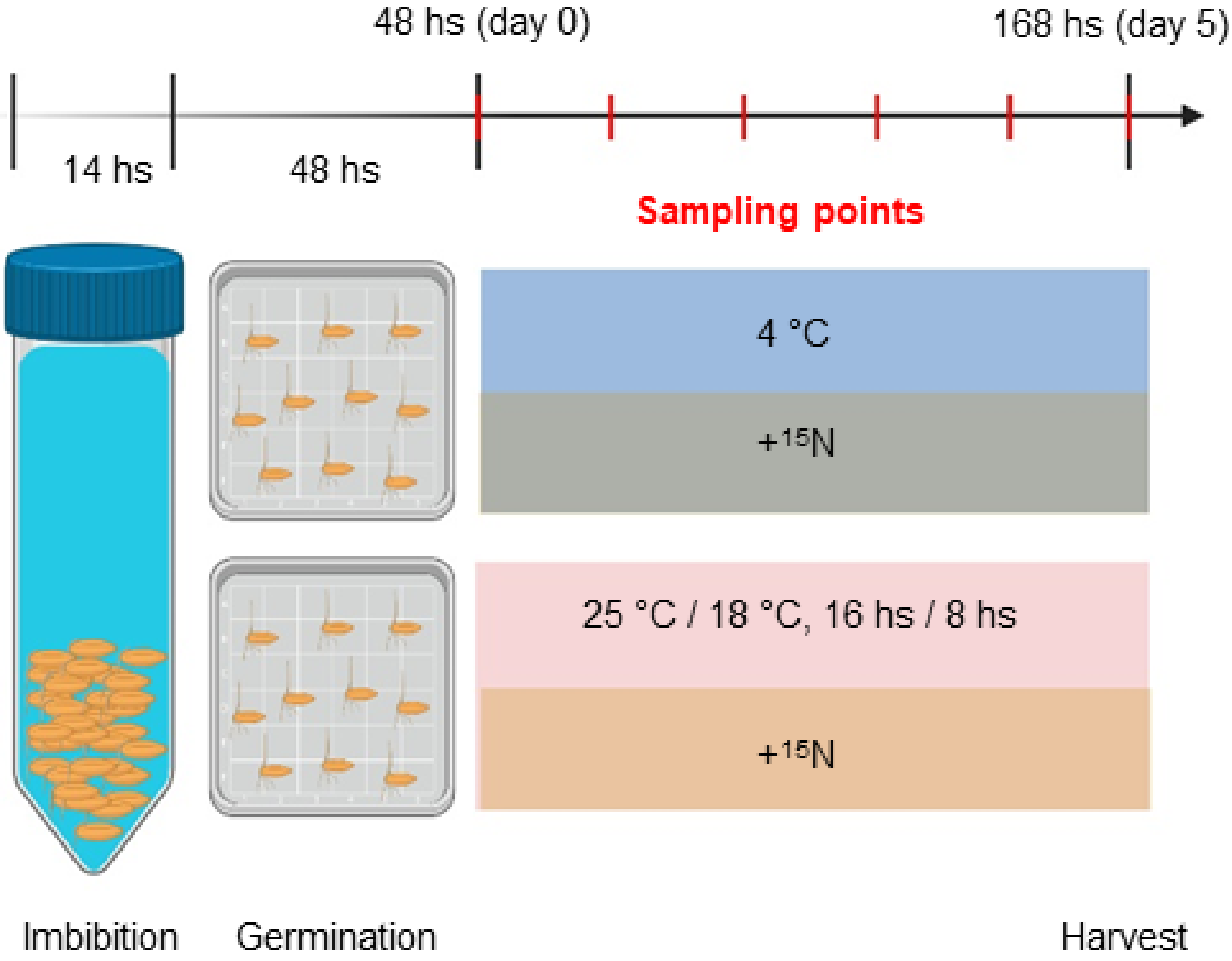
48 hs (day 0)
168 hs (day 5)
14 hs
48 hs
Sampling points
4 °C
+15N
25 °C / 18 °C, 16 hs / 8 hs
+15N
Imbibition
Germination
Harvest

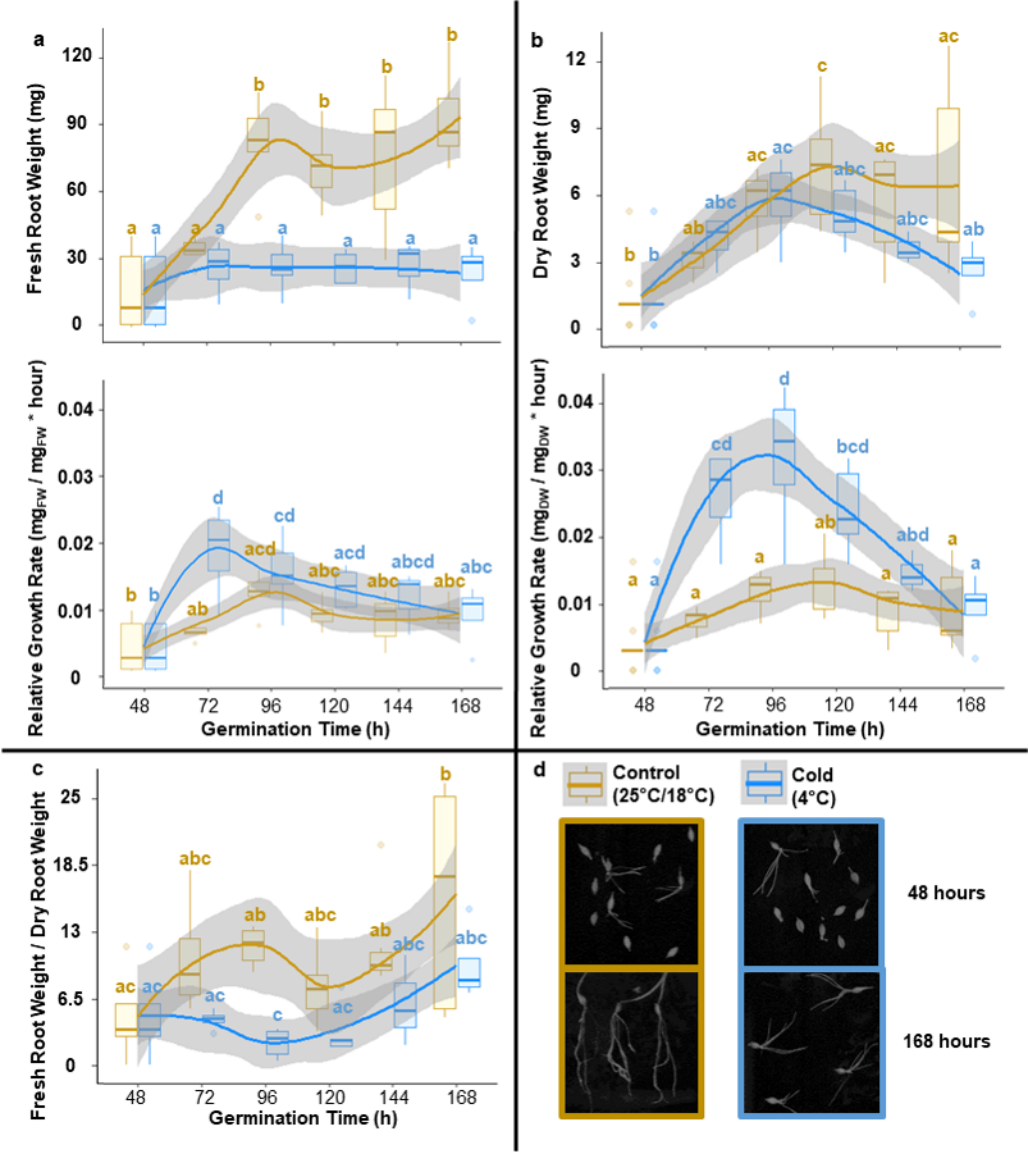
a
Fresh Root Weight (mg)
Relative Growth Rate (mg$_{FW}$ / mg$_{FW}$ * hour)
Germination Time (h)
b
Dry Root Weight (mg)
Relative Growth Rate (mg$_{DW}$ / mg$_{DW}$ * hour)
Germination Time (h)
c
Fresh Root Weight / Dry Root Weight
Germination Time (h)
d
Control (25°C/18°C)
Cold (4°C)
48 hours
168 hours

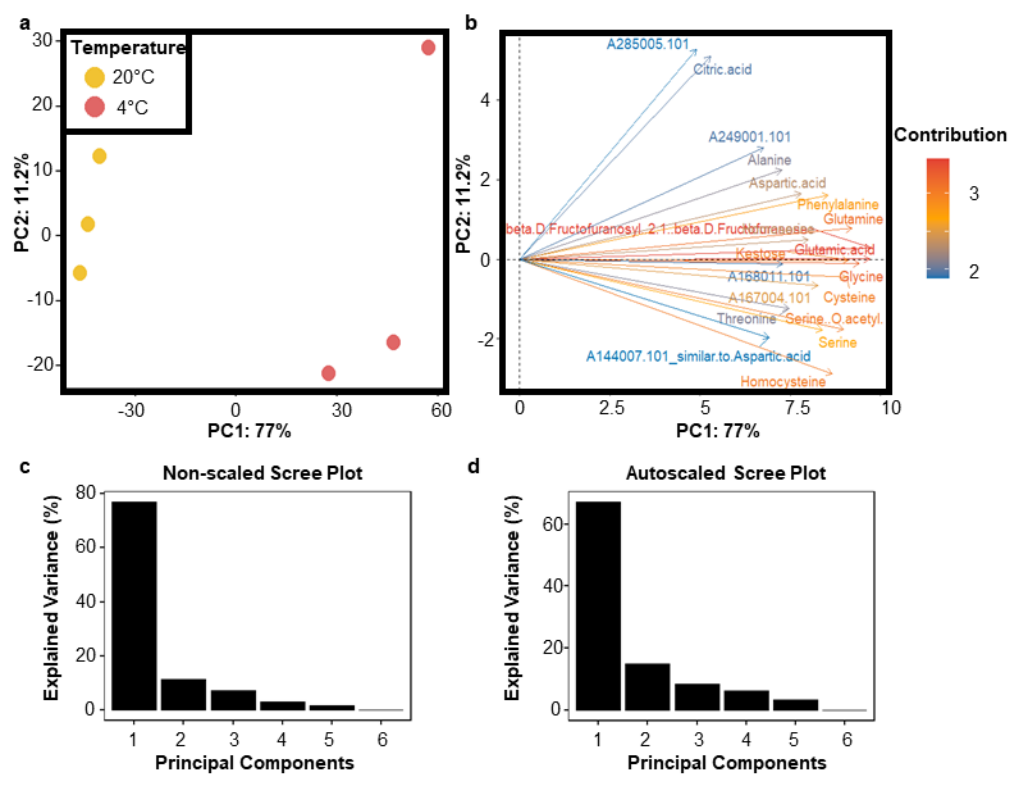
a
Temperature
20°C
4°C
PC2: 11.2%
PC1: 77%
b
A285005.101
Citric.acid
A249001.101
Alanine
Aspartic.acid
Phenylalanine
Glutamine
beta.D.Fructofuranosyl..2.1..beta.D.Fructofuranoside
Kestose
Glutamic.acid
A168011.101
Glycine
A167004.101
Cysteine
Threonine
Serine
O.acetyl.
Serine
A144007.101_similar.to.Aspartic.acid
Homocysteine
Contribution
3
2
PC2: 11.2%
PC1: 77%
c
Non-scaled Scree Plot
Explained Variance (%)
Principal Components
d
Autoscaled Scree Plot
Explained Variance (%)
Principal Components

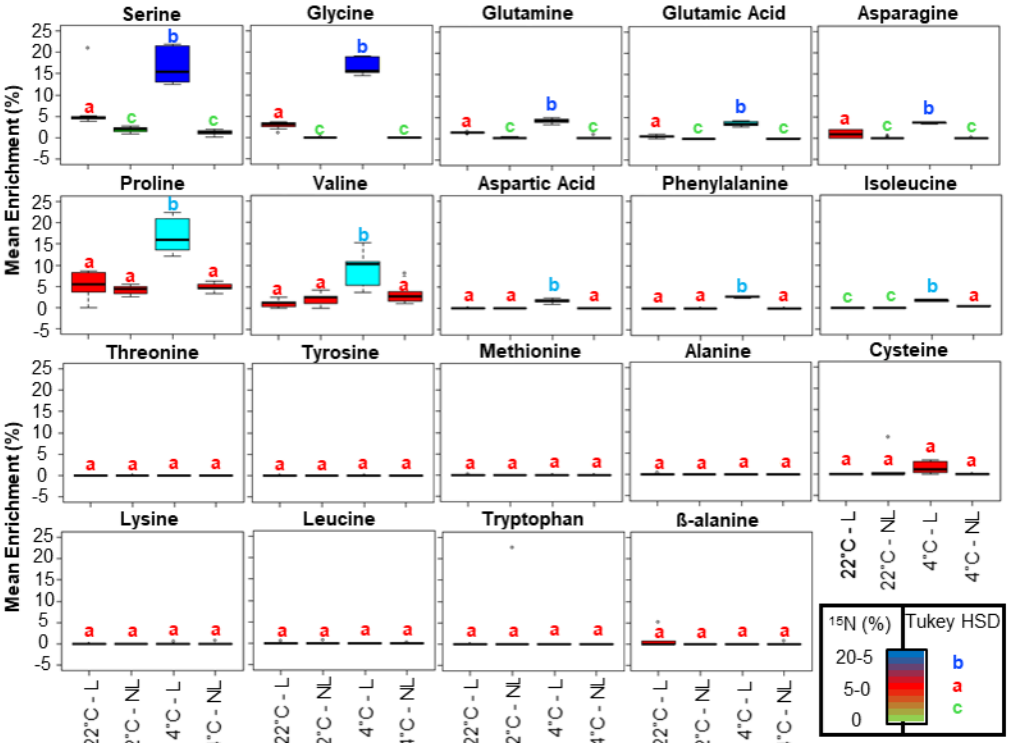
Serine
Glycine
Glutamine
Glutamic Acid
Asparagine
Proline
Valine
Aspartic Acid
Phenylalanine
Isoleucine
Threonine
Tyrosine
Methionine
Alanine
Cysteine
Lysine
Leucine
Tryptophan
ß-alanine
Mean Enrichment (%)
25
20
15
10
5
0
-5
22°C - L
22°C - NL
4°C - L
4°C - NL
15N (%)
Tukey HSD
20-5
5-0
0
b
a
c

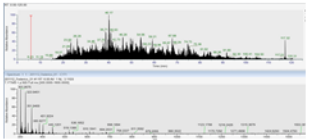

.RAW chromatograms

R package ProtSynthesis:
https://github.com/MSeidelFed/ProtSynthesis

Detailed usage instructions:
https://github.com/mgleeming/isotopeEnrichment

ProteoWizard

MaxQuant

.mzML

MaxQuant „evidence.txt"

isotopeEnrichment.py

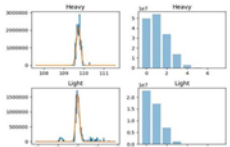

Isotopolog intensities

isotopeEnrichmentR

IsoCorrectoR input

.CSV

IsoCorrectoR::IsoCorrection()

%

EnrichmentSet.R

Enrichment percentages (non-corrected LPFs)

Subset of Labelled peptides

AnnotateProteins.R

Annotate proteins, highlight sequence coverage and enrichment percentage SD

LPFcorrection.R

Correct labelled peptide fraction (LPF) using enrichments in amino acid precursors

Protein fractional synthesis rates:

$K_s = LPF * \mu(RGR_{pf}) * 100$

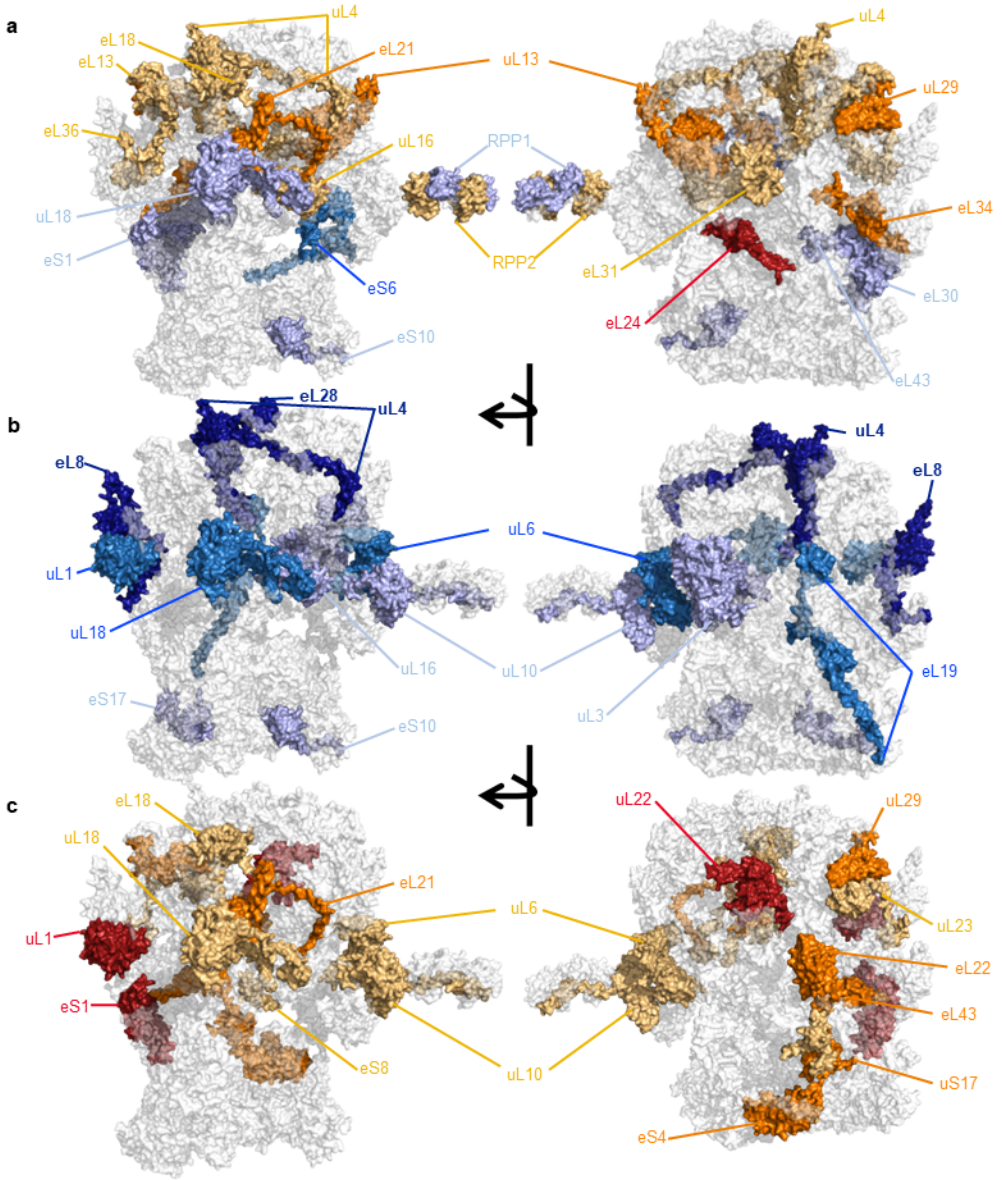
a
uL4
eL18
eL13
eL21
uL13
eL36
uL16
RPP1
uL18
eS1
eS6
RPP2
eS10
uL4
uL29
eL34
eL31
eL30
eL24
eL43
b
eL28
uL4
eL8
uL6
uL1
uL18
uL16
uL10
eS17
eS10
uL4
eL8
eL19
uL3
c
eL18
uL18
eL21
uL1
eS1
eS8
uL6
uL10
uL22
uL29
uL23
eL22
eL43
uS17
eS4

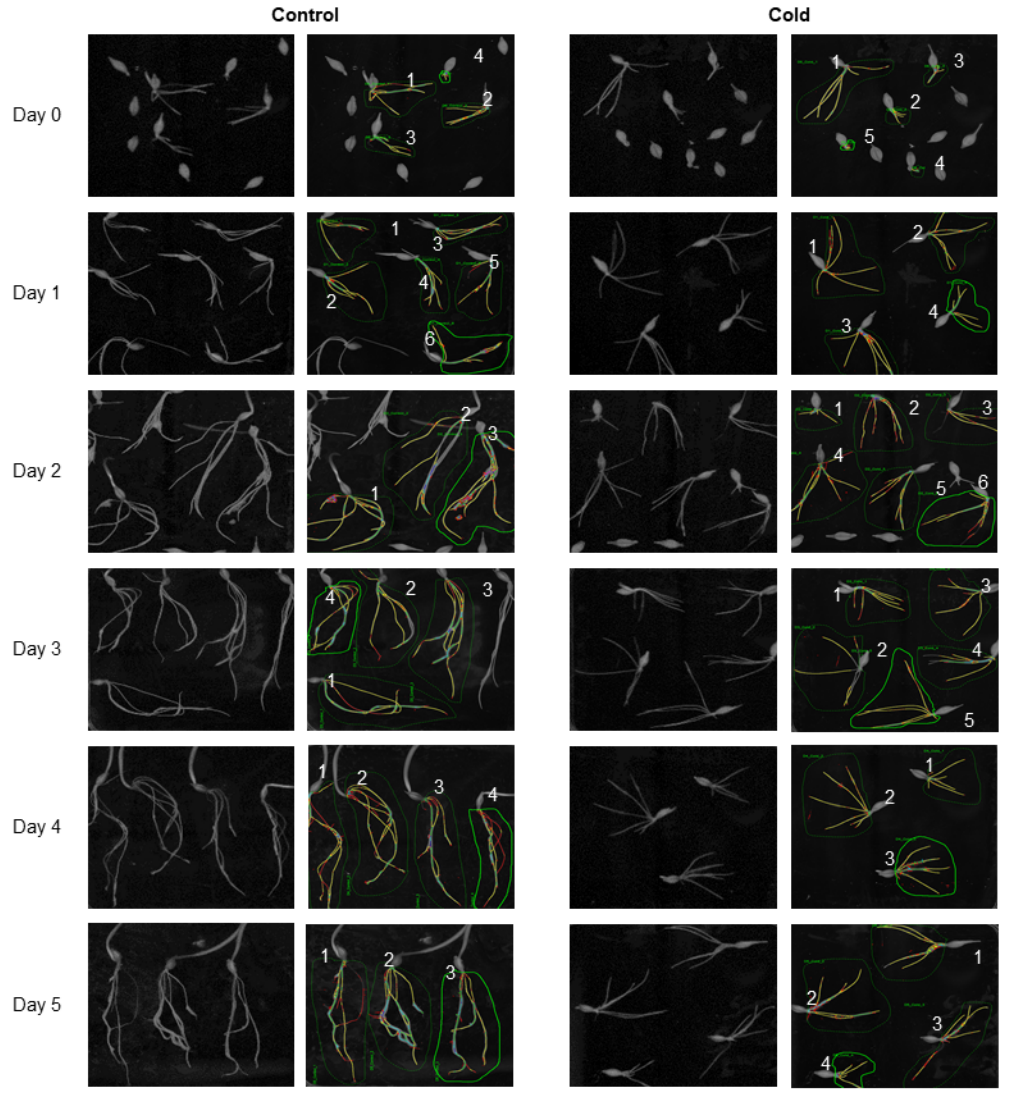
Control
Cold
Day 0
Day 1
Day 2
Day 3
Day 4
Day 5

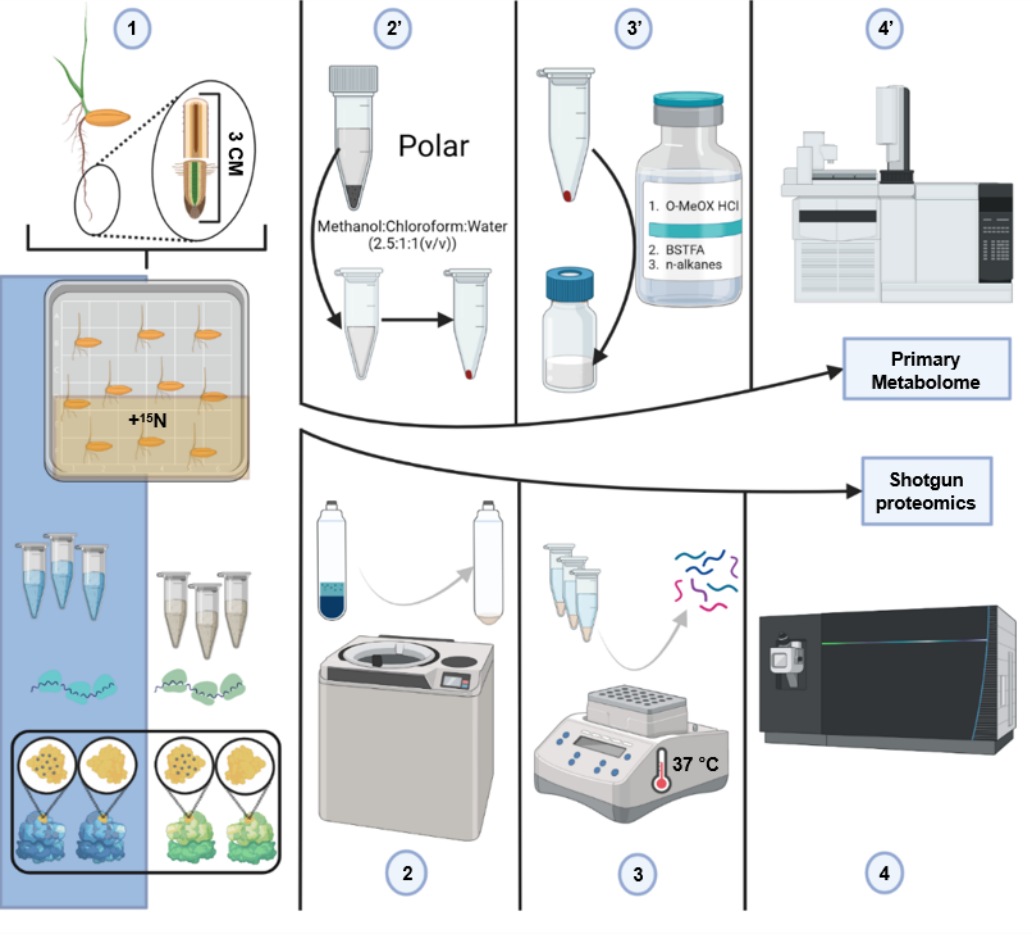
1
3 CM
+15N
2'
Polar
Methanol:Chloroform:Water
(2.5:1:1(v/v))
3'
1. O-MeOX HCl
2. BSTFA
3. n-alkanes
4'
Primary
Metabolome
Shotgun
proteomics
37 °C
2
3
4

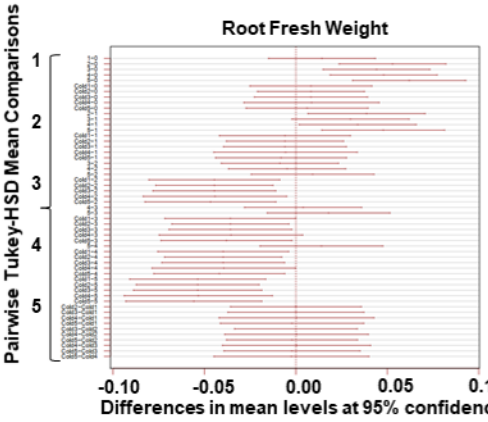

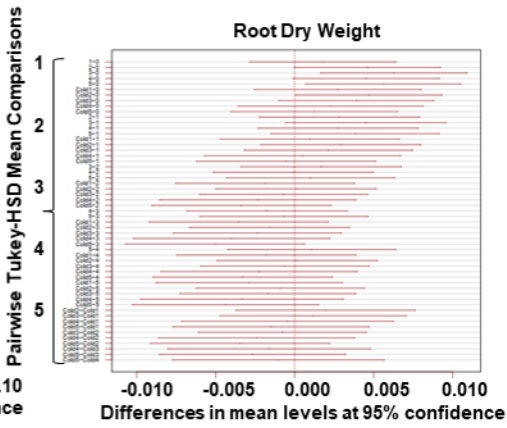

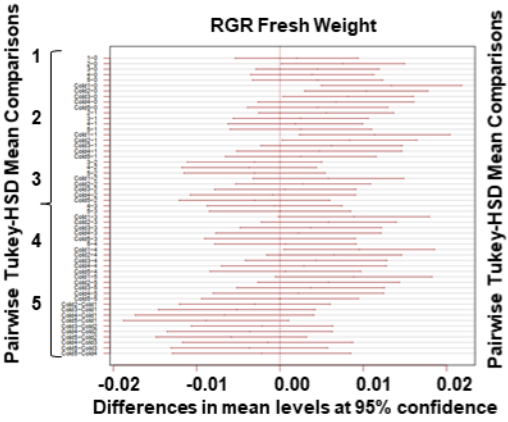

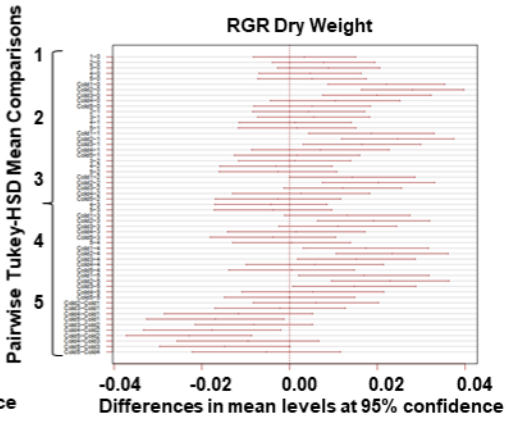

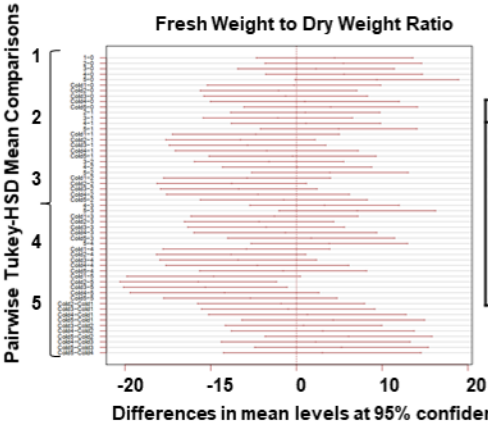

1	2	3	4	5
Control 1-Control 0	Control 3-Control 1	Cold 1-Control 2	Cold 5-Control 3	Cold 5-Control 5
Control 2-Control 0	Control 4-Control 1	Cold 2-Control 2	Control 5-Control 4	Cold 2-Cold 1
Control 3-Control 0	Control 5-Control 1	Cold 3-Control 2	Cold 1-Control 4	Cold 3-Cold 1
Control 4-Control 0	Cold 1-Control 1	Cold 4-Control 2	Cold 2-Control 4	Cold 4-Cold 1
Control 5-Control 0	Cold 2-Control 1	Cold 5-Control 2	Cold 3-Control 4	Cold 5-Cold 1
Cold 1-Control 0	Cold 3-Control 1	Control 4-Control 3	Cold 4-Control 4	Cold 3-Cold 2
Cold 2-Control 0	Cold 4-Control 1	Control 5-Control 3	Cold 5-Control 4	Cold 4-Cold 2
Cold 3-Control 0	Cold 5-Control 1	Cold 1-Control 3	Cold 1-Control 5	Cold 5-Cold 2
Cold 4-Control 0	Control 3-Control 2	Cold 2-Control 3	Cold 2-Control 5	Cold 4-Cold 3
Cold 5-Control 0	Control 4-Control 2	Cold 3-Control 3	Cold 3-Control 5	Cold 5-Cold 3
Control 2-Control 1	Control 5-Control 2	Cold 4-Control 3	Cold 4-Control 5	Cold 5-Cold 4

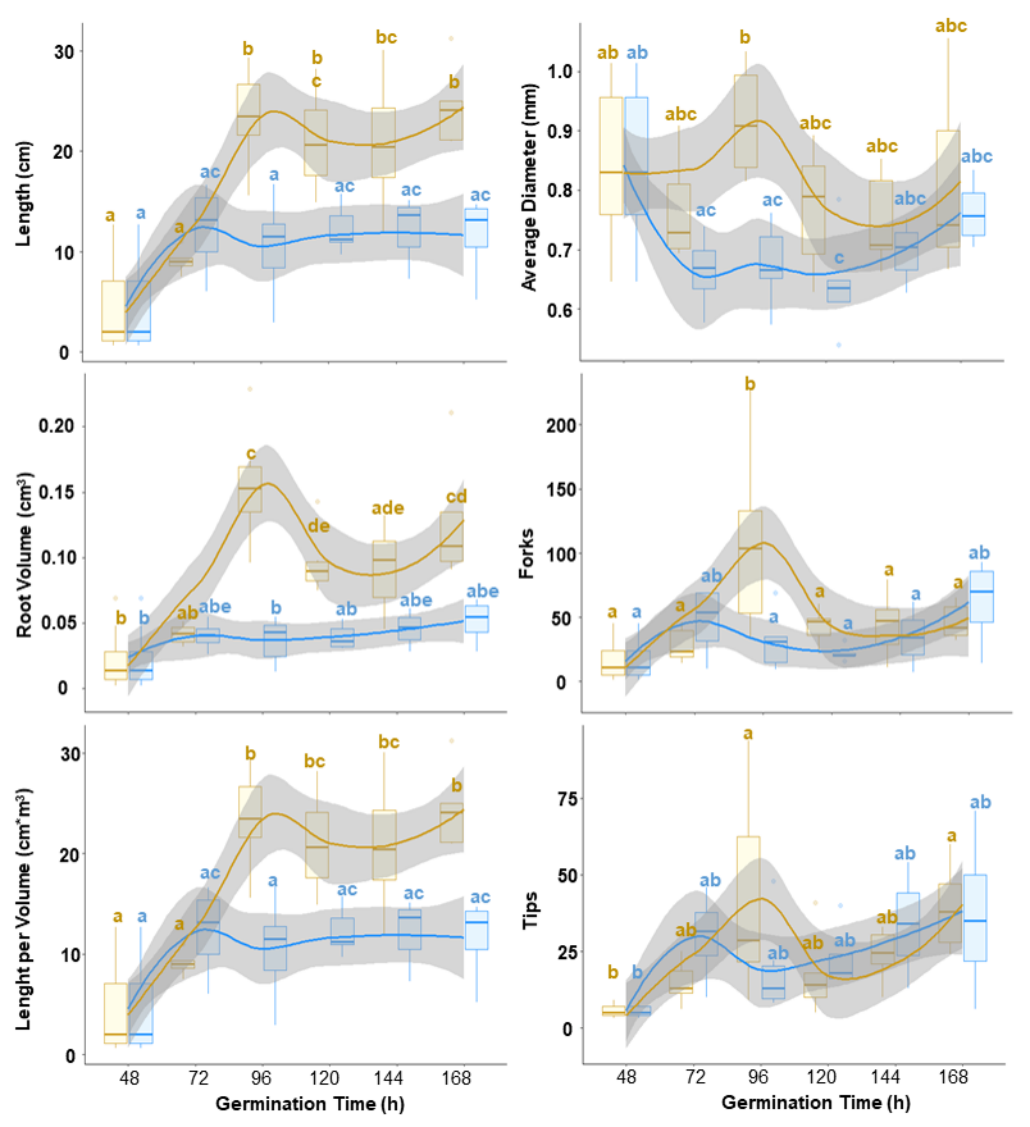
Length (cm)
Average Diameter (mm)
Root Volume (cm³)
Forks
Lenght per Volume (cm*m³)
Tips
Germination Time (h)
Germination Time (h)
48
72
96
120
144
168

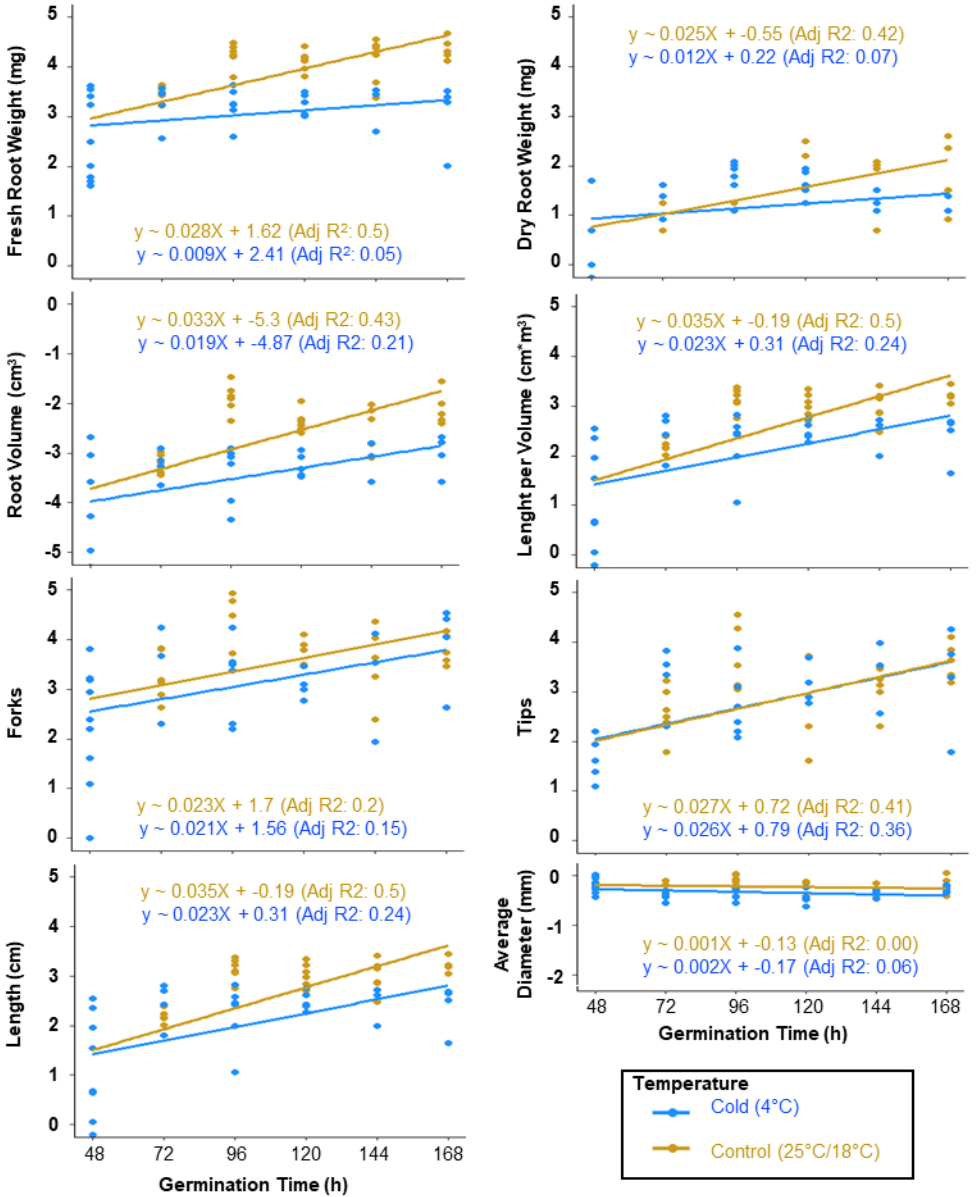
Fresh Root Weight (mg)
y ~ 0.028X + 1.62 (Adj R²: 0.5)
y ~ 0.009X + 2.41 (Adj R²: 0.05)
Dry Root Weight (mg)
y ~ 0.025X + -0.55 (Adj R2: 0.42)
y ~ 0.012X + 0.22 (Adj R2: 0.07)
Root Volume (cm³)
y ~ 0.033X + -5.3 (Adj R2: 0.43)
y ~ 0.019X + -4.87 (Adj R2: 0.21)
Lenght per Volume (cm*m³)
y ~ 0.035X + -0.19 (Adj R2: 0.5)
y ~ 0.023X + 0.31 (Adj R2: 0.24)
Forks
y ~ 0.023X + 1.7 (Adj R2: 0.2)
y ~ 0.021X + 1.56 (Adj R2: 0.15)
Tips
y ~ 0.027X + 0.72 (Adj R2: 0.41)
y ~ 0.026X + 0.79 (Adj R2: 0.36)
Length (cm)
y ~ 0.035X + -0.19 (Adj R2: 0.5)
y ~ 0.023X + 0.31 (Adj R2: 0.24)
Average Diameter (mm)
y ~ 0.001X + -0.13 (Adj R2: 0.00)
y ~ 0.002X + -0.17 (Adj R2: 0.06)
48
72
96
120
144
168
Germination Time (h)
Temperature
Cold (4°C)
Control (25°C/18°C)

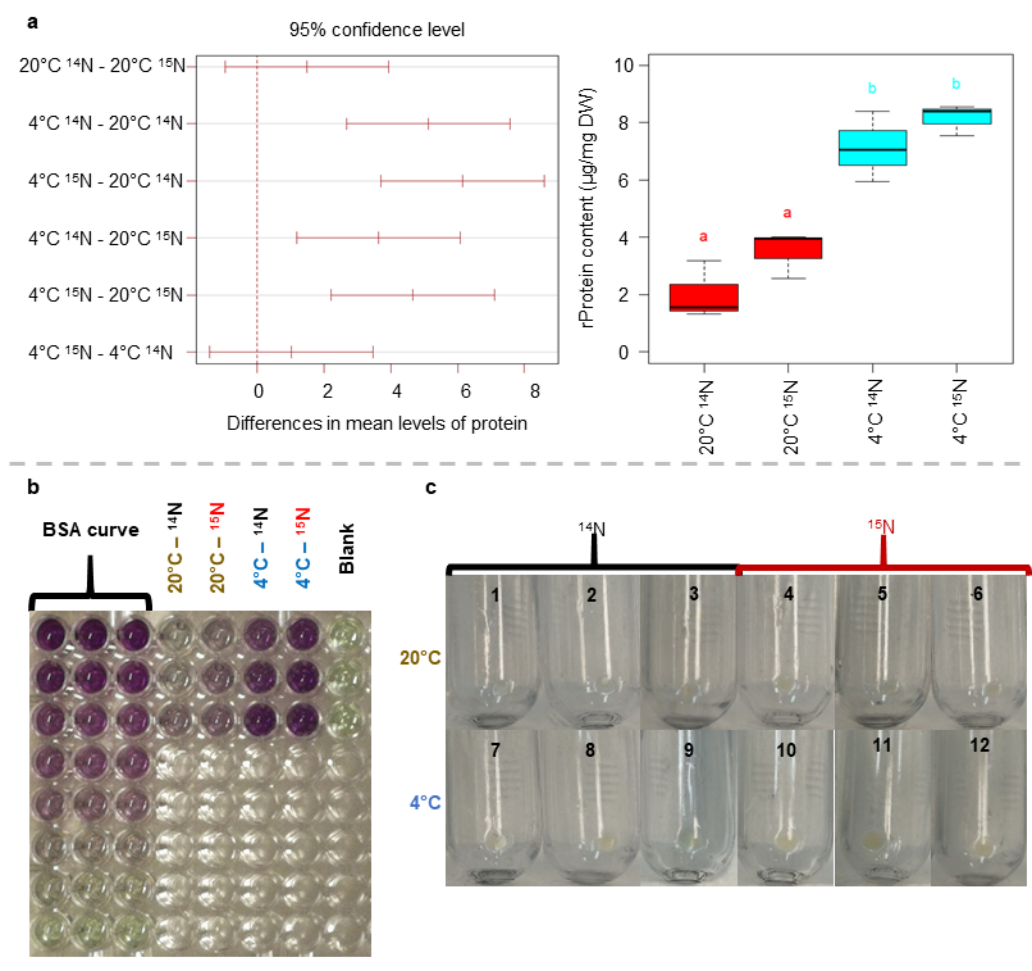
a
95% confidence level
20°C 14N - 20°C 15N
4°C 14N - 20°C 14N
4°C 15N - 20°C 14N
4°C 14N - 20°C 15N
4°C 15N - 20°C 15N
4°C 15N - 4°C 14N
0
2
4
6
8
Differences in mean levels of protein
rProtein content (µg/mg DW)
10
8
6
4
2
0
a
a
b
b
20°C 14N
20°C 15N
4°C 14N
4°C 15N
b
BSA curve
20°C – 14N
20°C – 15N
4°C – 14N
4°C – 15N
Blank
c
14N
15N
20°C
4°C
1
2
3
4
5
6
7
8
9
10
11
12

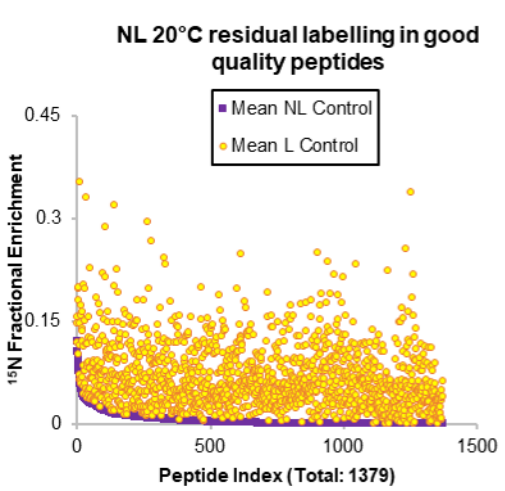
NL 20°C residual labelling in good quality peptides
Mean NL Control
Mean L Control
0.45
0.3
0.15
0
15N Fractional Enrichment
0
500
1000
1500
Peptide Index (Total: 1379)

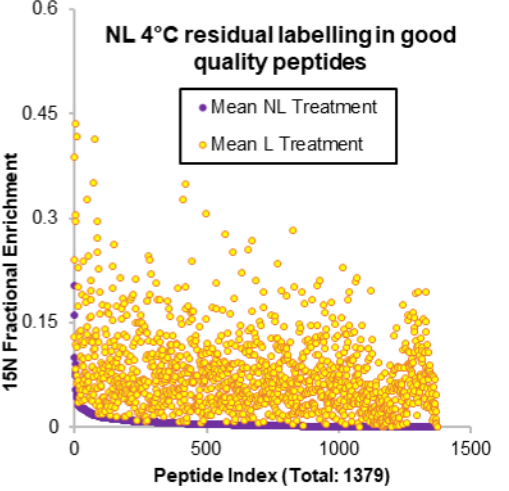
NL 4°C residual labelling in good quality peptides
Mean NL Treatment
Mean L Treatment
0.6
0.45
0.3
0.15
0
15N Fractional Enrichment
0
500
1000
1500
Peptide Index (Total: 1379)

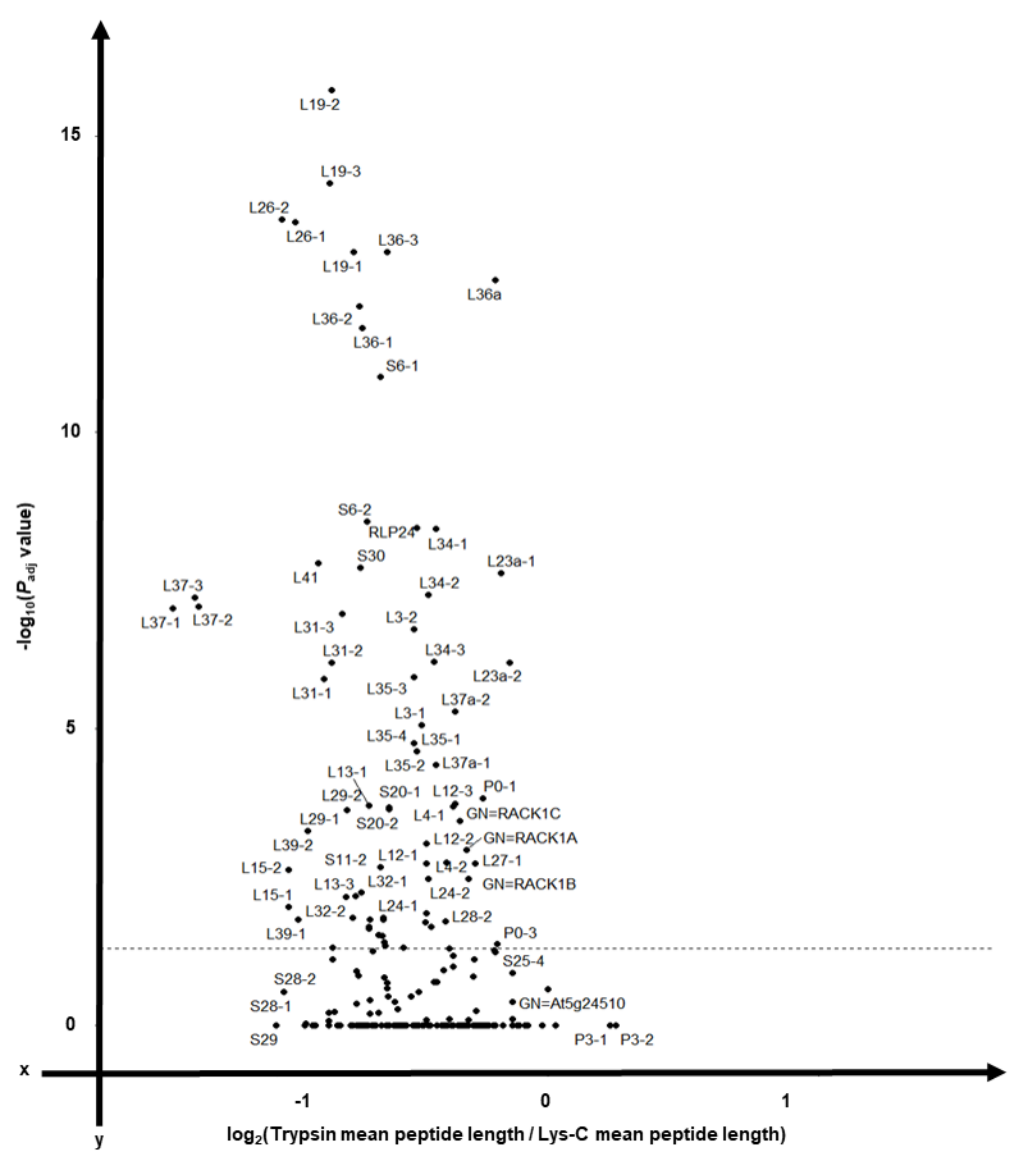
L19-2
L19-3
L26-2
L26-1
L36-3
L19-1
L36a
L36-2
L36-1
S6-1
S6-2
RLP24
L34-1
S30
L23a-1
L41
L34-2
L37-3
L37-1
L37-2
L31-3
L3-2
L31-2
L34-3
L23a-2
L31-1
L35-3
L37a-2
L3-1
L35-4
L35-1
L35-2
L37a-1
L13-1
L29-2
S20-1
L12-3
P0-1
L4-1
GN=RACK1C
L29-1
S20-2
L12-2
GN=RACK1A
L39-2
L15-2
S11-2
L12-1
L4-2
L27-1
L13-3
L32-1
GN=RACK1B
L15-1
L24-2
L32-2
L24-1
L28-2
L39-1
P0-3
S25-4
S28-2
S28-1
GN=At5g24510
S29
P3-1
P3-2
15
10
5
0
x
-1
0
1
y
-log10(Padj value)
log2(Trypsin mean peptide length / Lys-C mean peptide length)

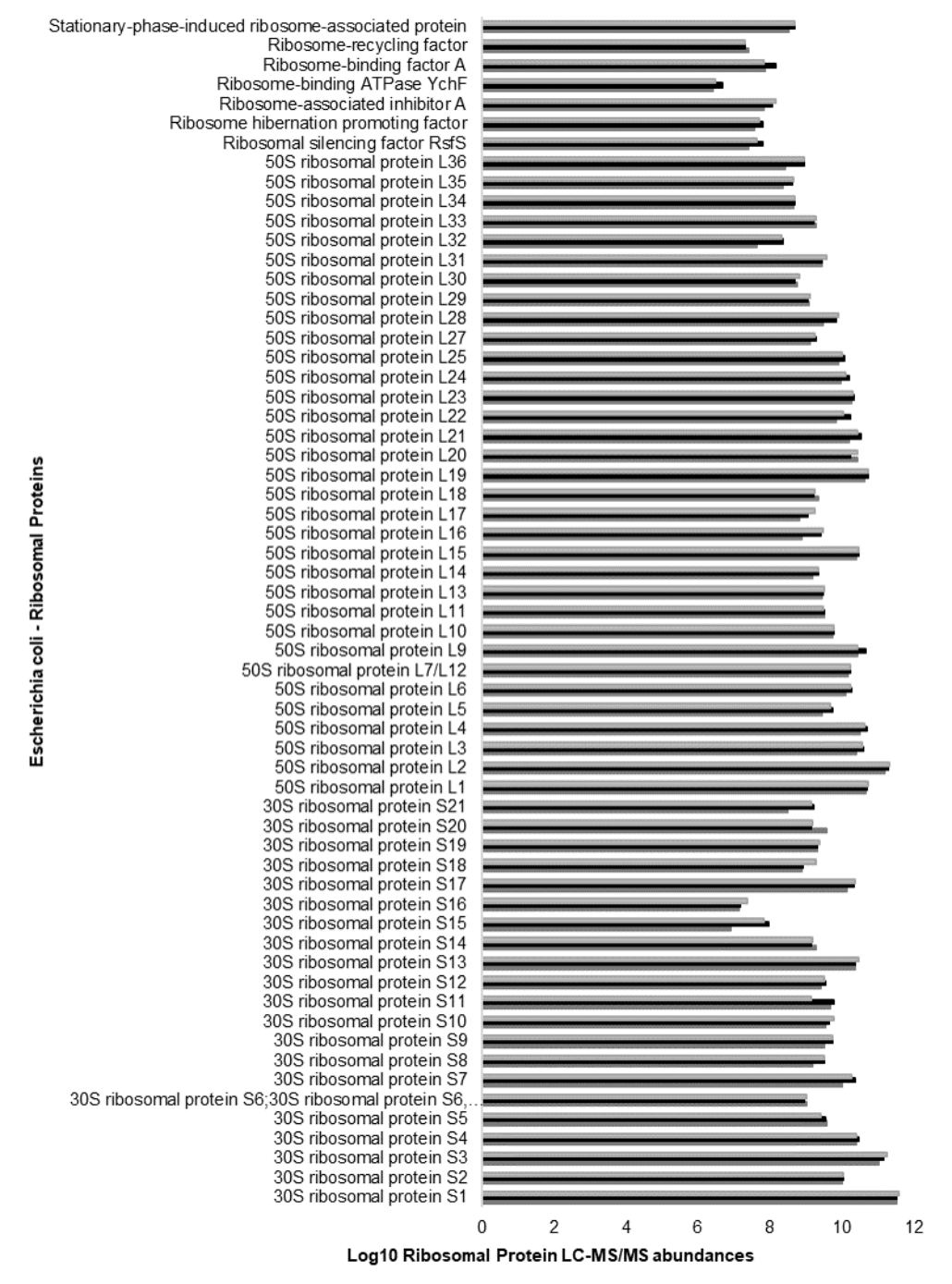
Stationary-phase-induced ribosome-associated protein
Ribosome-recycling factor
Ribosome-binding factor A
Ribosome-binding ATPase YchF
Ribosome-associated inhibitor A
Ribosome hibernation promoting factor
Ribosomal silencing factor RsfS
50S ribosomal protein L36
50S ribosomal protein L35
50S ribosomal protein L34
50S ribosomal protein L33
50S ribosomal protein L32
50S ribosomal protein L31
50S ribosomal protein L30
50S ribosomal protein L29
50S ribosomal protein L28
50S ribosomal protein L27
50S ribosomal protein L25
50S ribosomal protein L24
50S ribosomal protein L23
50S ribosomal protein L22
50S ribosomal protein L21
50S ribosomal protein L20
50S ribosomal protein L19
50S ribosomal protein L18
50S ribosomal protein L17
50S ribosomal protein L16
50S ribosomal protein L15
50S ribosomal protein L14
50S ribosomal protein L13
50S ribosomal protein L11
50S ribosomal protein L10
50S ribosomal protein L9
50S ribosomal protein L7/L12
50S ribosomal protein L6
50S ribosomal protein L5
50S ribosomal protein L4
50S ribosomal protein L3
50S ribosomal protein L2
50S ribosomal protein L1
30S ribosomal protein S21
30S ribosomal protein S20
30S ribosomal protein S19
30S ribosomal protein S18
30S ribosomal protein S17
30S ribosomal protein S16
30S ribosomal protein S15
30S ribosomal protein S14
30S ribosomal protein S13
30S ribosomal protein S12
30S ribosomal protein S11
30S ribosomal protein S10
30S ribosomal protein S9
30S ribosomal protein S8
30S ribosomal protein S7
30S ribosomal protein S6;30S ribosomal protein S6,...
30S ribosomal protein S5
30S ribosomal protein S4
30S ribosomal protein S3
30S ribosomal protein S2
30S ribosomal protein S1
Escherichia coli - Ribosomal Proteins
0
2
4
6
8
10
12
Log10 Ribosomal Protein LC-MS/MS abundances

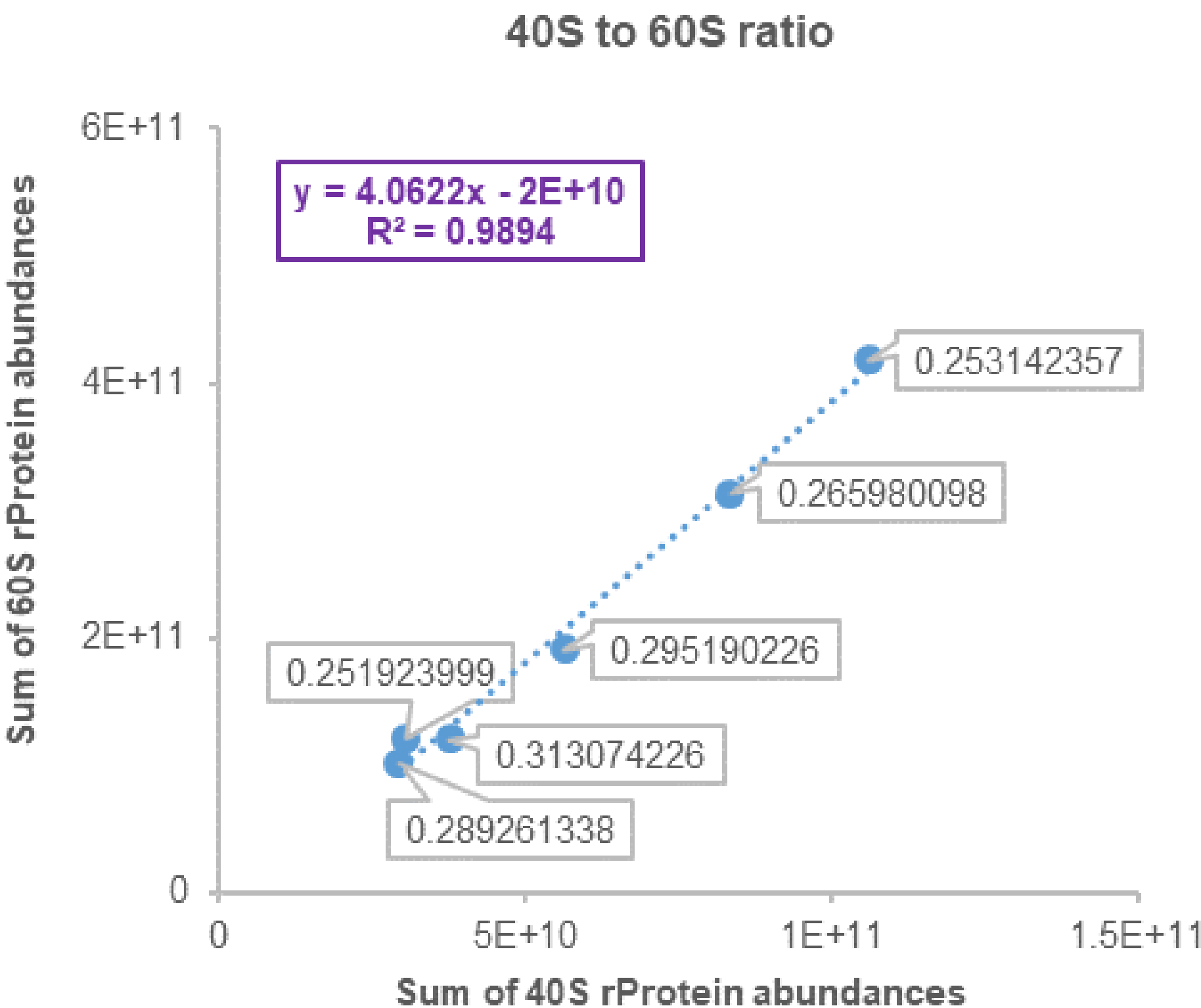
40S to 60S ratio
y = 4.0622x - 2E+10
R² = 0.9894
6E+11
4E+11
2E+11
0
0
5E+10
1E+11
1.5E+11
Sum of 60S rProtein abundances
Sum of 40S rProtein abundances
0.253142357
0.265980098
0.295190226
0.251923999
0.313074226
0.289261338